Tidal Hydrodynamics in a Multi-Inlet Wetland System: Toward Improved Modeling of Salt Marsh Flooding and Draining

BY

Mithun Deb, James T. Kirby, Fengyan Shi
and Ali Abdolali

CENTER FOR APPLIED COASTAL RESEARCH

University of Delaware
Newark, Delaware 19716

ACKNOWLEDGEMENTS

TABLE OF CONTENTS

Chapter

Appendix

LIST OF TABLES

LIST OF FIGURES

ABSTRACT

Modeling hydrodynamics and sediment transport inside a multi-inlet wetland system is a challenging task due to constraints on model efficiency, accuracy and representation of physics, the scarcity of field data for model validation, and more importantly, the availability of high-resolution data sets of marsh topography and channel bathymetry. Lack of field data sets, model assumptions, and limitations often lead to wrong interpretation of the system's nature. To correctly predict the changes in governing hydrodynamics and morphology of shallow wetland environments, it is essential to resolve the complex interaction between the tidal channel and marsh surface with the best possible accuracy. In this thesis, we describe the development of a high-resolution 2D numerical model for a rapidly eroding tidal wetland system using the Finite-Volume, primitive equation Community Ocean Model (FVCOM). Topo-bathymetric survey data and water surface and current velocity measurements during calm and stormy conditions have been collected in support of model development and validation. The model is then used to perform a morphology scenario analysis to evaluate the effect of anthropogenic and natural disturbances in altering overall wetland hydrodynamics. The study has also shown the role of horizontal model resolution around the marsh channel shoreline and surveyed bathymetry data in improving the model calculations for major physical processes such as channel surface phase lag, tidal wave characteristics, and flow asymmetry. Hydrodynamic processes over marsh topography are seen to be significantly affected by surface defects such as cuts and rills on the marsh platform. Inadequate representation of these meter-scale features from spatial resolution available from data sources such as LiDAR, as well as the incomplete resolution in the model grid itself, lead to artificial ponding over the isolated marsh depressions, with resulting effects on estimates of sediment fluxes and hydroperiod. A

new set of mass and momentum conservation equations is proposed using a surface porosity technique to improve the dynamic wetting and drying over artificially isolated depressions. This model improvement is essential for accurate predictions of marsh hydroperiod and volume flux that primarily controls the sedimentation rate and overall morphological evolution. Ultimately, by solving these critical processes, the study has provided useful solutions to improve the present-day limitations in numerical modeling of salt marsh flooding and draining.

Chapter 1

INTRODUCTION

Coastal wetlands are dynamic landscapes that occur in the intertidal zone between land and the sea, and involve continuous feedback between hydrodynamic forces, vegetation types and sediment erosion/accretion. They act as a natural defense system to protect the coastal communities and provide an essential buffer against storm surge, wind waves, and even tsunamis. However, the salt marshes in the U.S. have been disappearing recently at an increasing rate due to various natural and anthropogenic processes such as sea-level rise, severe meteorological events, and man-made morphology changes. According to US EPA (United States Environmental Protection Agency), the rate was more than 80,000 acres per year between 2004 and 2009 and 59,000 acres per year from 1998 to 2004 (http://epa.gov/wetlands/coastal-wetlands) due to a variety of commercial, residential, industrial activities and conversion for agricultural uses.

The wetland geomophology and tidal processes depend on each other (Dronkers, 1986). An abrupt change in the morphology can directly affect the hydrodynamics, which in turn alter the formation of the wetland over a short or long term (e.g. Speer, 1984). Over the years, the construction of artificial structures such as levees and canals have changed the course of tidal hydrodynamics in many coastal wetlands, ultimately leading to marsh habitat alteration and destruction (Williams, 1995). Single events, such as violent storms, have caused numerous breaches and formed new inlets that changed the wetland-Bay dynamics (Ramsey and Reilly, 2002; Aretxabaleta et al., 2017). The Bombay Hook National Wildlife Refuge (BHNWR), DE, is one of the largest remaining expanses of tidal wetlands in the mid-Atlantic region and has lost almost 20% of its salt marsh area since 1949 from a combination of anthropogenic and

natural activities (McDowell, 2017). Artificial channels and oxbows were constructed to connect the interior marsh to Delaware Bay to improve the marsh drainage (Dozier, 1947). Over the years, the system's main channels have progressively deepened and widened, and several tidal mudflats have formed, making it more ebb dominant and erosive in nature (Deb et al., 2018a). In light of the importance of the BHNWR to both the ecology and economy of the Delaware coastal environment, we needed a robust high-resolution numerical modeling system to identify the major causes responsible for changing the tidal hydrodynamics. In Chapter 2, we have described the development of a high-resolution two-dimensional model system for the entire BHNWR tidal wetland environment based on the Finite-Volume, primitive equation Community Ocean Model (FVCOM, Chen et al. (2013)). The unstructured grid developed for BHNWR covers the entire marsh system with sufficient grid resolution to resolve small channels and creeks. The model performance is validated using surface elevation at several tidal gauges, ADCP current velocity data collected from the major channels, and pressure data over the marsh platform. The effects of a historical man-made channel construction, ongoing channel deepening, and a potential inlet opening in shifting wetland hydrodynamics are shown by developing a scenario analysis. Tidal asymmetry is estimated in the marsh interior and inlets to show the role of morphology changes in system's continuous progression toward a frictionless regime. Finally, the results are explained using simple inlet-channel-bay relationship and scaling analysis to highlight the primary balance between the governing forces.

Developing a highly precise wetland/salt-marsh 2D model is a challenging task as it requires an understanding of the optimum grid resolution and, more importantly availability of high-resolution data sets of marsh topography and channel bathymetry. During the hydrodynamic model development in Chapter 2, we have noticed two important present-day modeling limitations associated with flooding and draining in both the inter-tidal channels and marsh platforms. First, an increase or decrease of the channel resolution in the model can change the hypsometry and directly affect the flow continuity and momentum. In a marsh-channel environment with sharp bathymetry

gradients, an inadequate representation of the channel berms can influence the bay-channel volume flux, and also the volume of water that goes back and forth between the channel and marsh surface. Channel properties and inter-tidal storage, along with the oceanic forcing, controls the tidal asymmetry (i.e., flood/ebb dominance) and over-all stability of a tidal wetland (Aubrey and Speer, 1985; Speer et al., 1991; Friedrichs, 2010). Sediment transport directly correlates with the surface elevation/velocity asymmetry, which can be in the form of magnitude and period of the tidal wave (Friedrichs and Aubrey, 1988; Nidzieko, 2010). An accurate estimate of tidal asymmetry and wave characteristics is essential for determining the residual flow, direction, and sediment budget. Therefore, to have a reliable estimate of the tidal amplitude, phase speed, and asymmetry, it is necessary to correctly resolve the land-water flow exchange and channel hypsometry with optimum spatial grid resolution. In addition to the adequate grid resolution, a high-density bathymetry data is also needed to properly represent the channel hypsometry in model calculations (Yu and Lane, 2006; Horritt et al., 2006). The improper geometric representation from sparse survey data can heavily constrain the model performance. In Chapter 3, we have demonstrated why it is essential to re-solve the variation in channel hypsometry with a higher accuracy that improves model reliability for the prediction of tidal characteristics. The changes in along-channel sur-face phase lag for different geometric conditions is also explained using the 1D Saint Venant equations for irregular cross-sections, which has given an essential insight on the sensitivity of tidal waves to channel properties.

After observing an improved channel flooding and draining, we looked into the model performance over the marsh platform. We noticed that the inundation process over marsh surface is significantly affected by surface defects such as cuts and rills on channel berms and narrow creeks on the platform. Channel embankments or berms form hydraulic depressions on the marsh platform that flood during the high tide and drains slowly through small cuts and rills during ebb. These meter-scale features are often missing in the model representation due to the spatial resolution available from

data sources, as well as incomplete resolution in the model grid itself. Inadequate representation of the ground irregularities in the model leads to the formation of artificial hydraulic depressions and changes the marsh flooding and draining process.

The geomorphological developments in salt marshes depend on the sea level and tidal oscillations, where the plant growth and sedimentation are controlled by hydroperiod and advection of fine sediments from the channels (Fagherazzi et al., 2012). The vegetation biomass growth rate depends particularly on tidal amplitude, period, and local elevation, resulting in multiple vegetation types that dominate different zones (Morris, 2006). With the growing availability of computational resources, to predict the long-term marsh evolution, a range of process-based physical models are being used nowadays to resolve marsh overland flooding and draining and sediment transport with the highest resolution possible (e.g. D'Alpaos et al., 2007; Zhang et al., 2019). The artificial ponding seen over marsh depressions can lead to incorrect modeling of vegetation dynamics, and of the volume and speed of flooding and draining processes, ultimately leading to an inaccurate marsh platform geomorphological evolution. In Chapter 3, we have implemented a surface porosity technique in the mass and momentum conservation equations to improve the inundation process in artificially isolated depressions in the FVCOM model. We proposed the new set of equations based on the existence of narrow cuts and rills over the channel berms. Our modeling strategy is conceptually similar to Chen et al. (2000) and Kennedy et al. (2000) in defining the time-varying slot area, but differs in porosity calculations based on the representation of marsh elevation. We made the modifications primarily to eliminate artificial ponding effects observed in hydrodynamic model simulations for any given Digital Elevation Model (DEM). The model performance is tested using different idealized marsh conditions to explain the slot mechanism in simple and well-defined artificial ponds. Using the same setup, we have also shown the sensitivity of model flooding and draining to the variation in slot geometry and bottom roughness. Finally, we verified our proposed strategy against an extensive set of pressure measurements obtained from a real marsh depression in BHNWR.

The work presented in Chapter 2 and 3 is under review, and Chapter 4 is in preparation for journal publications.

Chapter 2

SENSITIVITY OF TIDAL HYDRODYNAMICS TO MORPHOLOGY CHANGES IN A MULTI-INLET RAPIDLY ERODING SALT MARSH SYSTEM: A NUMERICAL STUDY

2.1 Introduction

Coastal wetlands provide important ecosystem services such as protecting coastal areas from storm damage and sea level rise, and providing refuge and breeding ground for migrating shorebirds, waterfowl, and other wildlife. The National Oceanic and Atmospheric Administration (NOAA) and the U.S. Fish and Wildlife Service (USFWS) analyzed the status and trends of wetland acreage along the Atlantic Coast, Gulf of Mexico, and the Great Lakes and reported that 361,000 acres of coastal wetlands were lost in the Eastern United States alone between 1998 and 2004 (Stedman and Dahl, 2008). These changes are possibly due to a number of various anthropogenic and natural processes such as sea level rise, man-made morphology changes, overgrazing by native and migratory species, and severe meteorological events. Historically, the Mid-Atlantic region has lost coastal wetlands due to the variety of commercial, residential, industrial activities and conversion for agricultural uses (EPA, 2010). Coastal wetlands have also been particularly affected by conversion of tidal wetlands to open water by construction of impoundments and sea level rise (Tiner, 1987). Construction of levees and canals have changed the course of tidal inundation in many coastal wetlands, and led to marsh habitat alteration and destruction (Williams, 1995). During large storm events, the wetland systems are often affected by the offshore storm surge and waves, where the storm induced breaching changes the bay-inlet-ocean dynamics and the volume exchange (Aretxabaleta et al., 2017). In the state of Delaware, along Delaware River, numerous breaches were recorded over the last century from historical storms

that caused dramatic changes in the wetland ecosystems (Ramsey and Reilly, 2002; Runion, 2019). The Bombay Hook National Wildlife Refuge (BHNWR), DE is one of the largest remaining expanses of tidal wetlands in the mid-Atlantic region and has lost almost 20% of its salt marsh area since 1949 (Figure 2.1). Over the years, this multi-inlet salt marsh system has gone through a combination of anthropogenic (Dozier, 1947) and natural changes (Ramsey and Reilly, 2002), shifting its tidal dynamics from time to time. In light of the importance of the BHNWR to both the ecology and economy of the Delaware coastal environment, it is essential to obtain a better functional understanding and predictive capability of the system's morphological evolution.

The coastal wetland morphology and tidal processes are interdependent on each other, and an abrupt change in the estuarine morphology by any anthropogenic or natural processes could affect the hydrodynamics which in turn alter the evolution of the estuary (Speer, 1984; Dronkers, 1986). The hydrodynamic regime, including asymmetry in the system (i.e., flood/ebb dominance during spring/neap tide) and inter-tidal storage controls the net volume exchange, residual volume transport and overall stability of a tidal wetland (Aubrey and Speer, 1985; Speer et al., 1991; Friedrichs, 2010). The tidal asymmetry can be represented in two ways, 1) using duration asymmetry that measures the difference in duration and/or amplitude between rising and falling tide (slack water difference), and 2) using velocity skewness that characterizes the ebb and flood current distribution over a tide cycle (peak velocity skew) (Nidzieko and Ralston, 2012). The difference in slack water period between ebb and flood generally affects the residual flux of the fine suspended load, where the difference between maximum tidal currents during ebb and flood particularly affects the bed load transport (Dronkers, 1986). While the duration asymmetry is controlled by the variation in channel volume and the intertidal volume of adjacent shoals (Speer, 1984; Friedrichs, 2010), the velocity skew can generate from the local bathymetry gradients, quadratic friction and the phase lags between the surface gradient and local depth (Nidzieko and Ralston, 2012). Boon and Byrne (1981) and Speer (1984) have investigated a few inlet/estuary systems in the U.S. east coast, where Murrells Inlet, SC and Nauset Inlet, MA are observed to

be flood dominant (longer falling tide and a higher current velocity during flood at the inlet) and Wachapreague Inlet, VA is identified as ebb dominant (shorter ebb duration and a stronger ebb current). An important distinction is also noticed by Speer (1984) in Pamet River, MA, where a shorter rising duration asymmetry exist with the ebb dominant inlet discharge as the interior falling tide decouples from the offshore falling tide.

The net residual sediment transport in a system is related to tidal asymmetry and phase difference between surface elevation and flow velocity (Hsu et al., 2013; Ralston et al., 2013), and in order to predict the morphology evolution of such short inlet/estuaries, it is imperative to identify the state of tidal asymmetry. In this study, we have developed a high-resolution two-dimensional model system for the entire BHNWR tidal wetland environment based on the Finite-Volume, primitive equation Community Ocean Model (FVCOM, Chen et al. (2013)). The unstructured grid developed for BHNWR covers the entire marsh system with sufficient grid resolution to resolve small channels and creeks. The grid bathymetric data in channels is based on data collected during an extensive bathymetric survey, and the topographic portion is developed from the vegetation bias corrected LiDAR data set. The model is validated using surface elevations at several tidal gauges and the ADCP current velocity data. Model performance for predicting flooding/draining processes during normal and storm conditions has been examined using the data collected on the marsh platform. Subsequently, we use the model to examine tidal asymmetry and flow exchange in the marsh's multiple entrance channels to determine the governing hydrodynamics. Finally, a scenario analysis is developed based on the historical anthropogenic and natural changes to evaluate the effects of artificial channel construction, channel deepening, and a potential inlet opening on the tidal hydrodynamics.

This chapter is organized as follows. The history of the case study alternation over time is presented in 2.2. Section 2.3 describes the model grid and Digital Elevation Model (DEM) development from corrected high-resolution LiDAR data and channel survey data, and model forcing preparation at the open boundaries. Model

validation with the field data is given in this section. Calculations for tidal asymmetry, and scenario development with present-day bathymetry and morphology changes is provided in section 2.4. Section 2.5 discusses the changes in dominant hydrodynamics due to human intervention, long term changes in channel hypsometry and potential inlet opening due to shoreline erosion. Concluding remarks and observations on needed future works are given in section 2.6.
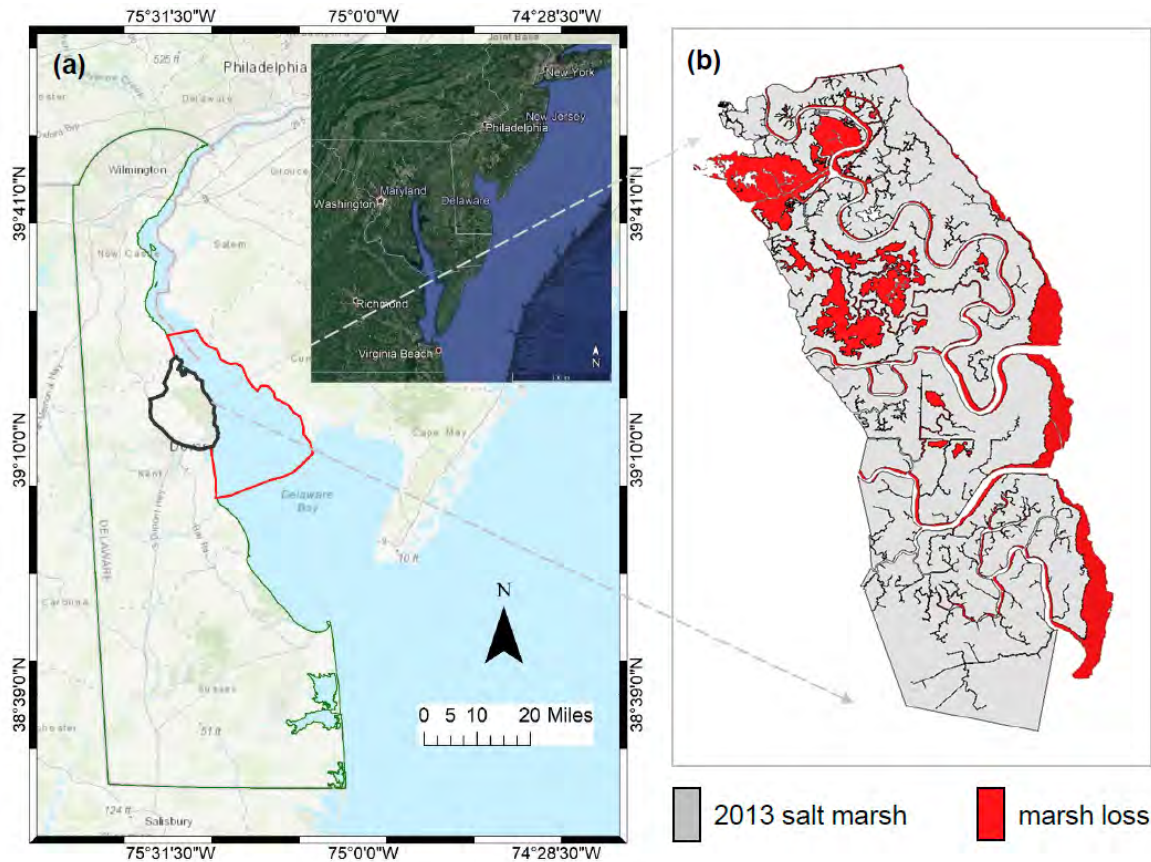
Figure 2.1: (a) Bombay Hook National Wildlife Refuge, DE. Red and black polygons show the model outer boundaries in Bay and BHNWR respectively; (b) Marsh loss between 1949 and 2013. Grey area shows the existing salt marsh while the marsh platform loss since 1949 is shown in red (panel (b) taken from McDowell and Sommerfield (2016)).

2.2   Regional description

The marshes of BHNWR provide a buffer to adjacent communities and large areas of highly productive farmlands. The refuge itself is a key component of the local economy where it provides nearly \$100M/year in ecosystem services such as clean water, fisheries habitat and carbon sequestration (Kauffman et al., 2011). During a large Nor'easter storm in May 2008, the refuge's impoundment boundary was breached by water for the first time in the history of refuge management, illustrating the increasing vulnerability of the wetlands and freshwater impoundments to storms and sea level rise. The BHNWR wetland system originally had three natural tidal inlets, namely the Leipsic River, the Simon River and the Woodland Beach, and based on historical evidence (Dozier, 1947; Ramsey and Reilly, 2002), the channel depths were much lower than the present condition. A new channel Sluice Ditch is constructed in 1890 to connect the marsh interior at Duck Creek directly to the Delaware Bay (Dozier, 1947). Additionally, several oxbows in the course of the Leipsic River were straightened prior to 1900 and also during that year, which changed the drainage system of wet areas. In the last couple of decades, the main channels of the system have progressively deepened and widened and now the cross-section averaged depth is almost 10.0 m at some locations along the channel, while the width reached approximately 100.0 m in Sluice Ditch and 200.0 m in the Leipsic River. From the comparison of historic imagery's in Figure 2.1, we can also see that the system has different trends in the disturbed and undisturbed regions. In one part, three of the inlets: Leipsic River, Sluice Ditch and and Woodland Beach are connected to each other by the major channels and it is considered as the disturbed region, while the other part, Simon River inlet is mostly separated from the system and has less overall erosion. Simon River has a few smaller channels that connect to the Leipsic River during high tide and becomes extremely shallow at other times, making it less vulnerable to the ongoing channel deepening and erosion. Beside the internal marsh and channel erosion, the marsh shoreline with the Delaware Bay has also gone through significant erosion over the years due to local wind wave thrust on the scarp edge (Chen et al., 2018). All these historic and ongoing

erosive processes in BHNWR have been carefully taken into consideration for different morphology scenario analysis, performed at the later part of the study.

2.3 Model setup and validation

FVCOM solves seven primitive governing equations for momentum, incompressible continuity, temperature, salinity and density. The momentum equations are solved using the mode-splitting method, in which, an external mode solves 2D depth-integrated equations and an internal mode solves the equations in the vertical direction. This model has been previously used in several estuarine and coastal studies featuring complex topo-bathymetry, inter-tidal wetting and drying, and irregular coastline (Chen et al., 2008). Huang et al. (2008) used FVCOM 3D successfully to analyze wetland and estuarine interaction processes and tidal asymmetry in Okatee Creek, South Carolina. Similarly, Ralston et al. (2013) validated FVCOM using field data and investigated hydrodynamics and sediment transport on deltaic tidal flats at the mouth of the Skagit River, in Puget Sound, WA.

2.3.1 Unstructured grid development

The domain for the numerical simulation covers an area similar to that used by Stammerman (2013) for a previous hydrodynamic study of the same area. The model grid domain shown in Figure 2.2a covers Delaware Bay from Bowers, DE on the southern boundary up to 39° 25′ N latitude in Delaware River. The grid is extended landward on the western shore of the bay to cover the entire BHNWR wetland. Grid resolution in marsh-channel boundaries are as fine as $\sim$ 3 m in order to resolve channels and channel berm geometry. This is important for the wetting and drying process over the marsh platform that has a control over the tidal asymmetry and the total flux going in or out of the system. We have collected three high resolution LiDAR data sets of the study area and processed to a regular grid with 1 m in resolution. After comparing them with the surveyed marsh ground elevation, we selected the most accurate one, and further corrected the bias based on surveyed vegetation type data along random

11

transects in different wetland locations. Interestingly, from the comparison between LiDAR and field survey, we observed an uniform bias distribution of 0.1 m for locations representing high marshes and close to 0.2 m for low marshes in the LiDAR DEM. The DEM is then readjusted considering these two sets of errors and ultimately interpolated to the model unstructured grid nodes. Bathymetric surveys of the main waterways in BHNWR were conducted to obtain continuous depth soundings of the bottom below tide level. The data was de-tided using the nearest tide-gauge location Dock and the soundings were converted to the NAVD88 datum for gridding with LiDAR data. The detailed description of the LiDAR source and accuracy, DEM comparison with the ground truth survey, vegetation bias correction, channel survey and pre/post processing of the data set can be found in Deb et al. (2018a) and McDowell (2017).

2.3.2 Model forcing

The FVCOM unstructured grid with refinement in BHNWR area is driven by surface elevation and flux information at upstream and downstream boundary nodes, extracted from a large scale study using ROMS model. These forces need to be carefully defined as they are very sensitive to the overall performance of our local scale FVCOM model. A small error in boundary forcing can misrepresent the hydrodynamic processes (e.g., marsh surface wetting/drying) in a wetland system and can lead to subsequent errors in further estimations. ROMS simulations were performed for the years of 2012 and 2015 (Kukulka et al., 2017; Rodrigues, 2016) on a regular curvilinear grid of the Delaware bay with offshore extent to the continental shelf boundary, covering the entire Delaware Bay and estuary as is shown in Figure 2.2a (Abdolali et al., 2016). This grid has a maximum resolution of 0.75-2.0 km near the bay mouth and lowest grid resolution of about 8 km near the shelf break. Ten depth layers are specified to resolve the vertical depth variation using a terrain following coordinate system. The ocean model is driven with nine dominant tidal constituents (M2, S2, M4, M6, K2, K1, N2, O1, and Q1) imposed from ADCIRC database (Luettich Jr et al., 1992). The atmospheric pressure and wind forcing are taken from the North American Mesoscale

model (NAM) (`nomads.ncdc.noaa.gov`) and river discharge data has been added from USGS gauge at Trenton, New Jersey (`waterdata.usgs.gov`) in the upstream boundary that represents the Delaware River. Results are compared against a nearest NOAA tide gauge of the study area Ship John Shoal, NJ, located in the Delaware Bay (`https://tidesandcurrents.noaa.gov/waterlevels.html?id=8537121`). From Figure 2.3, it can be clearly seen that ROMS predicts tidal harmonics accurately (second panel) and underestimates the sub-tidal signal (third panel) at Ship John Shoal gauge. It can be possibly due to inaccurate representation of the remote forcing from NAM. To properly represent surface elevation at the FVCOM boundary, we separated the elevation data from ROMS into tidal and sub-tidal signals using T_TIDE, a tidal harmonic analysis tool (Pawlowicz et al., 2002). Then, we applied the same procedure to publicly available NOAA tide gauge datasets from Reedy point, DE; Ship John Shoal, NJ and Bower, DE in the Delaware Bay, and observed a similar trend in their sub-tidal signals. Finally, we have superimposed the ROMS tidal harmonics at the FVCOM boundary nodes with in-situ sub-tidal data from NOAA tide gauges near boundary nodes. This has improved the surface elevation forcing at FVCOM boundaries. Meanwhile, we kept the volume flux information from ROMS unchanged at the FVCOM boundary nodes. In FVCOM, it is possible to implement three different nesting conditions at the boundary, denoted as "direct nesting", "indirect nesting" and "relaxing nesting". We used the "direct nesting" approach in FVCOM, which allows nesting between small domain FVCOM and large domain ROMS with corrected sub-tidal data and volume flux at open boundary nodes. Lateral mixing is computed using the Smagorinsky scheme with a horizontal diffusion coefficient of 0.2 m^2/s. We used a Manning's Roughness Coefficient of $n = 0.02$ to estimate the drag coefficient C_d.
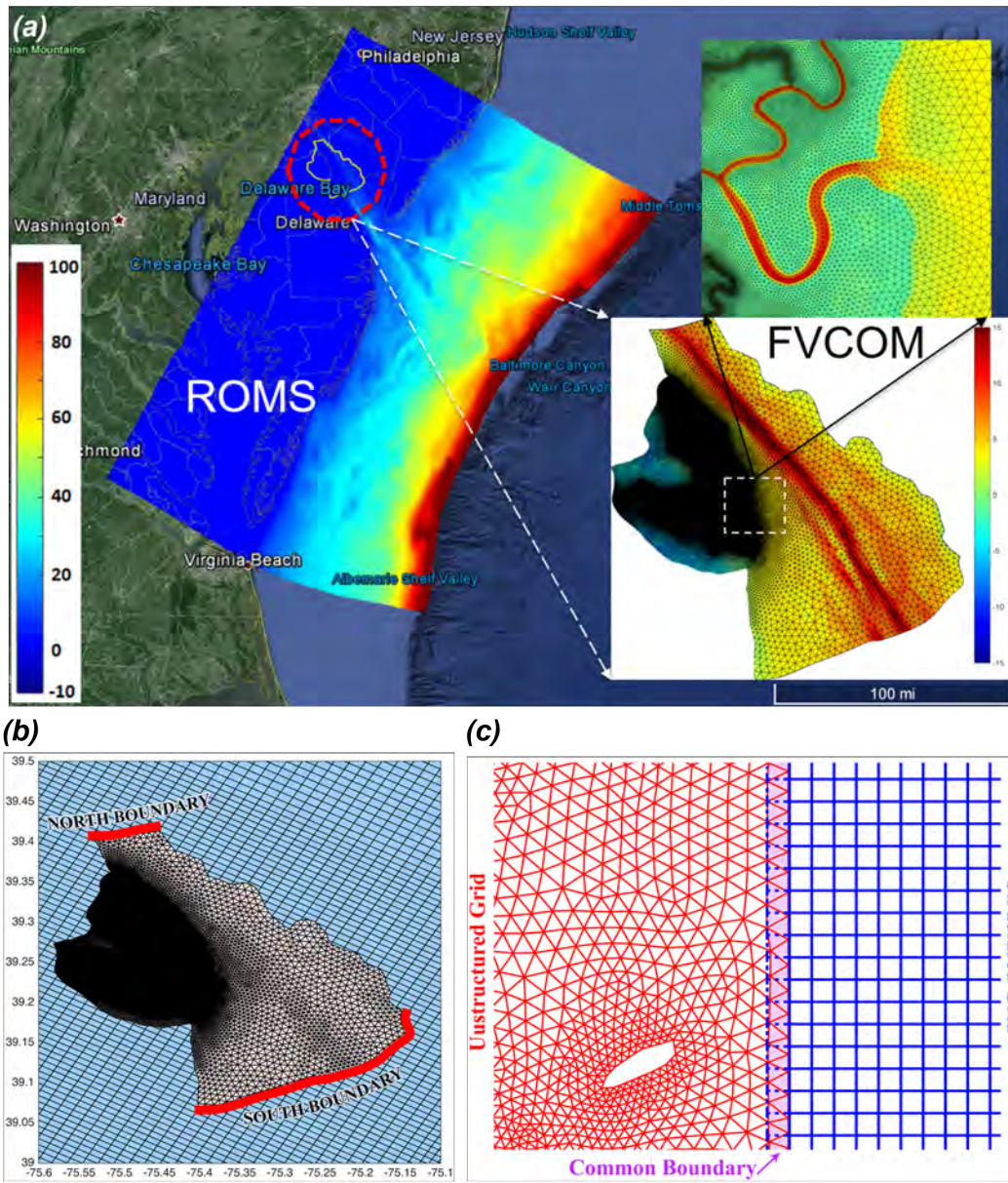
Figure 2.2: Models coupling scheme; (a) structured ROMS numerical domain covering Delaware Bay extended to the continental shelf in Atlantic ocean and unstructured FVCOM domain. The grid depth is shown in meters, from NAVD88 vertical reference level; (b) Schematic view of data exchange between ROMS and FVCOM at common boundary nodes at upstream and downstream side of the Delaware Bay; (c) Schematic view of FVCOM direct nesting at the boundary nodes.
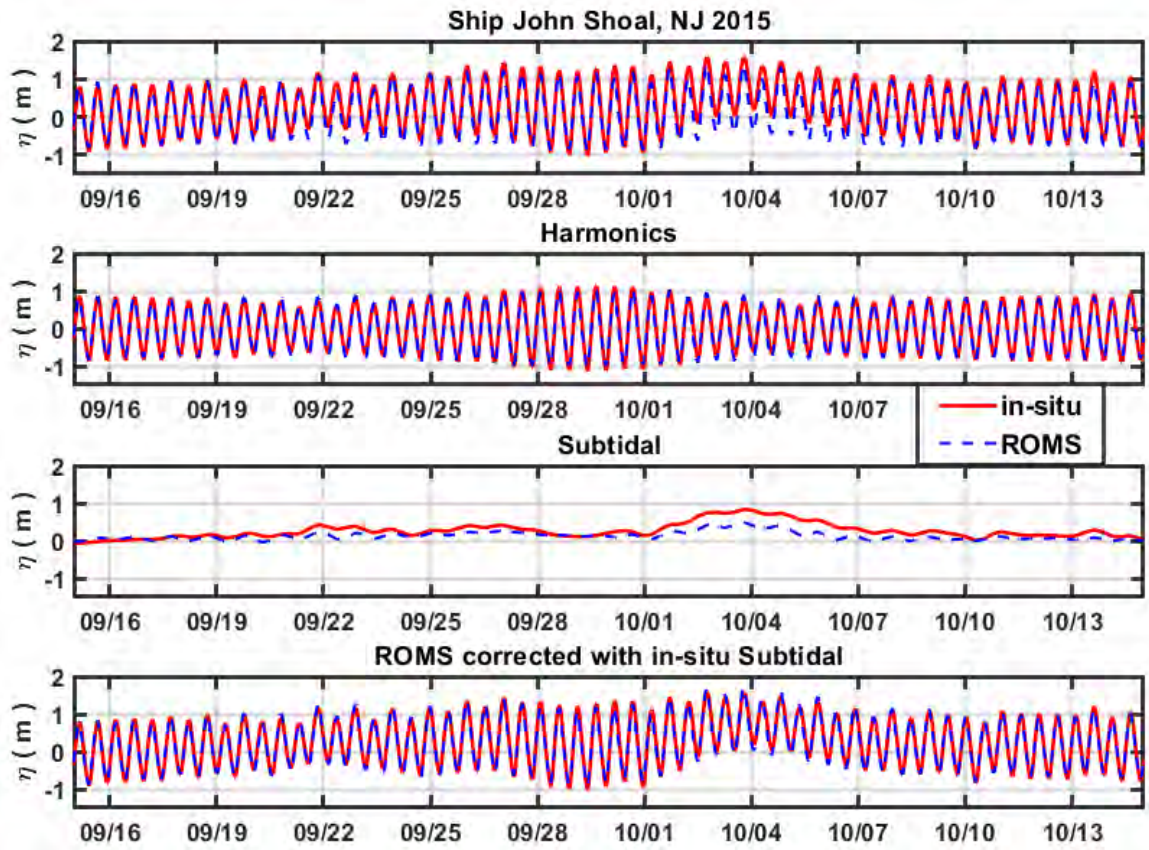
Figure 2.3: Comparison of in-situ (red) and ROMS outputs (blue) in term of free surface elevation at Ship John Shoal, Delaware Bay (2015); Pre-processed signals (top), tidal harmonics (second panel), subtidal (third panel) and subtidal corrected (lower panel) signal.
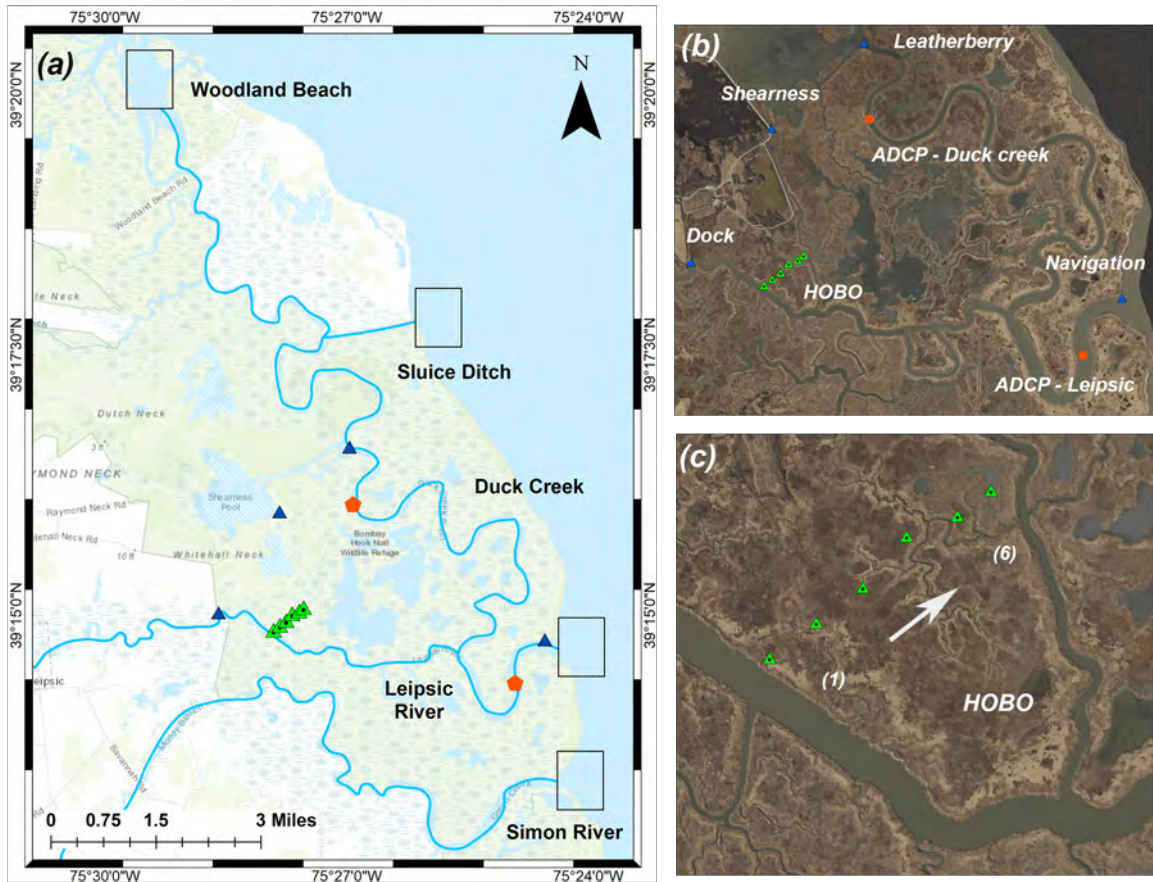
Figure 2.4: (a) Leipsic River, Simon River, Sluice Ditch/Duck Creek and Woodland Beach inlets that connect BHNWR wetland system with the Delaware estuary and Bay. The total volume flux going in/out of the system is estimated later using these four inlets. HOBO pressure gauges, DNREC tide gauges inside the wetland, and ADCP locations used for the model validation are shown in green triangles, blue triangles and orange pentagons; (b) Similar gauges are shown with more description; (c) A closer look to the HOBO pressure gauge locations.

2.3.3 Model validation

The model performance has been evaluated at point locations for a time frame from April to October 2015 and during two extreme events, in terms of water surface elevation in open water, marsh interior channels and on marsh flats. Also, we compared current velocity during April-May 2015 when two Acoustic Doppler Current Profiler

(ADCP) were deployed in two major channels, Leipsic River and Duck Creek. For the severe surge condition, two extreme meteorological events that threatened Delaware Bay with storm surge and large-scale coastal flooding, Hurricane Sandy (2012) and Hurricane Joaquin (2015) (Dohner et al., 2016), were selected. Hurricane Sandy made landfall as a Category 1 hurricane on the New Jersey coast near Brigantine, NJ in 2012 with a record setting water level and catastrophic flooding that resulted in an estimated property damage of 50 billion USD (Sullivan and Uccellini, 2013). Hurricane Joaquin initially made landfall in the Bahamas in 2015; however, then moved north-northeastward over the Atlantic Ocean and became embedded in the mid-latitude west-erlies (https://www.nasa.gov/feature/goddard/joaquin-atlantic-ocean). Although it stayed away from the US mainland and close to the shelf, there was intense rain-fall and both inland and coastal flooding in South Carolina, and storm surge up to 1.20 m in the Chesapeake Bay (Berg, 2016). The nearest bay-side tide gauge to BH-NWR at Ship John Shoal is chosen for model evaluation in Delaware Bay (https://tidesandcurrents.noaa.gov/waterlevels.html?id=8537121). Four DNREC tide gauges shown in Figure 2.4, are used for model evaluation in marsh interior channels. All gauges recorded data continuously for the entire year of 2012 and for a period of 7 months from April to October in 2015. Two ADCP gauges were deployed in Leip-sic River and Duck Creek during a short period of time in 2015, therefore the depth averaged current velocity field is compared for that separate time window. Model sim-ulations were performed separately for Hurricane Sandy, and the entire year of 2015 that included Hurricane Joaquin.

Comparison of surface elevation and current data sets at the gauge locations in the BHNWR and Delaware Bay are shown in Figures 2.5 and 2.10 where a generally good agreement between the model and in-situ data is obtained. Comparison with initial simulations with biased sub-tidal signals indicates that such correction being used in the forcing data could enhance model performance. First, we have compared model results with the entire 2015 in-situ data set to evaluate overall performance during a period that has both regular (tidal) and stormy (subtidal) conditions. The
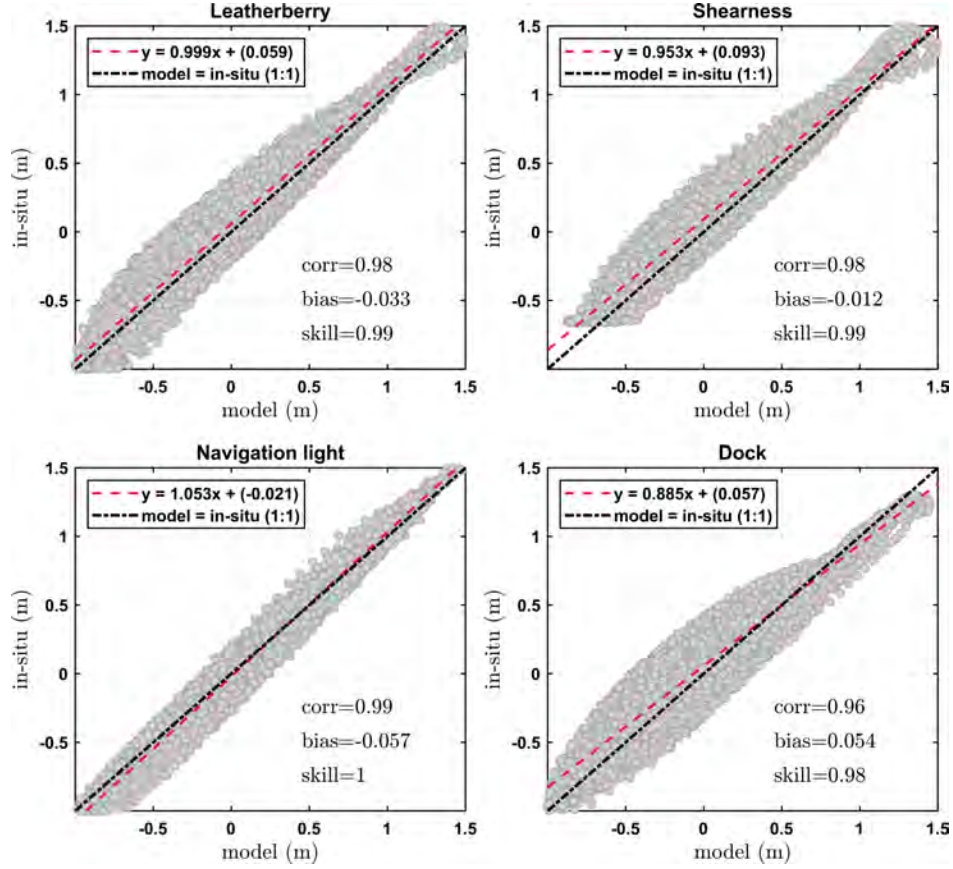
Figure 2.5: Scatter comparison (correlation, average bias index and skill) between FVCOM model and in-situ water surface elevation for the year 2015 at different DNREC tide gauges (in meters, from NAVD88 vertical reference level).

average bias index and model skill were computed using Equation 2.3.1 and 2.3.2, where

$$Bias = \frac{\sum_{n=1}^{N}(M_n - O_n)}{\sum_{n=1}^{N} O_n} \tag{2.3.1}$$

$$Skill = 1 - \frac{\sum_{n=1}^{N}(M_n - O_n)^2}{\sum_{n=1}^{N}(|M_n - O| + |O_n - O|)^2} \tag{2.3.2}$$

Where N is the total number of samples, M_n is the model result, O_n is the observed data and O is the mean of the observed data.

Tide gauge close to the Bay (Navigation Light) is observed to have a higher

correlation and skill score of 0.99 and 1.0, respectively, than the other interior gauges (Figure 2.5). The averaged bias index and slope of the regression line show that the model under-predicts during falling tide. Inside the wetland, scatter seems to increase at Leatherberry and Shearness, where the correlation coefficient and skill reduces to 0.98 and 0.99. Overall, they both show a similar trend where model under-predicts during high tide and then over-predicts at low tide. Moving further to the most up-stream gauge (Dock), model accuracy decreases more and now over-predicts during both tidal conditions, prominently during the low tide.

After looking into the model performance for a seven month period, we have parted it for different hurricane conditions to evaluate the bias primarily coming from subtidal signals and flawed marsh flooding and draining. To begin with, we looked into surface elevation time series during Hurricane Sandy and Hurricane Joaquin at Delaware Bay NOAA tide gauge location (Figure 2.6). The model skill is 0.99 for both events, and the negative sign on the low average bias index value represents a slight under-prediction by the model. We can see that the subtidal correction is much more accurate for Hurricane Joaquin compared to Hurricane Sandy, and has a smaller bias during the main surge event. The comparison at the BHNWR tide gauges is shown in Figure 2.7 for Hurricane Sandy, again revealing higher model skill at the tide gauge close to the Bay (Navigation Light). It shows an increase in the scatter at interior channel gauges when surge inundates the entire marsh platform. Some distinct scatter appears in all the interior gauges during one specific tidal cycle at the end of the surge, where the model overestimates surface elevation and also develops a phase lag due to gradual draining from the marsh platform.

Water surface elevation is collected along a transect on the marsh surface through-out the year 2015, using HOBO water level loggers. Locations of the HOBO gauges in the marsh are shown in Figure 2.4. The FVCOM model results are compared with in-situ data for Hurricane Joaquin at the four DNREC tide gauges (Figure 2.8) and on the marsh surface (Figure 2.9). A better model performance compared to the case of Hurricane Sandy is observed in three of the gauges, mainly at Navigation Light (close

19

to the Bay), Leatherberry and Shearness (located in the marsh interior). This could be due to a more accurate representation of the sub-tidal forcing at the boundaries and the channel bathymetry surveyed during the year 2015. Model skill and correlation score demonstrate a good agreement where both are close to 0.99. At Dock, we observed a significant deviation during falling tide (Figure 2.8, last subplot), also evident from the model correlation and skill that decreases to 0.96 and 0.95 respectively. The estimated regression slope and averaged bias index value show model over-estimation, that is mainly coming from a higher phase lag. The similar trend can be also noticed in longer-term comparison we have shown earlier.

The results at the six HOBO stations presented in Figure 2.9 show that FVCOM does a reasonable job of predicting maximum inundation depths over the marsh platform. However the model results show an elevated minimum depth compared to the in-situ measurements. A systematic error associated with marsh elevation shown by the red line cut off and model grid elevation shown by the horizontal black line, is seen. The differences between the base of the red and black lines are related to horizontal interpolation, resolution errors and smoothing from high resolution LiDAR data to get the model DEM, followed by an added error in interpreting local depth in a low order triangulated grid system. These errors are usually comparable to the vertical resolution errors that are inherent to the LiDAR measurement. From the surface elevation comparison, the model was seen to exhibit one particular problem during marsh draining phase, artificial ponding, where an extra water storage is apparent for the entire time at HOBO location 3 to 6. The model performance is further assessed for the current velocity variable at two ADCP locations. Figure 2.4 shows the instrument locations in Duck Creek and Leipsic River, BHNWR. The results are shown in Figure 2.10, revealing that the velocity outputs from the depth averaged FVCOM model agrees well with the collected velocity (depth averaged). Notably, a slight model under-prediction is observed during low water slack at the Leipsic River gauge, and during high water slack at Duck Creek.
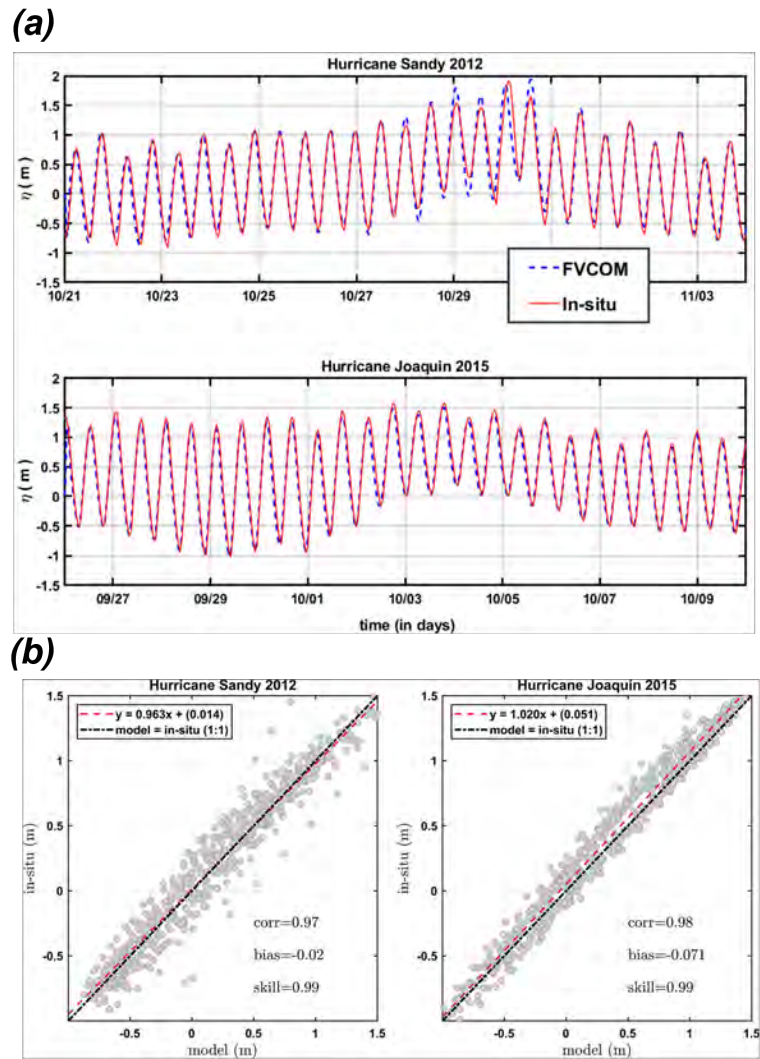
Figure 2.6: (a) Comparison between FVCOM model (in blue) and in-situ (in red) water surface elevation during Hurricane Sandy, 2012 and Hurricane Joaquin, 2015 at Ship John Shoal NOAA tide gauge in the Delaware Bay (in meters, from NAVD88 vertical reference level); (b) Scatter comparison (correlation, average bias index and skill) between FVCOM model and in-situ water surface elevation at the same gauge.
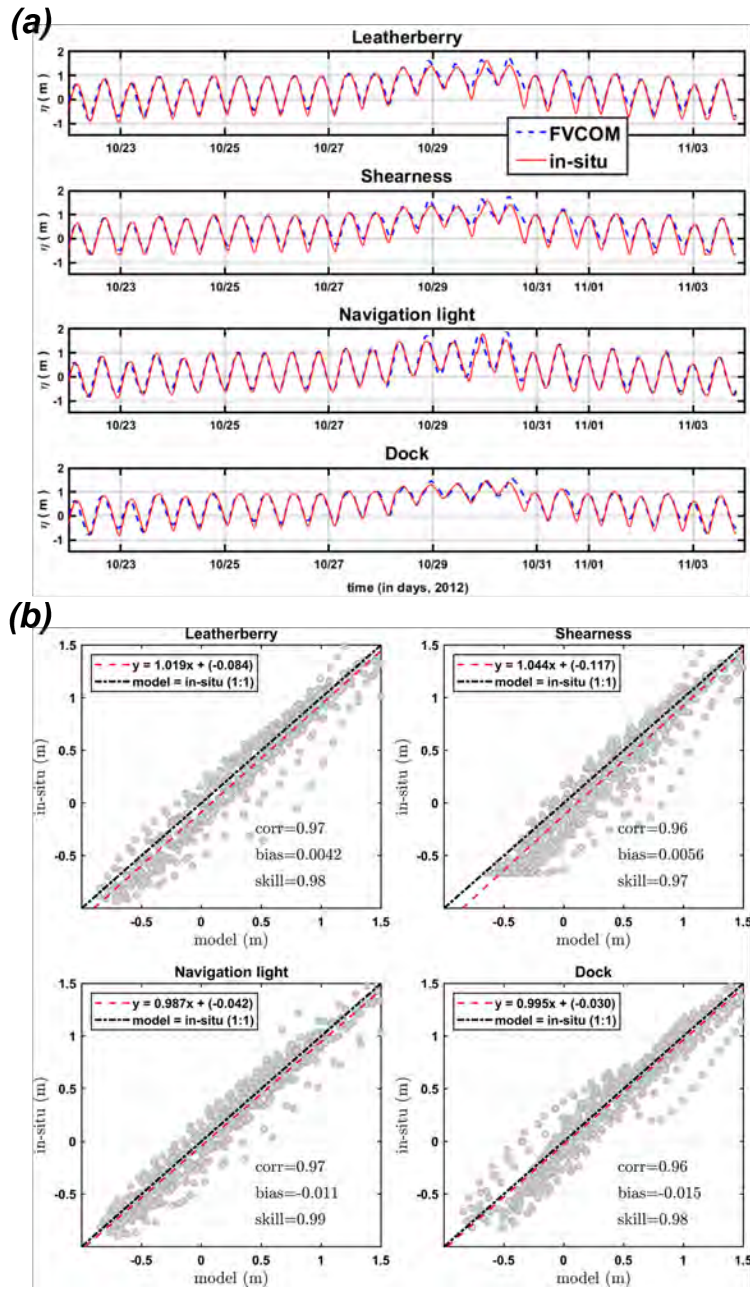
Figure 2.7: (a) Comparison between FVCOM model (in blue) and in-situ (in red) water surface elevation during Hurricane Sandy, 2012 at different DNREC tide gauges (in meters, from NAVD88 vertical reference level); (b) Scatter comparison (correlation, average bias index and skill) between FVCOM model and in-situ water surface elevation at the same gauges.
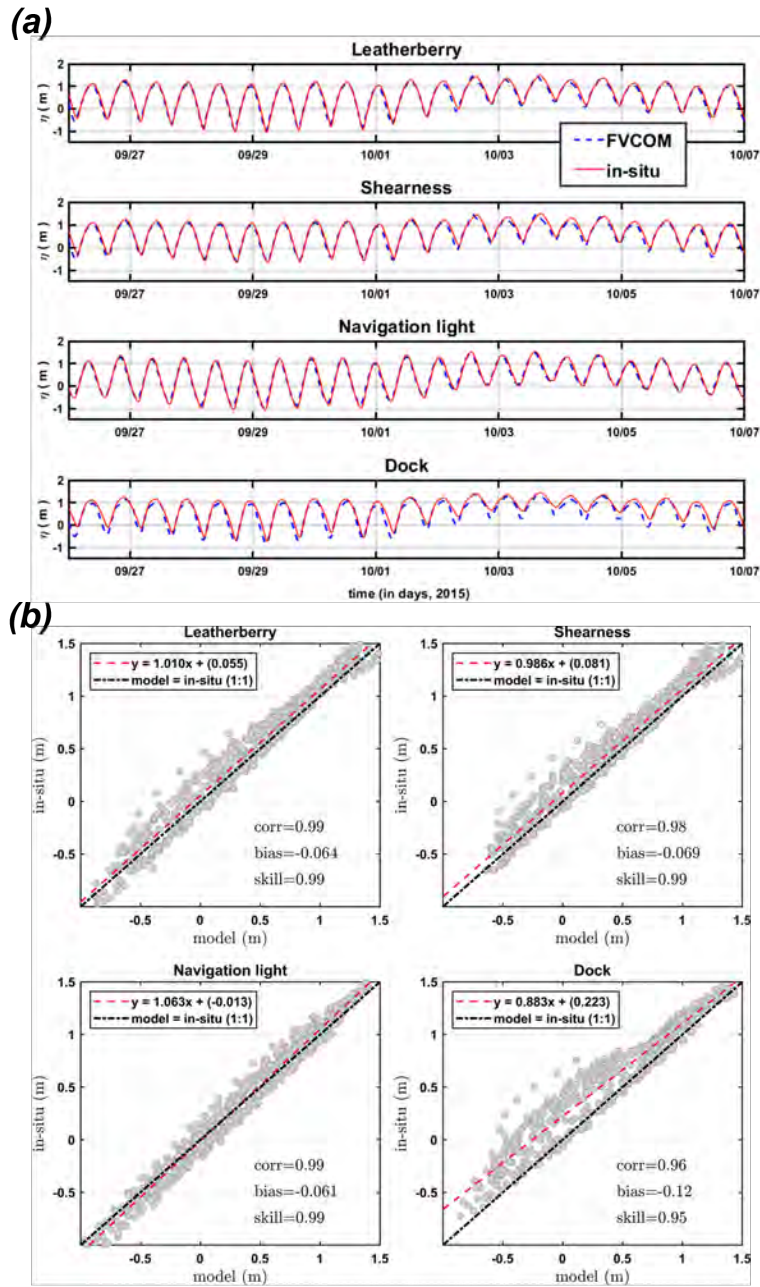
Figure 2.8: (a) Comparison between FVCOM model (in blue) and in-situ (in red) water surface elevation during Hurricane Joaquin, 2015 at different DNREC tide gauges (in meters, from NAVD88 vertical reference level); (b) Scatter comparison (correlation, average bias index and skill) between FVCOM model and in-situ water surface elevation at the same gauges.
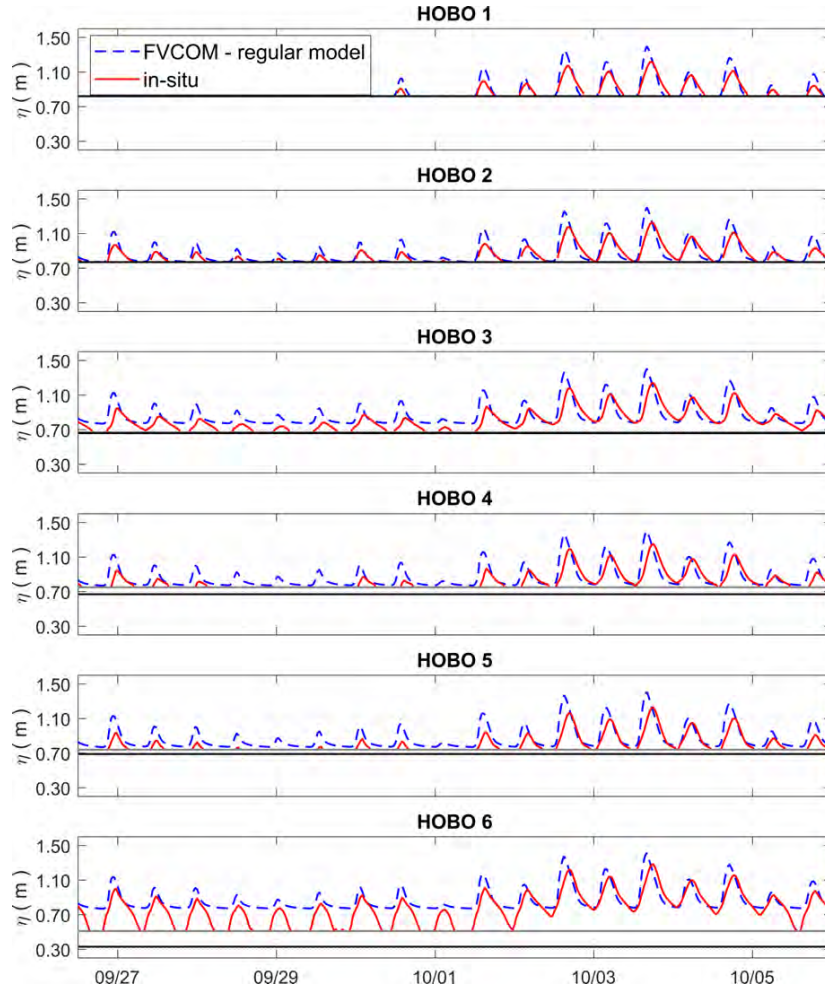
Figure 2.9: Comparison between FVCOM model (in blue) and in-situ (in red) water surface elevation during Hurricane Joaquin, 2015 at different HOBO gauge locations (in meters, from NAVD88 vertical reference level). The black straight and gray lines represent model grid bottom and surveyed elevation.
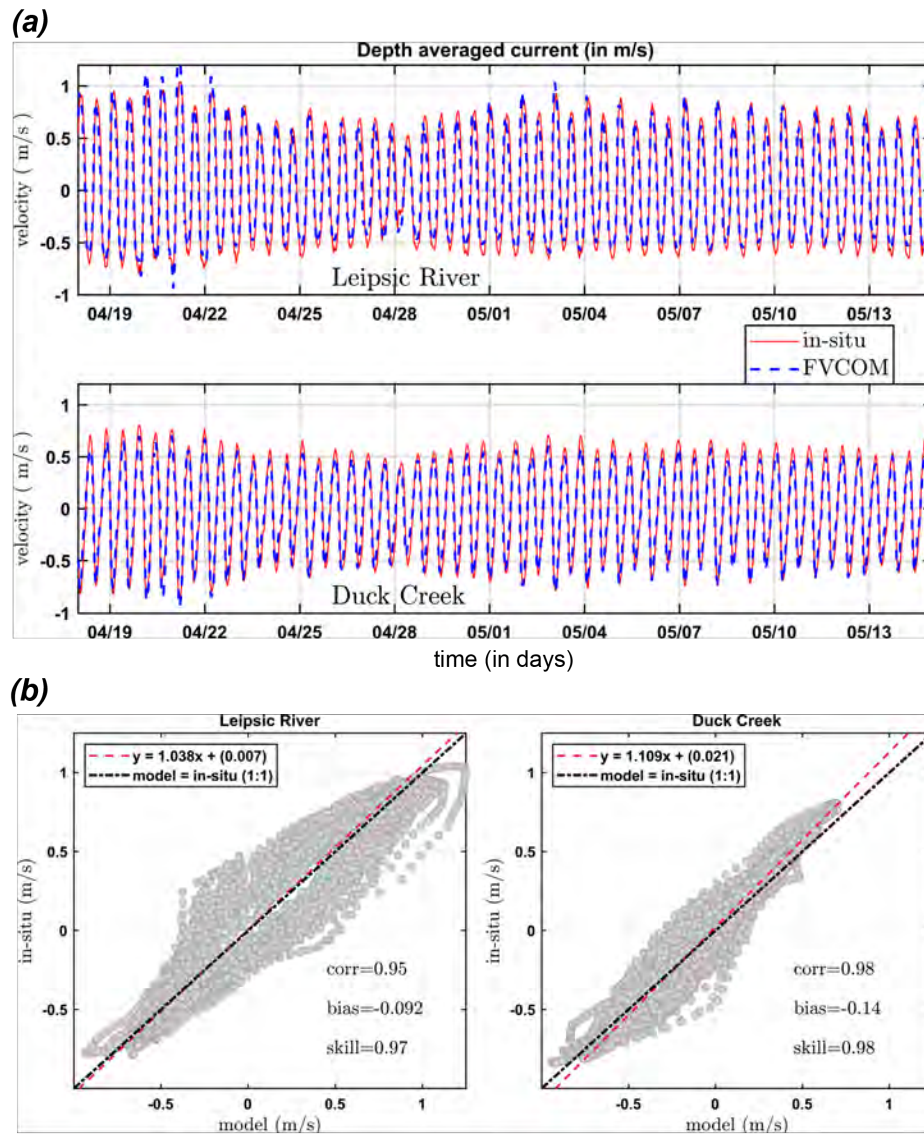
Figure 2.10: (a) Comparison between FVCOM model (in blue) and in-situ depth-averaged current data (in red) collected at different ADCP locations in Bombay Hook during April - May, 2015; (b) Scatter comparison (correlation, average bias index and skill) between FVCOM model and in-situ (in m/s).

2.4 Morphology scenario development and estimate of the tidal asymmetry

As shown in Figure 2.4a, the BHNWR area is connected to Delaware Bay through four different entrances, including Leipsic River, Simon River, Sluice Ditch/Duck Creek and Woodland Beach, which are connected to each other via interior channels of the wetland system. Of these, the Sluice Ditch channel is an artificially opened inlet (Dozier, 1947). The ongoing erosion events at the top and mid portion of the BHNWR, consisting Leipsic River, Sluice Ditch and Woodland Beach, have led to examine a few historical and morphological scenarios. Model simulations were carried out with changing morphology to describe the ongoing and future changes of hydrodynamics and tidal asymmetry. First, we hypothesized a historical case assuming channel bathymetry set to a maximum depth of 5 m throughout the entire wetland system, keeping it similar to the Simon River cross-section averaged bathymetry of the undisturbed region, and artificially filled the existing Sluice Ditch (Figure 2.11a, top polygon (1); 2.11b, top left). Then, considered a similar case of channel depth limited to 5 m, but introduced Sluice Ditch back into the system (Figure 2.11b, top right). This scenario is developed to illustrate the role of artificially opened Sluice Ditch in altering the hydrodynamics and enhancing transport processes in the eroding marsh system. Ultimately, both of them are compared to the baseline condition with current irregular channel bathymetry where mid-channel depth close is to 10.0 m in Leipsic River and Sluice Ditch (Figure 2.11b, bottom left). The first scenario is a step toward simulating historical conditions that were possibly in effect before the start of major erosional changes in the system. We have made no corresponding attempt to narrow channels or recreate river oxbows that have been straightened. We also note that the tidal flat areas such as Money Marsh would have been areas of continuous marsh platform (depression like), further reducing the available volume for tidal exchange. Finally, we considered the effect of the opening of a new entrance along Duck Creek due to progress shoreline erosion on the bay shoreline (Figure 2.11a, bottom polygon (2); 2.11b, bottom right). Here, we have provided an arbitrary inlet depth of 2 m, and the inlet width and orientation are

26

extracted from a current imagery of the internal erosion (Figure 2.11a, bottom polygon (2)).

To look into the tidal asymmetry and flood/ebb dominance of the system, a month long simulation for an entire spring-neap cycle is done under regular tidal forcing that produces minimum marsh artificial ponding (i.e., M_2 and S_2 tidal constituents taken from a nearest NOAA tide gauge). All model parameters were kept the same as described earlier in section 2.3.2. The inlets can show cross-channel spatial asymmetry, therefore, the total volume flux going in and out of the system is calculated across each inlet and shown in Figure 2.12, along with the mid-channel velocity to show the nature of hydrodynamics at the deeper part. We have quantified an asymmetry parameter γ_0 following Nidzieko and Ralston (2012) using the time derivative of surface elevation (η_t), mid-channel velocity (U) and net flux (Q) from each inlet to represent the duration asymmetry, and velocity and flux skewness for each tidal cycle (using a 12.42 hour window). Nidzieko and Ralston (2012) calculated second and third moment from the observed time series data sets (surface elevation and velocity) and prescribed the asymmetry parameter as

$$\gamma_0 \equiv \frac{\mu_3}{\mu_2^{3/2}} \tag{2.4.1}$$

where the k-th moment from zero can be defined as

$$\mu_k = \frac{1}{N-1} \sum_{i=1}^{N} (n_i)^k \tag{2.4.2}$$

Here, N is the number of samples n_i. The tide is ebb dominant for $\gamma_0(U) < 0$ and flood dominant for $\gamma_0(U) > 0$ (U is the depth averaged velocity), and the duration of falling water is longer than rising if $\gamma_0(\eta_t) > 0$.
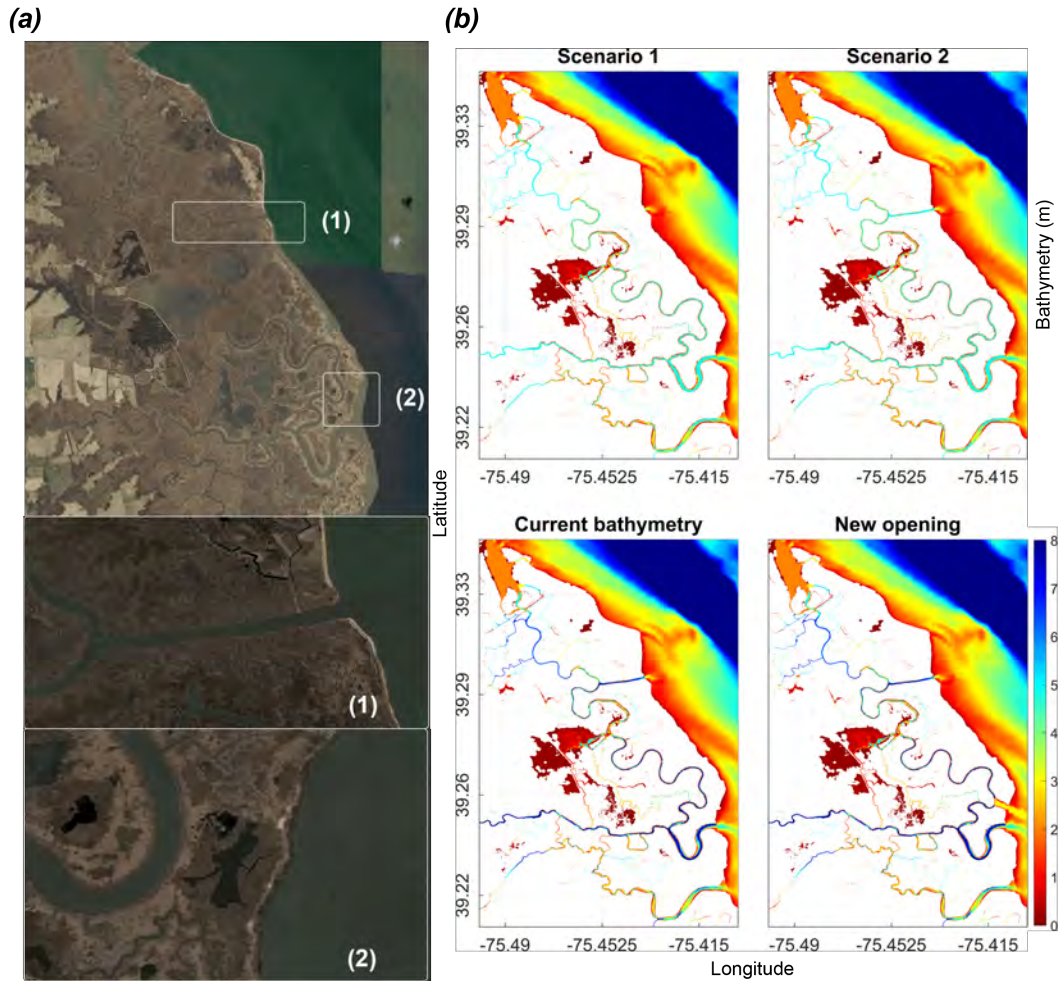
Figure 2.11: (a) Two inlet entrances used for morphology scenario analysis in this study: the middle subplot shows the artificially dredged Sluice Ditch (in 1890) and the bottom subplot shows a potential new entrance from shoreline erosion; (b) Different channel morphology conditions (in meters, from NAVD88 vertical reference level): Scenario 1 - No Sluice Ditch and channel depth 5 m, Scenario 2 - with Sluice Ditch and depth 5 m, Current bathymetry, Current bathymetry with the new opening.

2.5 Results and discussion

2.5.1 Changes in the overall hydrodynamics from a man-made channel construction

For the first scenario, all the inlets are observed to be flood dominant based on the duration asymmetry. The tidal amplitude and phase in inlet locations were almost identical for all the scenarios; hence we have shown only surface elevation from current bathymetry in the comparisons in Figure 2.12. This can be evident from Figure 2.13, where we can see that $\gamma_0(\eta_t) > 0$ everywhere. Leipsic and Simon River inlet both show ebb dominant velocity skewness. Figure 2.12a.2 (green curves) shows, in Leipsic River inlet, the timing of slack water shifts during ebb tide and produces a higher velocity skewness at the deeper part. Interestingly, the volume flux comparison shows a different response (Figure 2.12a.1), where the flux magnitude decreases during ebb tide, making the flux variation much more symmetric. So, we can see with a reduced thalweg depth and the along and across-channel bathymetry gradient, the Leipsic inlet shows an increase in ebb dominant velocity skewness (higher negative velocity skew) at the mid-channel, while the net flux displays less asymmetry due to higher flood dominance close to the banks (Figure 2.12a.1,2 and 2.13). There is much less effect of asymmetry during neap tide conditions, shown in the corresponding stage-discharge results in Figure 2.12b. Woodland Beach, currently a flood dominant inlet during neap tides (based on all γ_0 values), shows an increase in flood dominance for the entire inlet based on volume flux skewness during both spring and neap, where at the deeper part the velocity showing slight ebb dominance during spring tide (Figure 2.13).

When Sluice Ditch is reintroduced into the bathymetry of the first scenario (with the limitation to 5m depth), the total instantaneous flux going in or out of the Leipsic River becomes more asymmetric during both spring and neap conditions (Figure 2.13b). It means that the introduction of Sluice Ditch has increased Leipsic inlet volume flux ebb dominance, while reducing the mid-channel velocity ebb skewness to some extent. Response at the Woodland Beach inlet also shows a reduced volume flux flood dominance compared to the previous case with Sluice Ditch closed. In

29

addition, the newly opened Sluice Ditch inlet shows a strong ebb dominance at the deeper part based on velocity skewness, compared to a less asymmetric volume flux due to flood dominant channel banks. The opening of Sluice Ditch also has a pronounced effect on tidal range in all areas of the system aside from those most adjacent to the Leipsic and Woodland Beach entrances, with the tide range doubled in some instances along Duck Creek and at the entrance into Money Marsh, shown in Figure 2.14a. The increase in tide range is specifically coming from the decrease of mean low water along the Duck Creek (Figure 2.15a, Leatherberry), even without the affect of depth change. The opening reduces the maximum velocity in some instances along Leipsic River and Duck Creek up to the entrance of Money Marsh mudflat area, however caused a dramatic increase in the maximum velocity from there to the vicinity of the inlet (Figure 2.14c). From the Leatherberry mid-channel velocity shown in Figure 2.15b, we can see that the velocity magnitude skewness has increased and became more ebb dominant with the opening of Sluice Ditch.
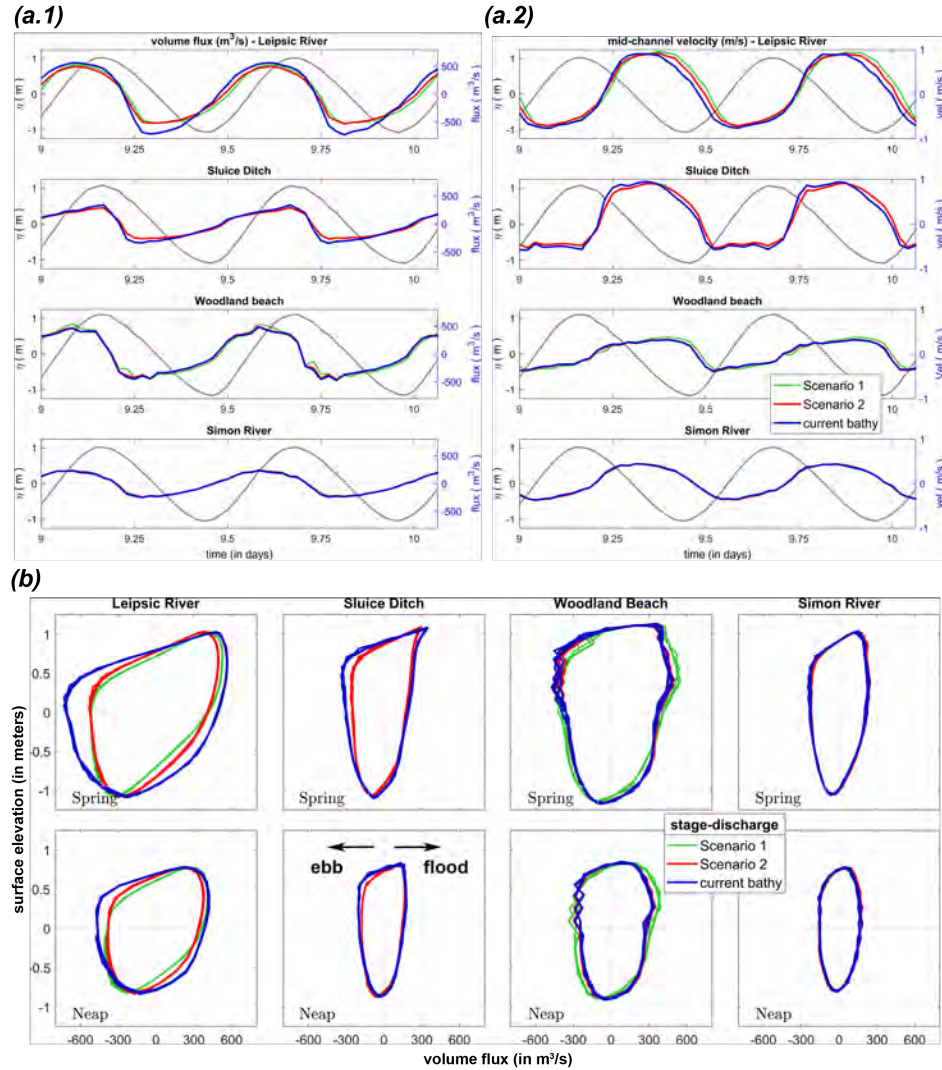
Figure 2.12: (a) Volume flux (in m³/s) going in/out through BHNWR inlets and the respective mid-channel velocities. First subplot a.1 shows flux magnitude during a spring cycle for different inlets. The color straight lines represent flow conditions based on different morphology scenarios (Green: Scenario 1 - No Sluice Ditch and depth 5 m, Red: Scenario 2 - with Sluice Ditch and depth 5 m, Blue: Current bathymetry). Second subplot a.2 represent the mid-channel velocity for the same inlets. Surface elevation from respective inlet entrance location (referenced to NAVD88, in meters) is shown with the solid gray line; (b) Stage-discharge relationship at the four inlets during spring and neap tide conditions (here, positive flux represents going into the wetland, negative represents going out).
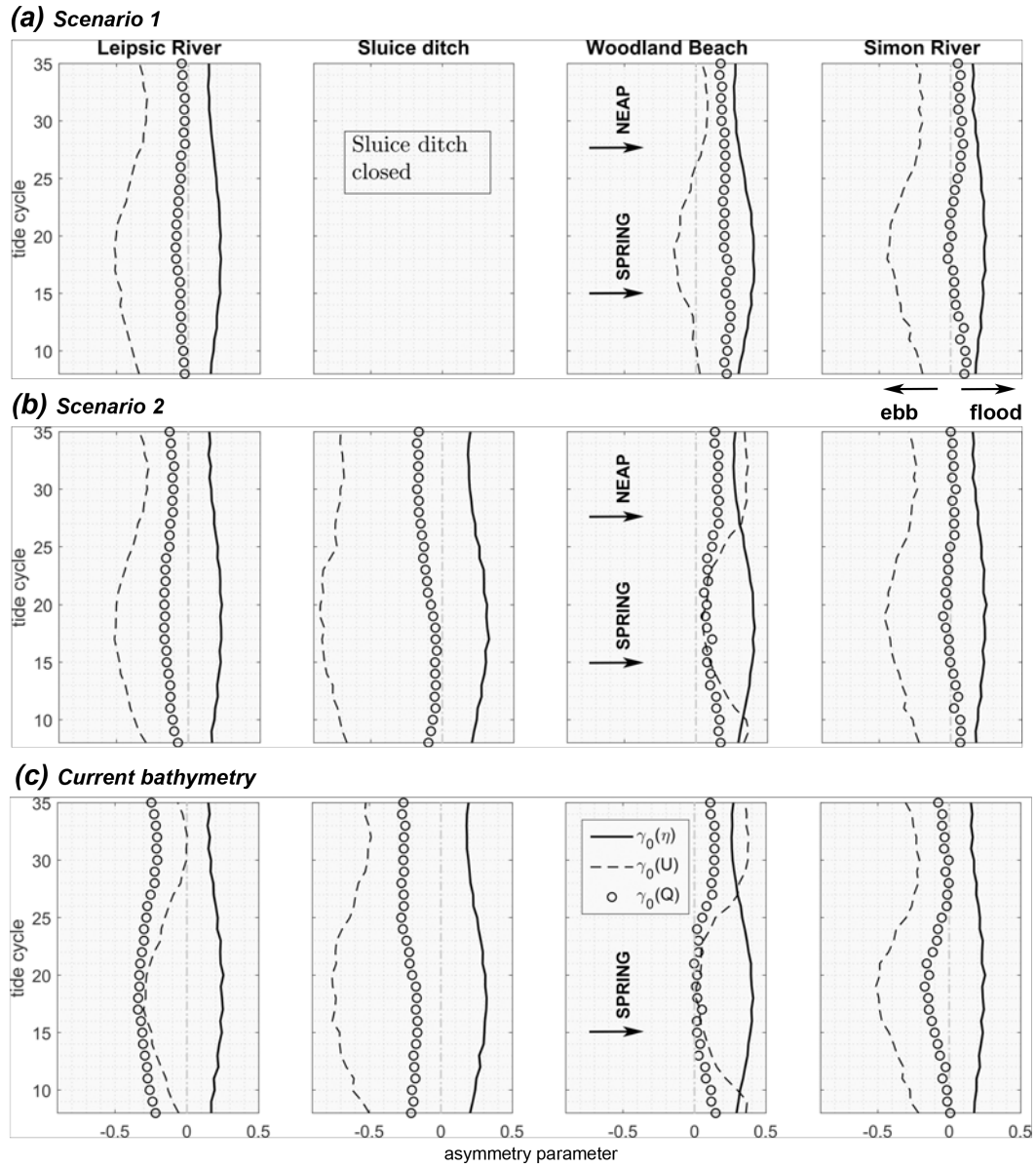
Figure 2.13: Asymmetry parameter γ_0 calculated following the equations given by Nidzieko and Ralston (2012). Here, $\gamma_0(\eta_t)$ represents the duration asymmetry, $\gamma_0(U)$ is the depth averaged velocity skewness, and $\gamma_0(Q)$ is the integrated inlet volume flux skewness. The tide is ebb dominant for $\gamma_0(U) < 0$ and flood dominant for $\gamma_0(U) > 0$, and the duration of falling water is longer than rising if $\gamma_0(\eta_t) > 0$.
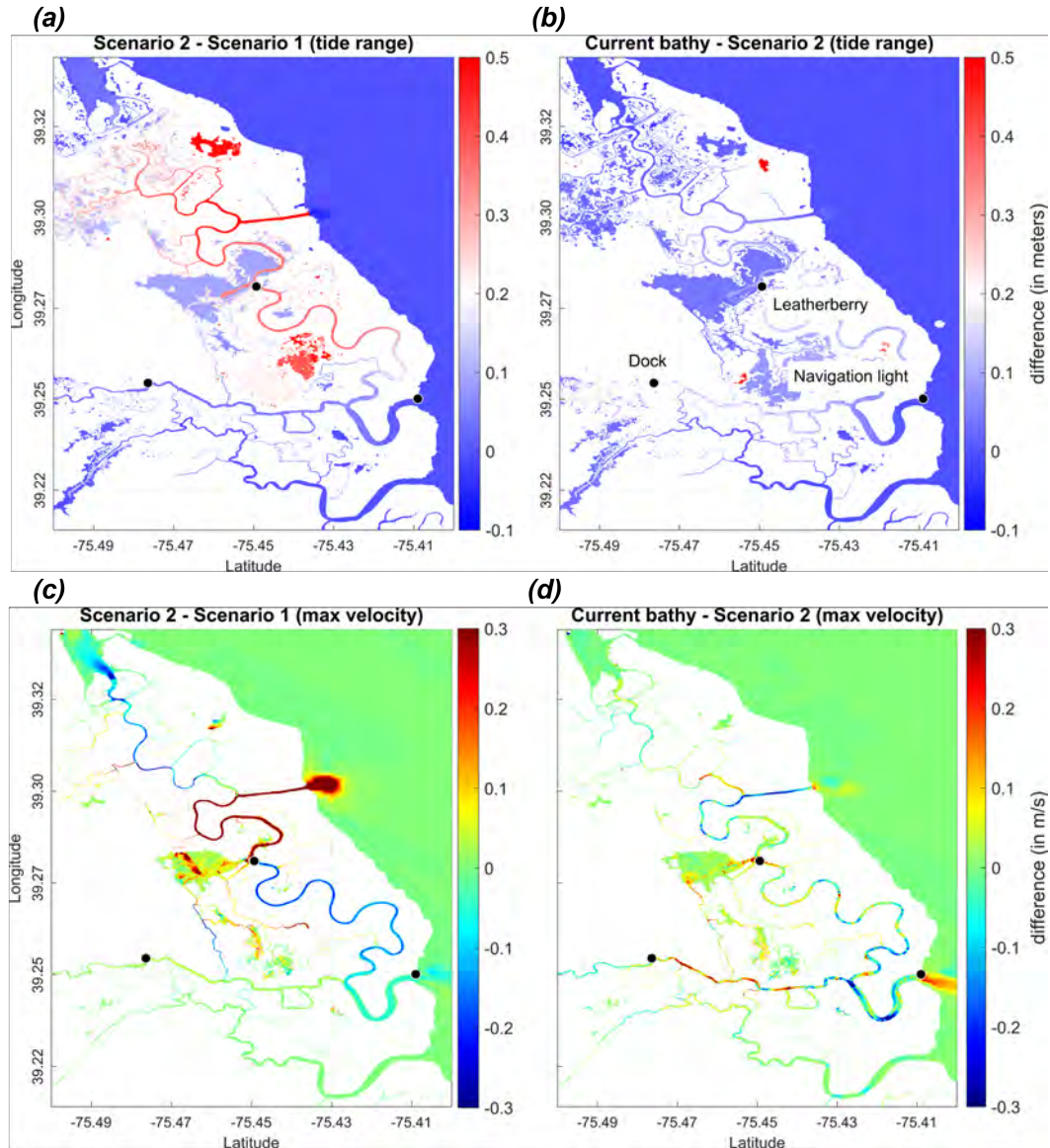
Figure 2.14: (a) Changes to the tide range from artificial dredging of Sluice Ditch (in meters). The tide range estimated from Scenario 1 (No Sluice Ditch and depth 5 m) is subtracted from the tide range of Scenario 2 (with Sluice Ditch and depth 5 m); (b) Similar subtraction is done between Scenario 2 and current bathymetry (in meters); (c) Changes to the maximum velocity from artificial dredging of Sluice Ditch (in m/s). Here, the maximum velocity magnitude for the case of Scenario 1 (No Sluice Ditch and depth 5 m) is subtracted from the maximum velocity magnitude of Scenario 2 (with Sluice Ditch and depth 5 m); (d) Similar subtraction is done between Scenario 2 and current bathymetry (in m/s).
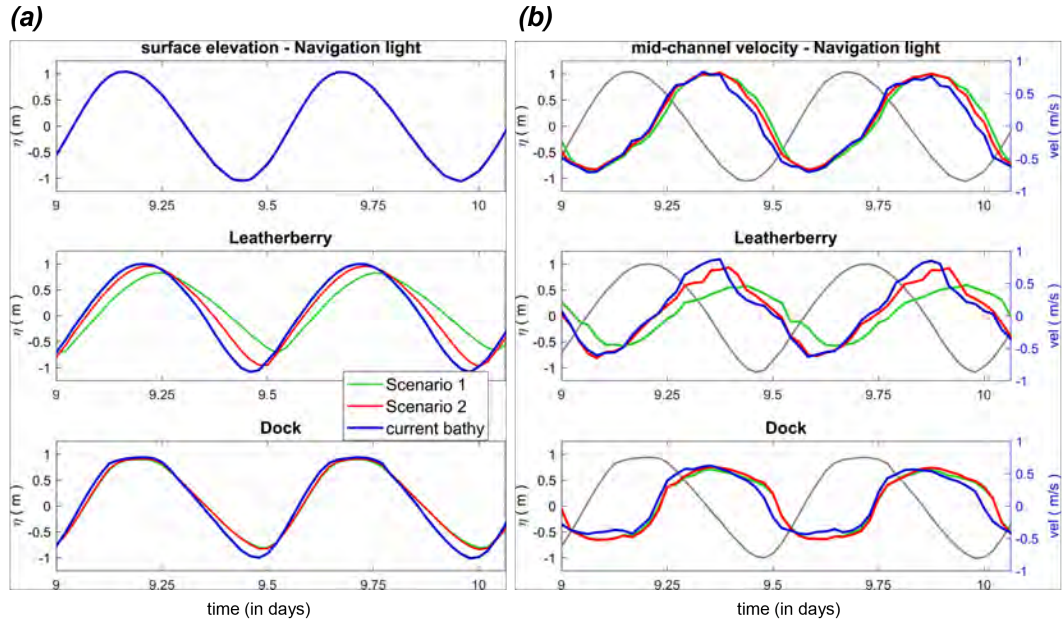
Figure 2.15: (a) Model surface elevation for different morphology scenarios at interior tide gauge locations during a spring cycle (in meters, from NAVD88 vertical reference level). Green: Scenario 1 - No Sluice Ditch and depth 5 m, Red: Scenario 2 - with Sluice Ditch and depth 5 m, Blue: Current bathymetry; (b) Mid-channel velocity for different morphology scenarios at the same gauges (in m/s). Surface elevation for current bathymetry scenario (referenced to NAVD88, in meters) is shown with the solid gray line to represent the flood and ebb tide.

Now, to understand these changes in the system's interior from the artificial opening in a mechanistic way, we have also used a simple inlet-channel-bay model that connects the wetland interior to the offshore by separate inlets. The Money marsh mudflat (where Leatherberry tide gauge is located) acts like a small Bay system which in reality is connected to the Delaware Bay by two separate major inlet channels, both in the first and second scenario. The major difference between both scenarios can be understood from Figure 2.16a. We can see the dramatic change in the ocean-inlet-bay system after introducing the new channel, where the interior now has a much shorter connection and higher depth for the tidal exchange compared to the first scenario. Here, we use the ocean-inlet-bay analytical model proposed by Aretxabaleta et al. (2017) to

34

evaluate the first-order response of the bay to ocean sea level forcing. Aretxabaleta et al. (2017) studied a similar shallow estuarine system in southern Long Island, New York along the Atlantic Ocean, and developed the bay water level expression (Equation 2.5.3) using along-channel depth-averaged momentum equation. Based on the simple balance between local inertia, frictional effects and pressure gradient, the momentum and continuity equations can be written as

$$\frac{\partial u_n}{\partial t} = g\frac{(\eta_o - \eta_e)}{L_n} - \frac{r_n}{h_n}u_n \tag{2.5.1}$$

$$A_e\frac{\partial \eta_e}{\partial t} = \sum h_n W_n u_n \tag{2.5.2}$$

where A_e and η_e are the surface area and sea level in the bay; η_o the sea level in the ocean; with h_n the water depth; u_n the depth-averaged velocity; W_n the width and L_n the length of channel n, and r is the linear drag coefficient ($\approx \frac{8c_d}{3\pi}u$), for $n = 1, 2$.

Assuming $\eta = \eta e^{i\omega t}$ and $u = u e^{i\omega t}$ yields the following equation:

$$\eta_e = \eta_o \left\{ \frac{\frac{h_1 W_1 g}{L_1\left(\frac{r_1}{h_1}+i\omega\right)} + \frac{h_2 W_2 g}{L_2\left(\frac{r_2}{h_2}+i\omega\right)}}{i\omega A_e + \frac{h_1 W_1 g}{L_1\left(\frac{r_1}{h_1}+i\omega\right)} + \frac{h_2 W_2 g}{L_2\left(\frac{r_2}{h_2}+i\omega\right)}} \right\} \tag{2.5.3}$$

where, w is the radian frequency of the ocean tidal oscillation and $\frac{r_n}{h_n}$ is the characteristics frequency of frictional dissipation in the channel. From the denominator in the Equation 2.5.3, we can also estimate the undamped natural frequency w_N of the interior bay (Helmholtz frequency) as

$$\omega_N = \left(\frac{h_1 W_1 g L_2 + h_2 W_2 g L_1}{A_e L_1 L_2}\right)^{1/2} \tag{2.5.4}$$

As the characteristics frequency of channel frictional dissipation increases from lower depth and higher friction, it reduces the frictional adjustment time and increases the interior amplitude damping. According to Chuang and Swenson (1981), when

Table 2.1: Channel-Bay properties inside BHNWR, Tidal period, T = 12.42 hrs; Money marsh mudflat area, $A_e = 1.0 \times 10^6\ m^2$; Drag coefficient, $r = 3.0 \times 10^{-3}$.

	$W1$	$h1$	$L1$	$W2$	$h2$	$L2$	w_n	$\frac{r_n/h_n}{w_n}$
Scenario 1	100m	5m	17km	200m	2m	19km	3.96×10^{-4}	5.4
Scenario 2	100m	5m	17km	100m	5m	10km	4.96×10^{-4}	2.4
Current bathy	100m	8m	17km	100m	10m	10km	6.75×10^{-4}	1.0

$\frac{r_n/h_n}{w_N} > 1.0$, the range of water level variation inside the bay is always less than the ocean, and for a $\frac{r_n/h_n}{w_N} \leq 1.0$ the response is opposite.

Based on the ocean-inlet-bay properties in our first and second scenario and ocean surface elevation from the FVCOM model, we have estimated the changes in channel frictional dissipation, natural frequency of the system and the decay time (Table 2.1). The analytical model result is shown in Figure 2.16b for different morphology scenarios, and we can see that the amplitude response η_e in the bay (marsh mudflat) mimic results seen from the numerical model in Figure 2.15a (Leatherberry gauge). To check the primary role of the inlet length and depth only, we kept the linear drag coefficient equal to 3.0×10^{-3} that normally varies based on the channel depth. The ratio of amplitude decay time $\frac{r_n}{h_n}$ and undamped natural frequency w_N is observed to be 5.4 for the first scenario due to the shallow ($h_2 \sim 2.0m$) and long ($L_2 \sim 19km$) inlet channel going toward the Woodland Beach. After adding the man-made channel (Sluice Ditch), we can see that the shorter and deeper side ($h_2 \sim 5.0m$ and $L_2 \sim 10km$) has reduced the characteristics frequency of channel frictional dissipation, increased the natural frequency, and ultimately reduced the ratio to 2.4. From the surface elevation comparison in Figure 2.16b, we can see a bigger tidal range and reduced bay amplitude damping compared to the first scenario, also shown in FVCOM results (Figure 2.15a).
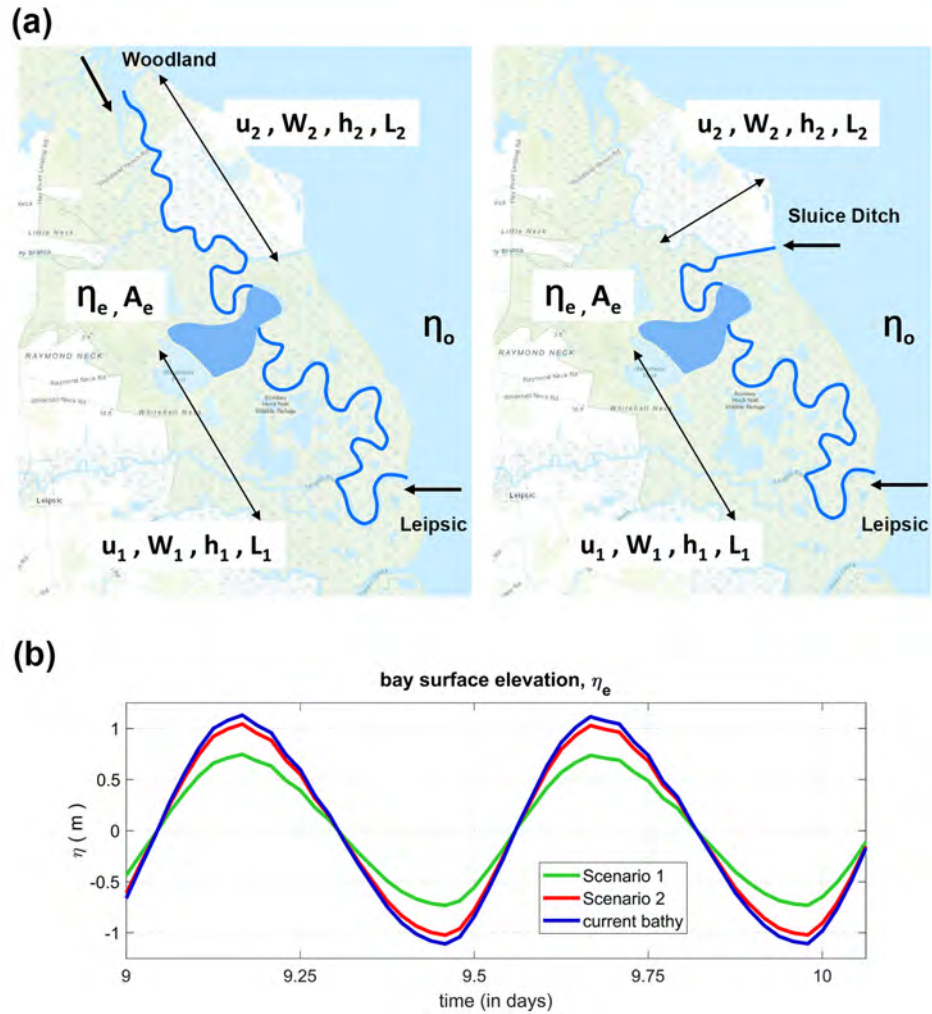
Figure 2.16: (a) Diagram of the ocean-inlet-bay system inside BNNWR; left subplot: Scenario 1 - No Sluice Ditch, and the interior is connected via Lepsic River and the Woodland beach inlet; right subplot: Scenario 2 and current bathymetry - after introducing Sluice Ditch; (b) Surface elevation, η_e for different morphology scenarios at the Money Marsh mudflat using the analytical model (in meters, from NAVD88 vertical reference level).

2.5.2 Effect of channel hypsometry changes over time

Comparing the present-day conditions (i.e., deeper channels) with second scenario, we can see that the volume flux is more asymmetric and ebb dominant. The tide range has progressively increased from mean low water decrease at the upstream side of Leipsic River, and close to the Money marsh mudflat (Figure 2.14b), while the maximum velocity change is observed to have a spatially varying response (Figure 2.14d). It provides an important insight on the affect of spatially varying channel thalweg bathymetry in changing the overall wetland interior and inlet flood/ebb dominance. The results ultimately show that the progressive deepening of channels within the marsh has led to a progressively increasing tendency towards volume flux ebb-dominance in the overall system, even though the velocity skewness at the mid-channel reduces. Woodland Beach, a flood dominant inlet in the case of both first and second scenario, also shows a decrease in flood dominance based on volume flux skewness during both spring and neap (Figure 2.13). The Woodland Beach inlet side is usually much shallower than 5 m and the bathymetry was not affected in the second scenario. The change in flux and velocity skewness clearly came from the increased velocity skewness in the connecting channel to Leipsic River. To recheck the flood/ebb dominance, the stage-discharge relationship at all the inlets are shown in Figure 2.12b, revealing that Leipsic river inlet is the major contributor to the system and has a strong ebb dominance. Corresponding stage-discharge results for neap tide are shown in Figure 2.12c, where much less effect of asymmetry during neap tide conditions is observed. At the marsh interior tide gauges, Leatherberry and Dock (Figure 2.15b,c), we can see that the tide range has increased along the channel compared to the shallower bathymetry, and the increase again is coming from the asymmetric response where the mean low water increased more compared to the decrease in mean high water. Familkhalili and Talke (2016) and Ralston et al. (2019) have observed a similar scenario in Cape Fear River Estuary, NC and Hudson River Estuary respectively, where the channel deepening by dredging has increased the tidal range by decreasing the effective drag and increasing hydraulic conveyance. In addition, from the mid-channel velocity comparison shown

in Figure 2.15b (blue line), we can see that the interior gauge Leatherberry shows a ebb dominant velocity skewness from the increased depth.

It is not trivial to explain the observed changes at different locations using simple analytical models because of the rapidly varying channel thalweg bathymetry and three inlets internally connected to each other. The increased ebb dominance at the Leipsic inlet is coming from a combined affect of reduced friction and increased net transport from the interior channel Duck Creek (Figure 2.17a). Previously, for the shallower conditions (second scenario), the interior channel has a lesser influence from the Leipsic inlet side and the interior drained via the shorter route Sluice Ditch. Now, with a much higher channel depth and tidal wave speed, the low tide travels through the Leipsic River, has an increased draining of the marsh interior and ultimately shows an ebb skewness at the inlet. Also, the overall volume flux is higher for the present condition which travels faster during flood due to the reduced friction, and the draining speed is also higher at the beginning of the ebb.

(a)

(b)
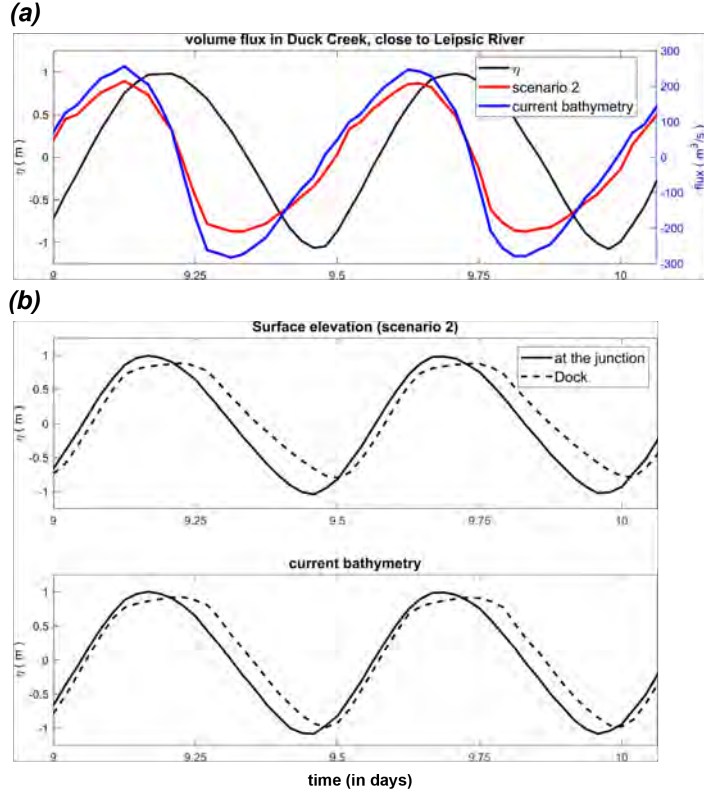
Figure 2.17: Changes in internal volume flux and surface elevation from channel deepening; (a) Volume flux (in m³/s) going in/out through Duck Creek that connects Leipsic River and Sluice Ditch; (b) Surface elevation changes along a short stretch in Leipsic River (referenced to NAVD88, in meters).

The stretch from the Leipsic River and Duck Creek junction to the Leipsic River u/s tide gauge can be considered as a straight river reach to use it to demonstrate the changes in the frictional dominance. For a channelized tidal estuary, Friedrichs and Madsen (1992) express the cross-sectionally averaged momentum equation as

$$\frac{\partial u}{\partial t} + u\frac{\partial u}{\partial x} + g\frac{\partial \eta}{\partial x} + \frac{C_d u|u|}{\eta + h} = 0 \qquad (2.5.5)$$

where, h is the cross-sectionally averaged depth of channel; η is the surface elevation; u is the cross-sectional average velocity; and C_d is the drag coefficient. Scaling the tidal amplitude with ξ, velocity with U, time with the tidal period T, x with a

Table 2.2: Scales and Parameters for the Leipsic River reach

Bathymetry	$U_0(m/s)$	ϵ	F^2	I	S	R
Scenario 2	0.5	0.26	8.5×10^{-3}	0.032	0.022	0.512
Current bathy	0.5	0.2	5.0×10^{-3}	0.025	0.017	0.24

characteristic length scale L, characteristic depth scale H, we define non-dimensional variables $x_0 = x/L$, $t_0 = t/T$, $u_0 = u/U$, $h_0 = h/H$, $\eta_0 = \eta/\xi$. In terms of these scaled variables, Equation 2.5.5 becomes

$$S\frac{\partial u_0}{\partial t_0} + I u_0 \frac{\partial u_0}{\partial x_0} + \frac{\partial \eta_0}{\partial x_0} + R\frac{u_0|u_0|}{h_0 + \epsilon\eta_0} = 0 \qquad (2.5.6)$$

The non-dimensional parameters S, I and R are given by

$$S = \frac{1}{\epsilon}\frac{F^2 L}{UT} \qquad (2.5.7)$$

$$I = \frac{F^2}{\epsilon} \qquad (2.5.8)$$

$$R = \frac{F^2 C_d L}{\epsilon H} \qquad (2.5.9)$$

where $\epsilon = \xi/H$ and F is the Froude number $U/\sqrt{gH}$.

From our chosen channel reach we have noticed that the tidal amplitude is $0.8m$ and $1.0m$, and cross-sectionally averaged channel depth is $\sim 3.0m$ and $\sim 5.0m$ for the second scenario and the current bathymetry respectively. Using the characteristic scales in the Leipsic River: $L = 16km$, $T \sim 12.42hrs(\sim 45000sec)$, $C_d = 3 \times 10^{-3}$, and $U \sim 0.5m/s$, we have observed that the local inertia S and the advective term I both are in same order. The ratio of tidal amplitude to the mean depth ϵ in all of the above terms (Equation 2.5.7-2.5.9) is seen to be two orders of magnitude larger than F^2 for both bathymetry conditions.

From Table 2.2, we see that friction dominates inertia for both cases where R is an order of magnitude bigger than S and I. So, for the selected reach of the Leipsic

River, the increase in mean low water can be simply explained using a balance between the sea surface gradient and channel friction as

$$g\frac{\partial \eta}{\partial x} + \frac{C_d u |u|}{\eta + h} = 0 \tag{2.5.10}$$

From Equation 2.5.10 we can see that for a higher depth and lower friction, the surface pressure gradient decreases along the channel, also observed in the surface comparison in (Figure 2.17b). While there is a reduced frictional effect for both second scenario and current bathymetry during high tide, it becomes dominant during ebb tide for the shallower conditions and increases the surface slope. Finally, the overall changes in the wetland hydrodynamics from the artificially opened channel and the progressive deepening can be also better understood if we look into Simon River inlet, which is mostly separated from the multi-inlet system (Figure 2.4) and is not a major factor in overall circulation of the disturbed part of BHNWR. From Figure 2.12 and 2.13, we can see that the channel volume flux is almost in a perfect symmetry during both spring and neap conditions, while the mid-channel velocity shows a tendency toward ebb dominance, and it stays unaffected from our scenario analysis as most of the channel reach has a bathymetry less than 5 m.

2.5.3 Potential of a new inlet opening from shoreline erosion

The net flux going in/out of the wetland seems to remain unchanged from the estimate with present morphology, with about the same degree of spring tide asymmetry. However, hydrodynamics in the Leipsic River changes dramatically. Velocity and flux through Leipsic River is reduced by almost half during both spring and neap tide (Figure 2.18d). Surprisingly, this new opening has a minimal influence on the other three inlets. From the spatial distribution shown in Figure 2.18a,b, we can see that the tidal prism is almost similar to the case with current bathymetry, while the velocity magnitude decreases significantly in the Leipsic River and in the stretch of Duck Creek connecting the Leipsic River to the new entrance. The new entrance is seen to divert the majority of the Duck Creek flow that originally passed through the Leipsic River entrance, leading to a dramatic reduction in maximum velocities in the Leipsic River itself. Meanwhile, in contrast to the stretch of new entrance connecting the Leipsic River, the velocity magnitude increased between the new entrance and Money marsh mudflat in the Duck creek. It can cause a different trend in the sediment transport and channel morphological evolution in the entire system where the Duck creek reach close to the mudflat will erode more, possibly also leading to a higher mudflat expansion, while the segment from new entrance to the Leipsic river inlet will see more deposition and depth decrease. Figure 2.19 show the instantaneous volume flux and velocity in each of the five open inlets. Volume flux through the new opening is comparable to flux in the Leipsic River, and the flux in either case is reduced to a value comparable to that of the Simon River during flood stage. The new entrance, along with the Leipsic River and Sluice Ditch, remain ebb dominant while decreasing the Leipsic River inlet asymmetry. Ultimately, this scenario shows that the new entrance from shoreline erosion could change the existing internal hydrodynamics, inlet asymmetry and transport processes in the disturbed part of the wetland, and the Simon River (undisturbed part) stays unaffected again. It is important to note that the results shown here with the new entrance reflects a response to the given arbitrary condition and it could easily change depending on the bathymetry distribution and orientation with the Bay.
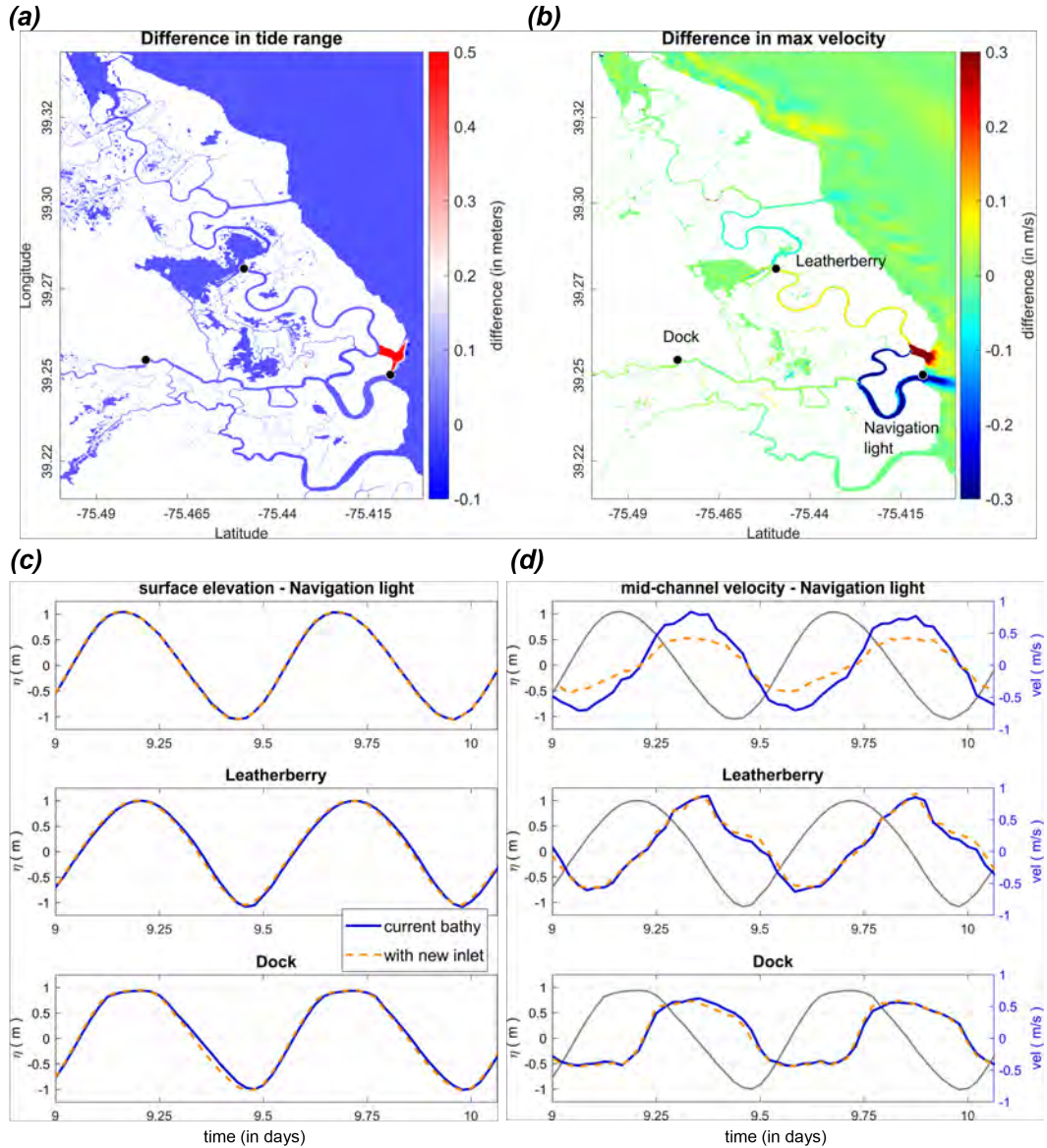
Figure 2.18: (a) Changes to the tide range from a new inlet opening (in meters). The tide range estimated from current bathymetry scenario is subtracted from the tide range of new inlet opening scenario; (b) Similar subtraction is done between current bathymetry and new inlet opening scenario for the maximum velocity magnitude (in m/s); (c) Model surface elevation for the two scenarios at interior tide gauge locations during a spring cycle (in meters, from NAVD88 vertical reference level); (d) Mid-channel velocity at the same gauges (in m/s). Surface elevation for current bathymetry scenario (referenced to NAVD88, in meters) is shown with the solid gray line to represent the flood and ebb tide.
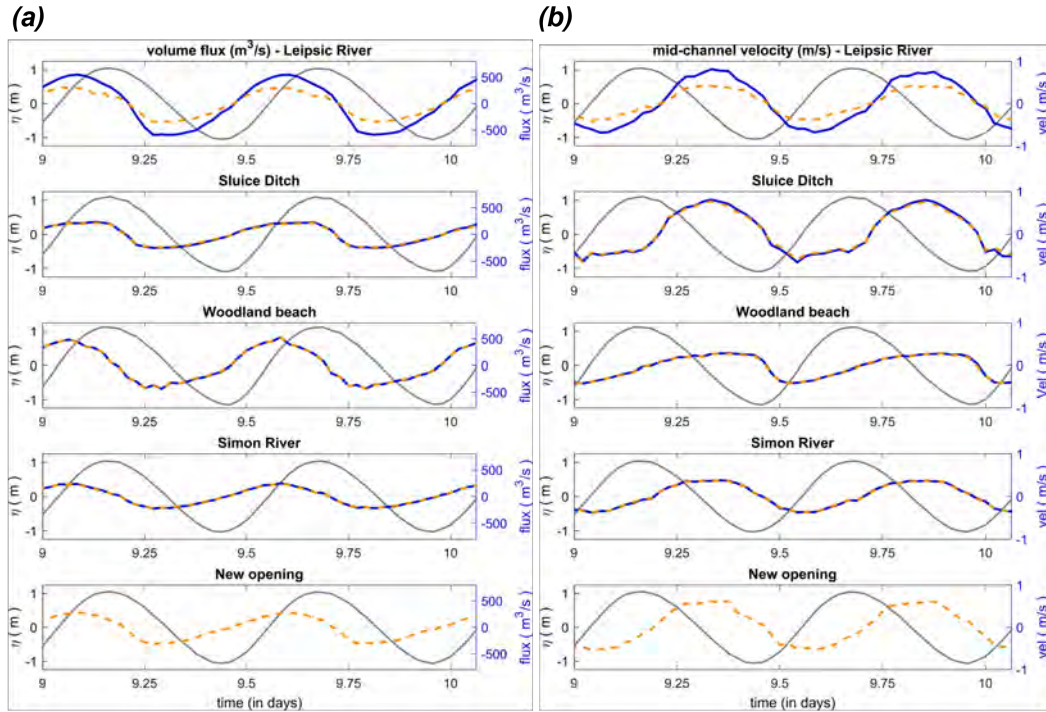
Figure 2.19: Changes in (a) volume flux (in m³/s) going in/out through BHNWR inlets and (b) mid-channel velocities for current bathymetry and a new inlet opening scenario during a spring cycle. The blue straight line represent flow condition based on current bathymetry and the orange dashed line is for the new inlet opening. Surface elevation from respective inlet entrance locations for current bathymery (referenced to NAVD88, in meters) is shown with the solid gray line to represent the ebb and flood conditions.

45

2.6   Concluding Remarks

To have a good assessment of the hydrodynamics in a complex environment like BHNWR, a high resolution unstructured grid model was required that represents complicated geometrical features of the wetland, and has a robust wetting/drying scheme. The FVCOM model was chosen for this study due to its well proven efficiency in resolving complex coastal geometry. Model validation is presented for the year 2015 and two storm conditions: Hurricane Sandy (2012) and Hurricane Joaquin (2015). A good agreement is observed between model and in-situ point source observations in terms of water surface elevation within Delaware Bay, main interior channels, tidal flats and over marsh platform. Moreover, the current velocity comparison in two major channels supported model reliability in predicting flood/ebb tide during calm conditions. The present state of tidal asymmetry based on channel velocity and inlet flux indicates that the system is strongly ebb dominant. Moreover, the morphology scenario analysis and simple mechanistic explanations provided an insight on the affect of man-made channel construction in altering overall wetland hydrodynamics, and how the system became more ebb dominant over time due to channel deepening. This paper is the first step toward looking into various physical processes which had possibly accelerated the erosive nature of BHNWR wetland. Also, it has provided a modeling platform to support wetland loss mitigation strategies to improve the long-term resilience of the system. As the BHNWR is one of the largest wetland system in the U.S. mid-Atlantic region, resolving the interaction between morphology changes and hydrodynamics have provided important insights which can be useful for restoration scenario analysis at other major multi-inlet wetland systems.

Chapter 3

HYDRODYNAMIC MODELING OF A COMPLEX SALT MARSH SYSTEM: IMPORTANCE OF CHANNEL SHORELINE AND BATHYMETRIC RESOLUTION

3.1 Introduction

The stability and long-term sediment transport in a tidal wetland system largely depend on the channel flow characteristics and morphology. Sediment transport directly correlates with the surface elevation/velocity asymmetry, that can be in the form of magnitude and period of the tidal wave (Friedrichs and Aubrey, 1988; Nidzieko, 2010; Ralston et al., 2012). Having an accurate estimate of tidal asymmetry and relative phase difference between current and surface are essential for determining residual flow, direction and sediment budget. In a channelized wetland system, tidal distortion (duration asymmetry and/or velocity skewness) varies when wave travels from inlet mouth to the boundary due to interaction between non-linear terms in the continuity and momentum equations (Parker, 1984; Aubrey and Speer, 1985; Friedrichs and Aubrey, 1988). More specifically, the space and time varying channel cross-section area, advective acceleration and quadratic friction play a major role in the generation of overtides and higher harmonics. In an estuarine system with negligible river discharge, besides asymmetry, the relative phase difference between tidal velocity u and surface elevation η can also vary both spatially and temporally due to system geometry, bottom friction and inter-tidal storage volume (Boon and Byrne, 1981; Friedrichs and Aubrey, 1988). The phase difference $\phi_{\eta u}$ between surface elevation and velocity has historically been used to characterize the tidal oscillations in an estuary as standing waves, progressive waves, or a combination of both (Parker, 1984; Jay, 1991; Friedrichs, 2010). When $\phi_{\eta u} = 90°$ it represents a standing wave, $\phi_{\eta u} = 0°$ represents

a progressive wave, and if the difference remains in between and close to 45°, then it is called a mixed wave type estuary. In a non-convergent short estuary with dominant semi-diurnal tide and barrier at the upstream end, $\phi_{\eta u}$ is a product of the interaction between incident and reflected waves (Hunt, 1964; Ippen, 1966; Officer, 1976). If the bottom friction is negligible, as in the case for a deep rectangular channel, it produces $\phi_{\eta u} = 90°$ and a standing wave type condition. For the same finite channel, wave properties can change in the presence of strong bottom friction, where the incident and reflected wave amplitudes decay and their phase lag follows the friction force (Hunt, 1964). Beside channel bottom friction, the channel hypsometry change based on the tidal surface elevation can also affect the amplitude decay and phase lag by enhancing or reducing the topographic dissipation (Li and Hodges, 2020). To properly identify the tidal wave characteristics and flow asymmetry inside a wetland system, we need a robust numerical modeling system that can resolve the variation in channel-marsh shoreline boundary and hypsometry with higher accuracy.

3.1.1 Background on modeling limitations in a marsh-channel system

3.1.1.1 Model grid resolution and the wetland flooding and draining

All of the studies mentioned above have evaluated dominant physical processes for $\phi_{\eta u}$ phase increase/decrease in channelized estuaries using simplified 1D wave or diffusion equations. These models have some common assumptions when dealing with the channel geometry, such as exponential channel width increase or decrease, depth is cross-section averaged, or the channel has a prismatic shape (Friedrichs, 2010). In a complex wetland system, to predict smaller scale processes, the along and across-channel bathymetry variations are key factors in determining time and space varying amplitude-velocity phase difference that a 1D model is not capable to resolve. To take care of the lateral and vertical channel variations, a 2D model is required with enough resolution to resolve the tidally varying hypsometry. However, developing an efficient high fidelity wetland/salt-marsh 2D model is a challenging task as it requires an understanding of the optimum grid resolution and more importantly availability of

high resolution data sets of marsh topography and channel bathymetry (e.g., LiDAR). Each of them has limitations such as spatially variable biases due to the presence of vegetation and temporal variations due to seasonal or severe events changes. Until now, a large number of studies have been done to address estuarine/coastal circulation problems using structured curvilinear (Lesser et al., 2004; Chen et al., 2014), unstructured/triangular (Luettich Jr et al., 1992; Chen et al., 2008) and hybrid grids (Bomers et al., 2019) in finite difference, finite element or finite volume discretization frameworks. In complex wetlands where bathymetry and/or topography gradient is large, an unstructured grid offers better performance in terms of shape flexibility and computational efficiency (Dietrich et al., 2012; Symonds et al., 2017). Inside a wetland system, the model performance then depends on changes to grid resolution following the variation of topo-bathy gradient, which can affect marsh-channel draining and filling. Moreover, most of the numerical models, 2D depth averaged or 3D, applied on a complex shallow environment, use a minimum depth value that controls the moving wet/dry boundary and corresponding inundation extent. In the inter-tidal zones like wetlands, it is essential to have a highly accurate land-water interface line for estimating the volume of water that goes back and forth between channel and marsh surfaces. In such systems, major channels and tidal creeks normally have an elevated side-bank/berm close to the interface that separates both channel and marsh platform, and subsequently influences model wetting/drying and flooding/draining speed. Furthermore, increase or decrease of the channel resolution changes the channel hypsometry which directly affects the flow continuity and momentum. For these reasons, it is mandatory to properly resolve the land-water flow exchange and channel hypsometry with optimum spatial grid resolution in order to have accurate estimation of tidal amplitude, phase speed and asymmetry inside a wetland system. An optimum grid resolution would also avoid model slow down due to the total number of elements and CFL constraints, governed by the minimum grid size.

3.1.1.2   Channel bathymetry data

Although a grid with enough resolution for resolving all the major processes is an important need, the model performance can be constrained by the scarcity of unbiased marsh topography and channel bathymetry data (Yu and Lane, 2006; Horritt et al., 2006). Recently, the emergence of different remote sensing techniques such as Light Detection and Ranging (LiDAR; e.g., Horritt et al. (2006)) and Interferometric Synthetic Aperture Radar (SAR; e.g., Horritt and Bates (2001)) have significantly improved the overland flood modeling, where the spatial resolution can reach up to 1 m with a vertical accuracy of ± 15 cm on bare ground(Yu and Lane, 2006). However, these data sets have some major drawbacks that includes inability to map the channel bathymetry, only limited to dry areas and can have vegetation bias based on the data acquisition period (tidal stage and seasonality). While the vegetation bias in the LiDAR data can be treated via a number of techniques such as minimum bin technique (Schmid et al., 2011)), the proper representation of channel bathymetry is still a challenging task. To make seamless topo-bathymetric DEMs in wetlands, that include shallow turbid water bodies, the most popular and reliable technique is the use of an acoustic sonar system that can map the seafloor from single or multi-beam echo sounding (Dierssen and Theberge, 2014). Inside a coastal wetland system that has major channels and tidal mudflats, it is imperative to collect high density bathymetry data to properly represent the channel hypsometry in model calculations.

3.1.2   Present study

This study assesses the role of grid resolution and accuracy of topobathymetric data on the tidal wave propagation and velocity asymmetry, to determine the role of inaccurate representation of the major channels hypsometry in reducing model reliability inside the wetland. The case study is Bombay Hook National Wildlife Refuge (BHNWR), DE located on the western shore of Delaware Bay, which as one of the largest multi-inlet tidal wetland system in the mid-Atlantic region, is rapidly eroding salt marsh system with short length, non-convergent and deep channels (Figure 3.1a).

The system has two major inlets, namely Sluice Ditch and Leipsic River, that are responsible for two-thirds of the total volume transport (Deb et al., 2020b). Other important information about the study areas geographic coverage, economic significance and ongoing wetland loss is detailed in Deb et al. (2020b). In this study, the 2D model performance is described after implementing a sufficient grid resolution that resolves marsh-channel interface properly and a dense channel survey data, which in fact provides a more realistic estimate of the tidal regime and velocity asymmetry.

This chapter is organized as follows. Sections 3.2.1.1 and 3.2.1.2 describes unstructured grid development, the pre-exisiting grid-A from a previous study and new ones (B,C) using bias corrected high-resolution LiDAR data set with surveyed marsh elevation for topography and channel data for bathymetry. Section 3.2.2 provides a brief overview of the FVCOM model physics and closures for the depth-integrated 2D version. Model results for stormy conditions are given in Section 3.3, illustrating model inconsistency that emerges from changes to the grid resolution and topo-bathymetry. A detailed description of the significant modeling bias from inaccurate channel hypsometry, and how a proper channel survey data can improve overall tidal hydrodynamics and model accuracy are given in section 3.4. Concluding remarks and observations on the necessity of the future works are discussed in section 3.5.
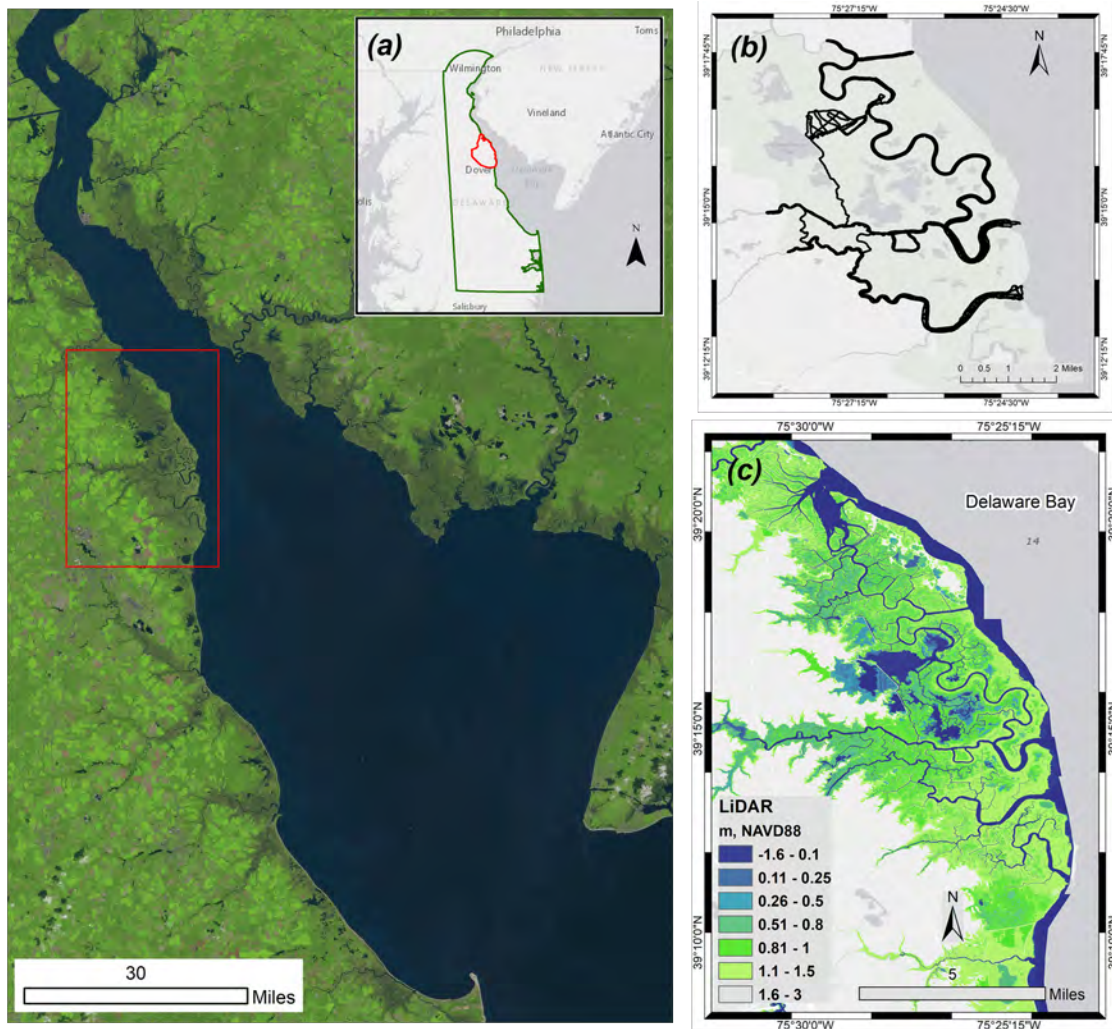
Figure 3.1: (a) Top: The state of Delaware, U.S., Bottom: USGS Landsat imagery for the Delaware Bay (https://glovis.usgs.gov/), the red polygons show the study area, Bombay Hook National Wildlife Refuge, DE (b) channel survey track lines inside the wetland (c) NOAA 2011 LiDAR data set of marsh surface (in meters, vertical datum: NAVD88)
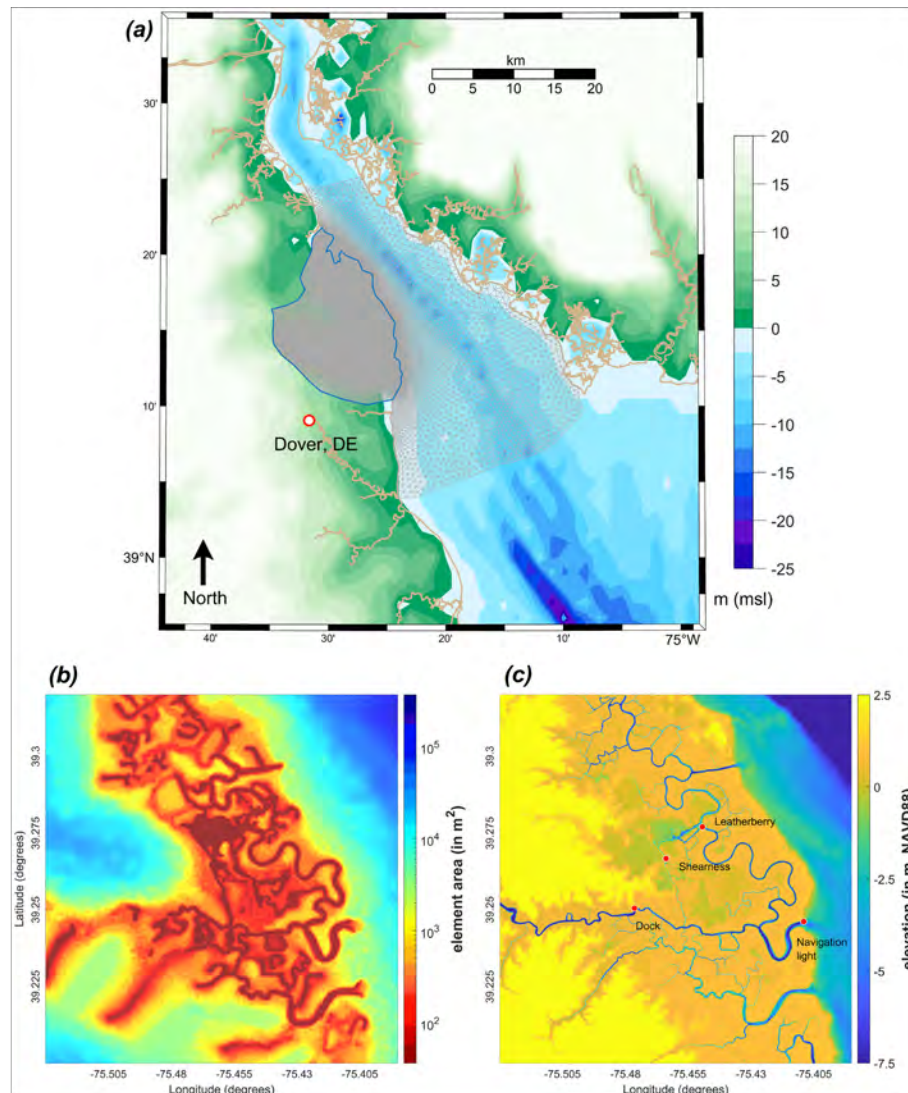
Figure 3.2: (a) FVCOM model grid domain in the Delaware Bay. Golden line represents the shoreline and blue polygon is the wetland extent that has higher resolution. The topo-bathymetric basemap below is from NOAA-NCEI global ETOPO2 grid (in meters, MSL) (b) variation of unstructured grid size: smaller elements inside the wetland and gradually larger outside (in sq. meters) (c) topo-bathymetry of the wetland from seamless DEM using LiDAR and channel survey data sets (in meters, NAVD88). Red points show tide gauge locations used for model validation.

53

3.2 Methods

3.2.1 Model grid development

In this section, we describe the development of different DEMs, and how they have been used for computational grid generation and terrain representation.

3.2.1.1 Topo-bathymetric DEM

For the study area BHNWR, three high resolution LiDAR data sets of the years 2007, 2011 and 2014 are collected from different sources (Deb et al., 2018a), processed to a regular grid with 1 m resolution and referenced to the NAVD88 datum. These data sets are compared with the ground truth survey at different locations to identify the most reliable one with minimum vegetation bias. Metadata, accuracy and extent of these data sets are described in Deb et al. (2018a). The National Oceanic and Atmospheric Administration (NOAA) 2011 data set has the least bias compared to other data sets and therefore was used for the high-resolution model development of BHNWR (Figure 3.1c). In this study, two sets of 2011 LiDAR data are used, where one represents actual NOAA post-processed data that contains vegetation bias; previously used in a similar hydrodynamic study by Stammerman (2013), and a modified one that has been corrected using ground truth, field vegetation survey and vegetation maps.

For the bathymetry, NOAA-NGDC data sets were collected for the bay side of the domain, developed from depth soundings for the Delaware Bay and Estuary (Stammerman, 2013). The NOAA-NGDC data does not have a good representation of the channels inside BHNWR system and required a separate field survey of the major channels and tidal creeks. In a previous study of the same area, Stammerman (2013) measured a total of 48 cross sectional profiles on the major channels and 5 on the mudflats using hand-held sonar, and used linear interpolation of the bathymetry along channels in between the cross sections. The surveyed data points were referenced vertically to NAVD88 datum and interpolated to model NOAA-NGDC DEM for final model bathymetry of the area. For a large wetland like BHNWR, this channel survey data is not sufficient to properly represent along-channel cross sectional geometries.

54

For the present study, a bathymetric survey of the main waterways in BHNWR was conducted using single-beam echosounder to obtain continuous depth with much higher density (McDowell, 2017). The survey consists measurement of depth and horizontal coordinates along cross sections, middle and sides of the channel profile and multiple zig-zag patterns (Figure 3.1b). The raw bathymetric soundings were processed, detided using nearest tide gauges, evaluated for outliers and then referenced to horizontal and vertical datums: Universal Transverse Mercator (UTM) Zone 18 and NAVD88 respectively. Additional information on the survey and pre/post processing of the data set is given in Deb et al. (2018b). The new channel bathymetry information then interpolated back to the previously developed data set of Stammerman (2013), and channel representation from both low and higher density survey data sets are shown in Figure 3.3 & 3.4.

Finally, from the collected and surveyed marsh topography and channel bathymetry data sets, we made two different seamless topo-bathymetric DEMs for this study using: 1) NOAA 2011 LiDAR data set and sparse channel survey done by Stammerman (2013), and 2) Bias corrected NOAA 2011 LiDAR and new dense channel survey data of the entire BHNWR.

3.2.1.2   Unstructured grid

Two unstructured grids of varying element sizes are generated, with identical nodes coordinates inside the bay and different resolutions inside the wetland system to describe how a small change in grid resolution can significantly affect the overall tidal regime, and provide an ambiguous modeling solution.

An unstructured grid covering the entire wetland with sufficient resolution for resolving tidal processes, was available from a previous hydrodynamic study of BHNWR (Stammerman, 2013). The model grid domain, shown in Figure 3.2a, covers interior Delaware Bay from Bowers, Delaware on southern boundary up to 39° 25′ N latitude on Delaware River, and has a total of 370629 nodes and 740776 elements. Stammerman (2013)) used a mesh generation tool JANET (http://www.smileconsult.de/

`index.php`) that applies forcing polygons or break lines to enforce the alignment of elements along the marsh-channel shoreline. The nodes on the forcing polygon were distributed manually based on the desired distance in specific areas, and the basic triangulation connected these nodes. The nodes on the tidal channels were pre-defined, and the mesh resolution transitioned from small elements in channels to bigger elements over the marsh surfaces, neglecting the steep channel side walls and berms (Figure 3.3a.1). In a tidally varying environment, the unresolved channel berms can change the land-water interface and channel width dramatically, causing artificial channel convergence/divergence following low/high tide. To tackle this problem, the resolution of the existing grid of (Stammerman, 2013) was increased, mostly in the major channels, tidal creeks and land-water interface covering elevated berms (Figure 3.3b.1). The zero NAVD88 elevation contour is used to define the channel lateral boundaries, and the bathymetry gradient is then used to increase the resolution in channel areas with higher gradients. As a result, the interior channels, berms and channel shorelines have higher resolution compared to the marsh platform. The new grid has an element size as fine as $\sim$ 3 m around marsh-channel boundaries, and in total has 488207 nodes and 975931 elements (Figure 3.2b, 3.3b.1).

Ultimately, using these two different resolutions and two channel bathymetry data sets, three unstructured grids are used for the analysis (Figure 3.3). They are unique in representing channel hypsometry based on the tidal elevation, where the main properties are:

1. Grid-A: lower channel resolution and insufficient channel survey, collected from Stammerman (2013) (Figure 3.3a)

2. Grid-B: higher channel and berm resolution, and bathymetry from Stammerman (2013) (Figure 3.3b)

3. Grid-C: higher channel and berm resolution, new dense channel survey data set (Figure 3.3c).

The dramatic difference between sparse and dense bathymetric survey data set is shown in Figure 3.4a,b. In Figure 3.4b, we can see that there is a significant difference between cross section averaged depths estimated from different grids along the Leipsic River, which could bring errors to the overall model performance and tidal hydrodynamics.

3.2.2   Modeling background and boundary forcings

For this study, we use the Finite-Volume, primitive equation Community Ocean Model (FVCOM) developed by Chen et al. (2008), which is an unstructured grid model and widely used for resolving coastal scale processes both in 2D and 3D. The 2D model is driven with two different sets of boundary conditions: 1) Water level and depth average velocity fields from the large scale three-dimensional model of Delaware Bay: Regional Ocean Modeling System (ROMS) (Kukulka et al., 2017) directly nested at the unstructured grid open boundary nodes for stormy conditions and 2) local M_2 tidal amplitude and period at open boundaries to reproduce a calm condition without channel berm overtopping. While the first set of simulations will show the role of grid resolution and quality of topo-bathymetric data in model under/over-prediction and phase lag during Hurricane Sandy and Hurricane Joaquin, the second set will explain qualitatively how a significant portion of the phase lag can be generated solely from the inaccurate channel hypsometry, and influence the overall tidal regime and velocity asymmetry.

Both meteorological events Hurricane Sandy (2012) and Hurricane Joaquin (2015) used for model vs. in-situ comparison had threatened the Delaware Bay with storm surge and large-scale coastal flooding (Dohner et al., 2016). Hurricane Sandy made landfall on the New Jersey coast near Brigantine, NJ (Sullivan and Uccellini, 2013), and Hurricane Joaquin initially made landfall in the Bahamas and then changed track, finally moving north-northeastward over the Atlantic Ocean. Hurricane Joaquin stayed away from the US mainland and close to the shelf; however, significantly affected the the DE and Chesapeake bay area because of its gradually amplified surge

generated for a longer period compared to Hurricane Sandy. ROMS large scale simulations for the entire Bay included the necessary forcings such as atmospheric forcing, tidal constituents and river discharge data from multiple sources, and were validated against NOAA tide gauges located in the Bay (Deb et al., 2020b). Then, after nesting ROMS data at the FVCOM boundary, four tide gauge data sets, located on wetland interior channels (Figure 3.2c) are used to evaluate the model performance for different prescribed grid conditions. The tide gauges have information from the year 2008 to 2019 and regularly maintained by the Delaware Department of Natural Resources and Environmental Control (DNREC). After collection, all data sets were post-processed and converted to water surface elevation referenced to the NAVD88 datum. Among the channel tide gauges, "Navigation light" is located on the major channel/inlet mouth, "Dock" is close to the model upstream boundary, and two other gauges "Leatherberry" and "Shearness" are from inside the wetland & near a tidal mudflat, as shown in Figure 3.2c. For this study, a small portion of the entire channel tide gauge data are taken for model comparison that represents the major storm events: Hurricane Sandy and Hurricane Joaquin.

More information about 2D model code, methods for prescribing tidal and subtidal boundary condition, validation and its limitations are given in Deb et al. (2020b). For the second part of the study, to simulate channel flooding and draining without marsh overtopping, the principal lunar semi-diurnal constituent M_2 amplitude and period are extracted from the nearest Bay tide gauge Ship John Shoal, NJ (https://tidesandcurrents.noaa.gov/) using T_TIDE, a tidal harmonic analysis tool (Pawlowicz et al., 2002). For different model runs, all the physical parameters such as drag coefficient, mixing coefficient and others are kept the same as cases in Deb et al. (2020b).
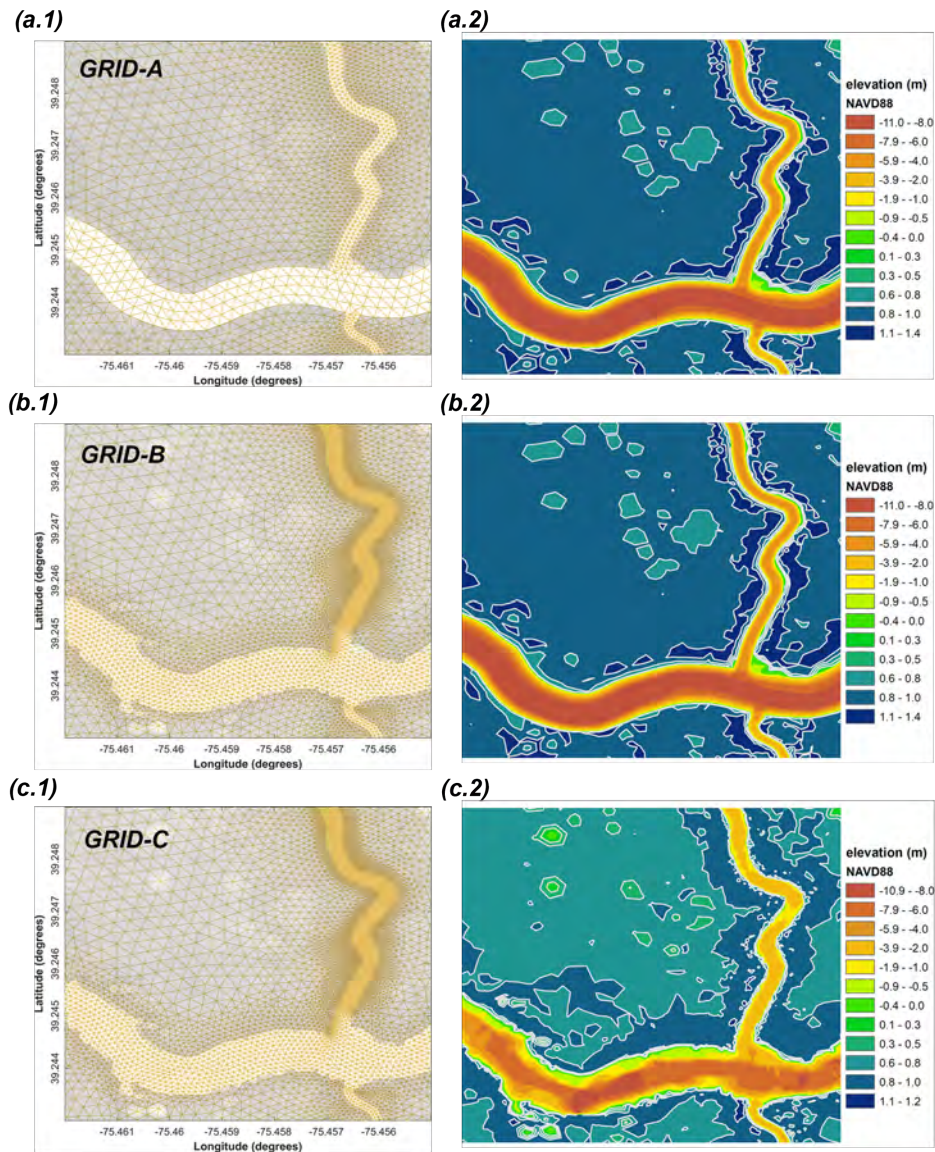
Figure 3.3: Unstructured grids with different marsh-channel hypsometry, separated into two columns showing resolution (left) and topo-bathymetry in meters, NAVD88 (right): (a) low resolution in channels, insufficient channel survey and biased LiDAR data (b) high resolution in channels and on berms, topo-bathymetry interpolated from biased Lidar and sparse bathymetric survey (c) high resolution in channels and on berms, new dense channel survey data set and vegetation bias corrected LiDAR elevation.
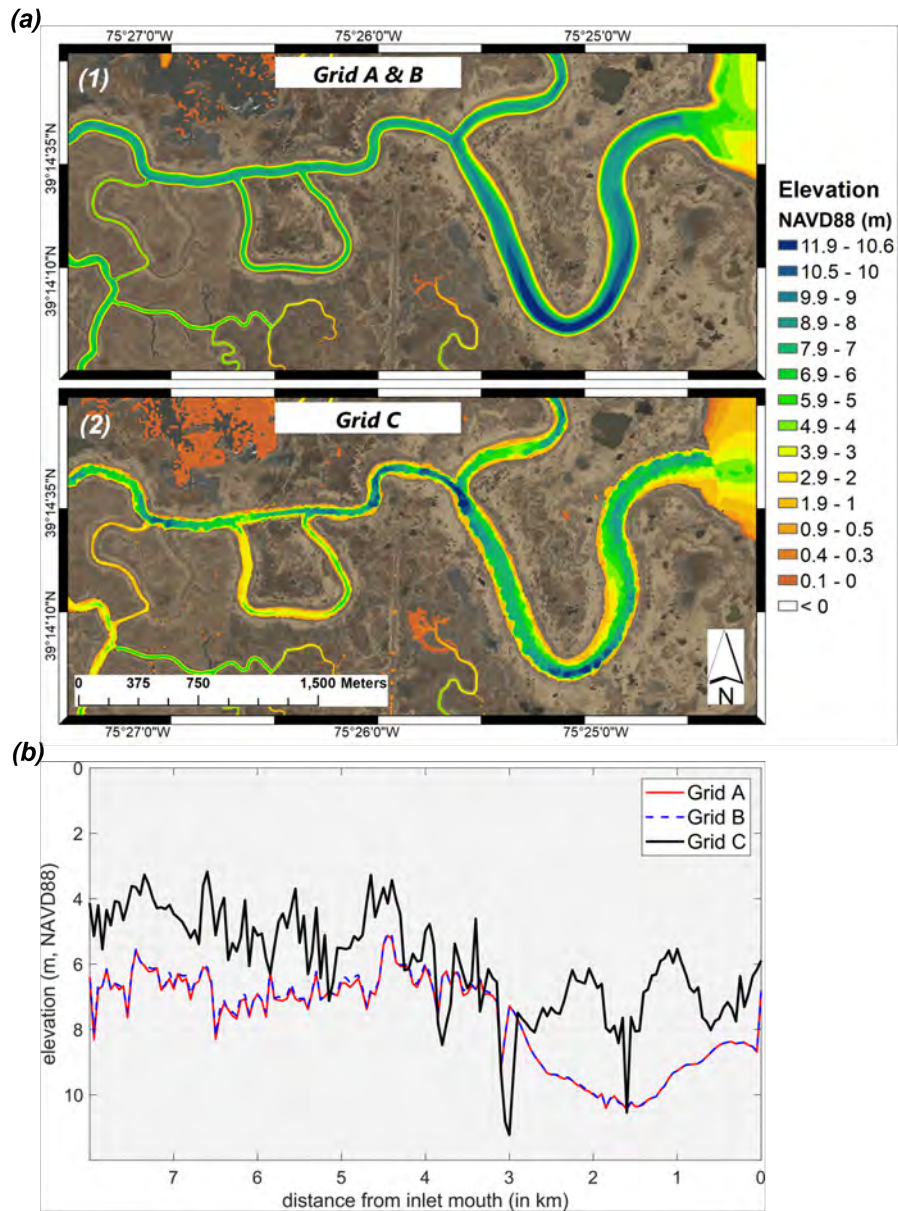
Figure 3.4: Bathymetry in a major channel: Leipsic River from different survey data sets interpolated to the model grids. Grid properties are described in Figure 3.3, Grid A & B have different resolutions; but same source of bathymetry. (a) spatial variation of channel elevation from NAVD88 datum (in meters) (b) cross-section averaged bathymetry from inlet mouth to boundary (in meters)

3.3 Results

In this section, water surface elevations from model and in-situ data during the storm events are compared (Figure 3.5-3.6 and 3.7-3.8) to understand the role of proper channel resolution and hypsometry on accurate wetland flood modeling. The comparisons have been assessed in terms of model skill (Willmott, 1981) and average bias index (Equation 2.3.1-2.3.2), where a model skill of 1.0 shows perfect agreement and a positive/negative bias represents model over/under-prediction respectively.

Here, more emphasis is given to the cases with Hurricane Joaquin (2015) where more field deployments, including current profiler data, are available. Figures 3.5-3.6 and 3.7-3.8 shows surface elevation comparison and statistics at channel tide gauges during Hurricane Joaquin and Hurricane Sandy, and both Figure 3.5 and Figure 3.7 are separated into two sub-figures: (a) showing the difference before the arrival of main surge and (b) during major event when the entire wetland system was submerged. Main comparison drawn here is between the in-situ and model results from three different grid configurations (A, B & C), described in the previous section. The differences between model results from Grids A - B and Grids B - C are due to grid resolution and accuracy of topo-bathymetric data sets respectively.
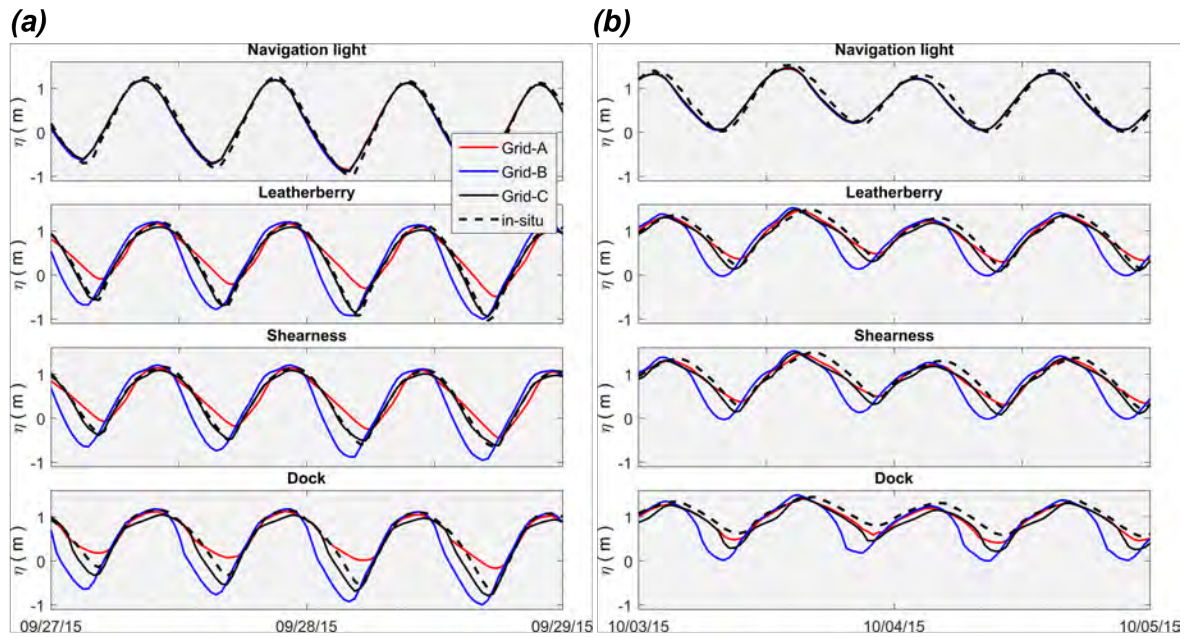
Figure 3.5: Water surface elevation from FVCOM model grids (straight lines) and in-situ (dashed line) during Hurricane Joaquin, 2015 at different channel tide gauge locations (in meters, from NAVD88 vertical reference level) (a) before the main surge event (b) during surge event.
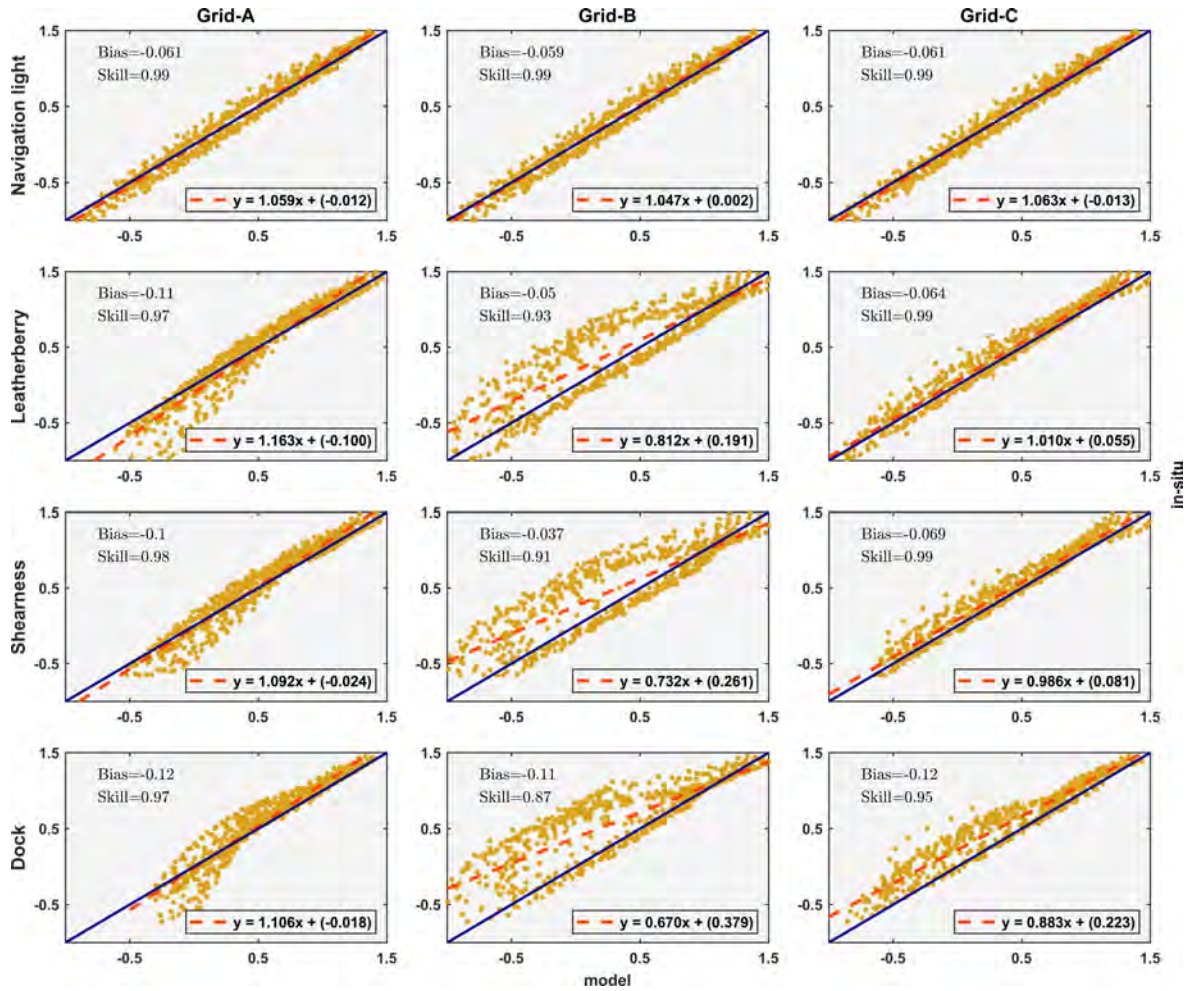
Figure 3.6: Scatter comparison: average bias index and skill between FVCOM model grids (separated into 3 columns) and in-situ water surface elevation at different channel tide gauge locations during the entire model period of Hurricane Joaquin, 2015 (in meters, from NAVD88 vertical reference level).
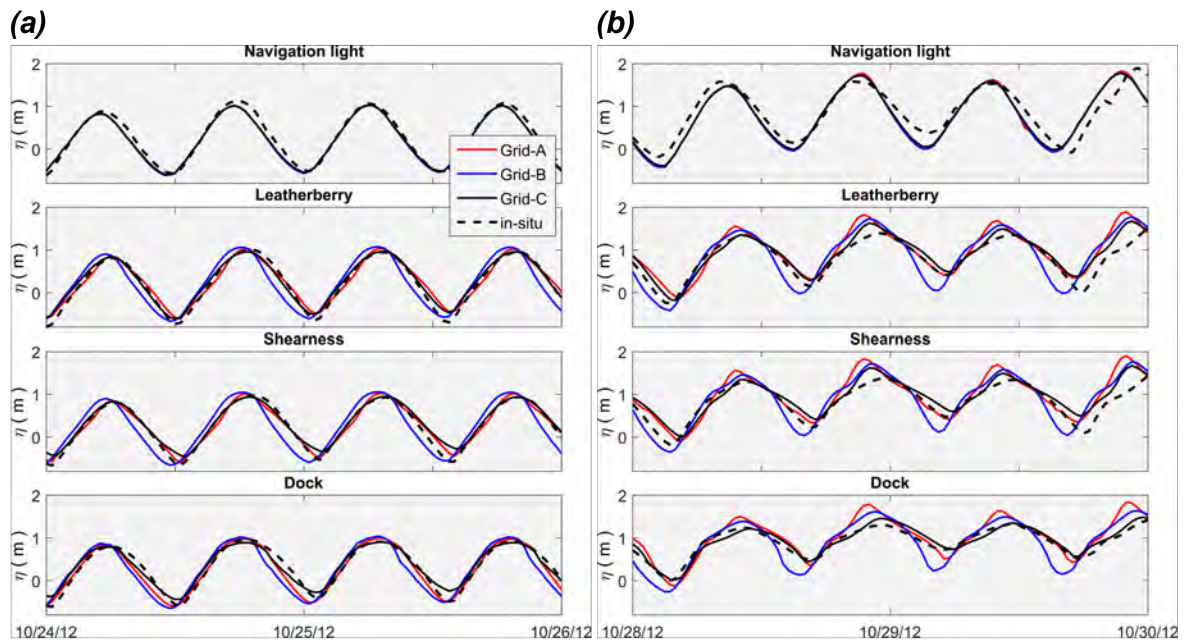
Figure 3.7: Water surface elevation from FVCOM model grids (straight lines) and in-situ (dashed line) during Hurricane Sandy, 2012 at different channel tide gauge locations (in meters, from NAVD88 vertical reference level) (a) before the main surge event (b) during surge event.

64
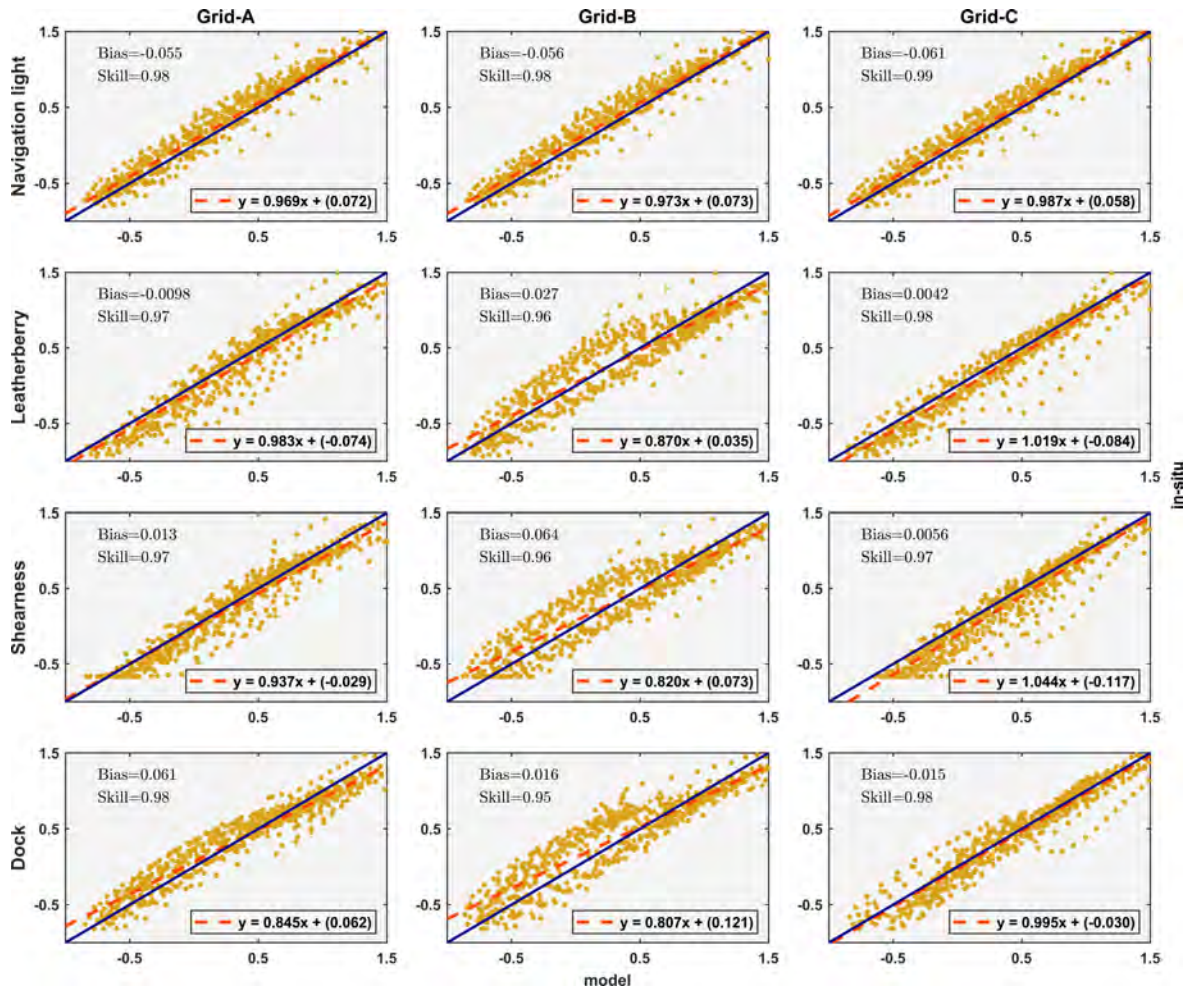
Figure 3.8: Scatter comparison: average bias index and skill between FVCOM model grids (separated into 3 columns) and in-situ water surface elevation at different channel tide gauge locations during Hurricane Sandy, 2012 (in meters, from NAVD88 vertical reference level)

We first examine the Grid-A case, which has lower resolution in the channels and sparse bathymetry data. For Hurricane Joaquin (Figures 3.5-3.6), model skill is relatively better close to the inlet opening (Navigation light) than the interior gauges (i.e. Dock). Overall, model skill remains close to 0.97, which indicates that Grid-A is a reliable option for further model analysis. However, before the entire marsh submergence during Hurricane Joaquin, there is a higher bias that originated from model under-prediction of surface elevation during low tide and the reduced tidal range along the channel as tide propagates inward from Navigation light to Dock (Figure 3.5). Then, when the major surge event inundates the marsh platform (Figure 3.5b), a better reproduction of channel flooding and draining is observed and subsequently higher skill at all the gauges is achieved. These differences actually display the role of marsh surface flooding and draining in overall model performance, where before the major surge we have an active model wet/dry domain, in contrast to the entirely wet domain with the residual surge. Interestingly, the same grid shows a better skill during calm conditions before Hurricane Sandy residual surge, and channel draining also seems to be accurate compared to the case of Hurricane Joaquin (Figures 3.7 and 3.8).

Grid-B has an increased resolution in order to better resolve the land-water interface during tidal fluctuations; however, the channel bathymetry is interpolated from the DEM used to construct Grid-A. For the case of Grid-B, a drastic change in the scatter comparison is observed for both storm conditions, much more pronounced during Hurricane Joaquin. The model skill deteriorated faster inside the wetland upstream gauges (Figure 3.6, middle column) and the trend is significantly different from Grid-A. To understand this reduction in model skill with improved Grid-B resolution, time series plot during calm condition is shown in Figure 3.5, when the system still has active wetting/drying. It shows improvements in channel draining and tidal range prediction during low tide condition. The previous trend of under-prediction at the interior channel gauges has now changed to over-prediction with a significant increase in phase mismatches. These low tide over-prediction and sharper drops to the trough compared to in-situ ultimately deteriorated the model skill. The phase lag remains

during elevated MWL when wet part of the domain expands (Figure 3.5b), slightly less pronounced during Hurricane Sandy (Figure 3.7-3.8). This case with Grid-B raises a new concern that with an improved marsh-channel resolution, why the system now shows a higher phase lag during ebb and if it is solely from the inaccurate surveyed channel hypsometry. A detailed explanation of the tidal phase speed discrepancy due to inaccurate channel bathymetry is given in the discussion section.

For the case of Grid-C, with Grid-B resolution and more accurate topo-bathymetry, an immediate improvement in wave phase prediction, tidal range and channel draining/flooding are observed (Figure 3.6b, last column). Scatter comparison in Figure 3.5 show that the model skill and slope are close to 1.0 during the full period of Hurricane Joaquin, and also a similar response during Hurricane Sandy (Figure 3.7 and 3.8). Note that slightly inaccurate sub-tidal forcing at the boundary, originally came from the large scale model, has led to inaccurate sub-tidal signals in the entire domain, including the bay side gauges (Deb et al., 2018a). Finally, results using Grid-C show the importance of along and across channel bathymetry in resolving the hydrodynamics and tidal processes with higher accuracy.

3.4 Discussion

In the results section, we have shown surface elevation comparison at different channel locations inside BHNWR wetland system during Hurricane Joaquin and Sandy for different grids, and how the model responds to the changes in channel hypsometry (Figures 3.5-3.6, 3.7-3.8). We can see that the agreement between model and in-situ elevation varies based on different grid configurations. Our study area can be considered as a short estuary system, where the wetland basin length is close to 20 km and it is much shorter than the tidal wavelength 400 km for a semi-diurnal tidal period of 12.42 hours (Parker, 1984). Channels are mostly narrow ($\sim$200 m), weakly-converging and deep at the middle ($\sim$10 m); however, the cross-sectional area varies significantly over the entire reach due to shallow/deep side banks. In-situ tide gauge data sets have shown that the tidal amplitude decay rate is insignificant, while there is a noticeable lag in phase when wave travels upstream. In results section we have observed that the model performs well at gauge location close to the open bay (Navigation light) for all grids and storm events. However, when we looked into the marsh interior, in all our remaining gauge locations model predicts surface better during raising tide compared to the falling.

3.4.1 Role of marsh-channel connectivity and artificial ponding on model performance

Mainly, in Grid-A which has a lower resolution in channels, we can see that it under-predicts surface elevation during low tide, but then Grid-B with higher resolution over-predicts surface and misses phase completely (Figure 3.5-3.6, 3.7-3.8). Subsequently, model prediction improves immediately during both high and low tide when surveyed channel bathymetry interpolated into Grid-B, represented as Grid-C. In Grid-A with previously collected bathymetry and lower resolution, model suffers from inefficient marsh interior channel connectivity, along with a process called artificial ponding over the marsh platform (a modeling limitation from LiDAR and model grid resolution), ultimately leading to inaccurate drainage during low tide. Artificial

ponding comes from the unresolved small marsh channels/creeks in model grid that in reality drains the isolated low spots in DEM depressions formed by channel berms. A detailed description of the ponding problem and the ongoing work has been provided in Deb et al. (2018a). For the scope of this paper, importance of artifical ponding is less significant compared to the grid resolution in marsh-channel berm locations and the need of proper channel survey data.

During Hurricane Joaquin, the volume of water stored over marsh surface was significant due to a longer surge period. The land-water interface along the channels were not resolved properly in the low resolution grid and it took longer time to properly drain the stored water, as most of the wetland area remain active and wet. As a result, the ebb duration increased and the raising tide caught falling tide before reaching it's lowest limit in the channels. With improved resolution and properly defined channel berms in Grid-B, we observed an immediate improvement in the internal channel drainage pattern. The well resolved channel berms have helped to separate channels from marsh surfaces when water level dropped below model minimum depth (5 cm). Now, the surface elevation reaches close to in-situ elevation during low tide in the channels; however, it drains water faster than previous causing a phase lag between model and in-situ. An increase in resolution, while keeping old bathymetry in place have actually raised the channel volume flux and shifted it toward a frictionless estuary, explained further in the following section. Then, with new survey data in Grid-C, we found that the middle and cross-section averaged channel bottom is much rougher compared to previous conditions (Figure 3.4) and it improves the representation of shallower zones close to channel banks. This has changed spatially varying friction and helped to predict the phase better, shown in Figure 3.5-3.6. The response is almost similar for Hurricane Sandy except Grid-A with old bathymetry (Figure 3.7-3.8). In this case, interestingly, the model surface elevation matches better with in-situ during both high and low tide. To explain this we have to go back again to the channel connectivity issue mentioned before. For Hurricane Sandy there was no surge from the open ocean for couple of days prior to the landfall like Joaquin, and the marsh

overland flooding became significant only during the period of storm. So, there was no accumulated affect from marsh wetting/drying on channel draining and filling.

3.4.2 Channel hypsometry and surface phase lag

From Figure 3.7.a we can see that, Grid-B has surface elevation phase lag at wetland interior gauges (Leipsic, Shearness & Dock), even when there was no subtidal elevation and ponding right before Hurricane Sandy. While, Grid-A that is developed with low resolution channel representation, shows a good surface elevation agreement with in-situ at the same interior gauges. In this section, we explain this phase lag without any artificial storage over marshes, and also describe how an inaccurate representation of channel configuration from collected data or model grid resolution can provide ambiguous results, that is in good agreement with the in-situ data. We ran new cases with only a regular M_2 tide that has an amplitude of 0.8 m and a period of 12.42 hr keeping the grid properties unchanged. Now, the responses shown in Figure are completely from the channel properties (e.g. width, depth and friction). In, Figure 3.9 we have surface elevation comparison between at the two tide gauge locations along the main tidal channel Leipsic River: Navigation light (at the inlet mouth) and Dock (close to the boundary, 9 km upstream).

First we have compared model surface elevation for Grid-A and observe that there is a clear phase lag between the gauges during both rising and falling conditions (Figure 3.9). When improved the resolution in channels and marsh surface for Grid-B, phase lag goes away and and the solution represents a standing wave condition. Ultimately, with the surveyed channel bathymetry in Grid-C, we see a reestablishment of the phase lag between downstream and upstream gauges, but much more pronounced during falling tide. The low resolution grid elements in Grid-A that represents channel-marsh boundary causes connectivity issue during low tide due to minimum depth criteria defined for wetting/drying. As surface drops below minimum depth, nodes that are located over marsh edge makes the entire element fall into dry category, ultimately making the channel width narrow than the real configuration shown in Figure 3.10a

70
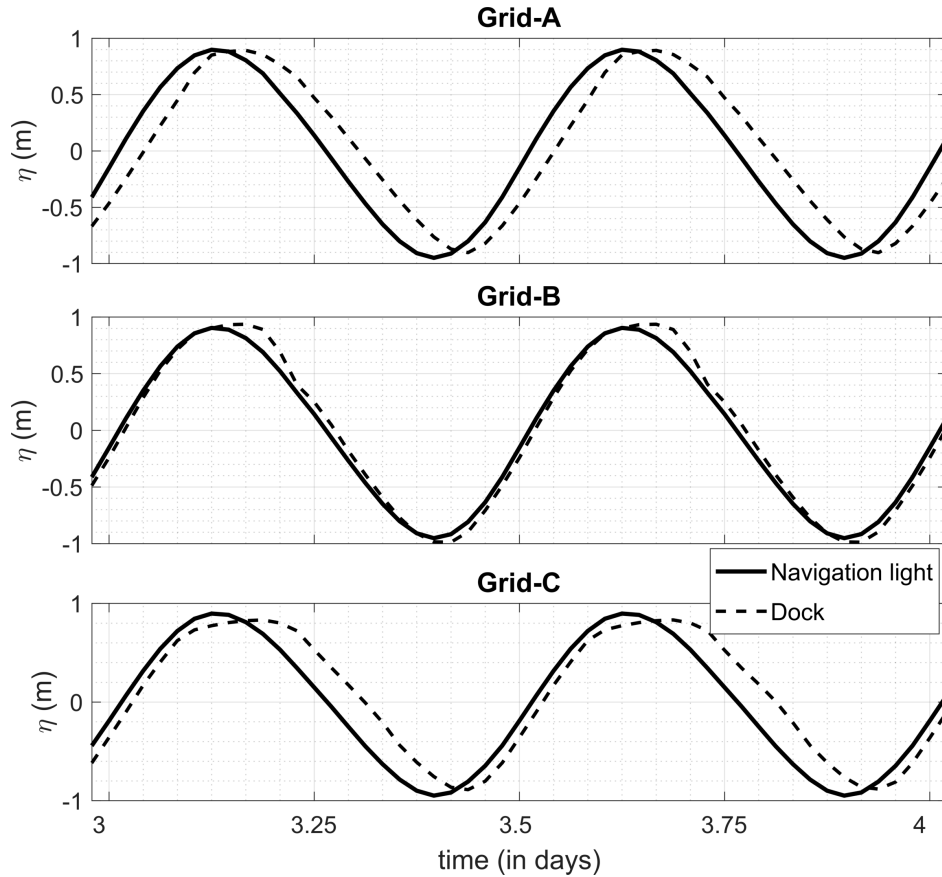
Figure 3.9: Model water surface elevation comparison between two gauge locations from inlet channel opening and boundary: Navigation light and Dock respectively (in meters, from NAVD88 vertical reference level). Subplots from the top to bottom shows a sequence of result for different grid conditions, A-C.

and 3.11a. Figure 3.11a (mid-column) shows a transect taken from mid-reach of the Leipsic River, where we can see that the width of the momentum transporting channel becomes almost half for most of the tidal cycle that slows down the wave propagation during both flood and ebb. With the higher resolution in channels and berm location we overcame the abrupt channel width contraction and expansion issue in Grid-B. Although, it changed the channel hypsometry from previous, but the interpolated bathymetry still remains inaccurate (Figure 3.4). From Figure 3.10b and 3.11b we can see a much smooth transition between marsh and channel during high and low

71

tides. In all of our previous surface elevation comparisons between model and in-situ shown in the results section, we have the highest bias for Grid-B compared to the other grids. In Figure 3.9 (second subplot) we can see that there are no changes in surface elevation phase, $\phi_{\eta\eta}$ for the entire channel reach and wave phase speed is a constant $(c = \sqrt{gh})$ at both flood and ebb, mimicking a frictionless, non-convergent estuary with a barrier at the head (Van Rijn et al., 2010). Ultimately, using Grid-C with surveyed bathymetry and a proper representation of the channel geometry, we noticed an increase in surface elevation phase lag again at both inlet mouth and boundary, much more pronounced during ebb condition (Figure 3.9 (bottom subplot)). From Figure 3.10c and 3.11c we can see that the width become almost similar to Grid-B during a high tide, while the well defined shoals close to channel banks reduced cross-section averaged depth significantly. Lateral channel depth varies throughout the entire reach, and represents a channel geometry that has a deep channel at the middle and shallow side banks. In, Figure 3.9 (bottom subplot), we can see that as tide travels upstream, phase propagates faster corresponding to the narrower and deeper channel section at the mid-channel and slows down during ebb due to the reduced depth.
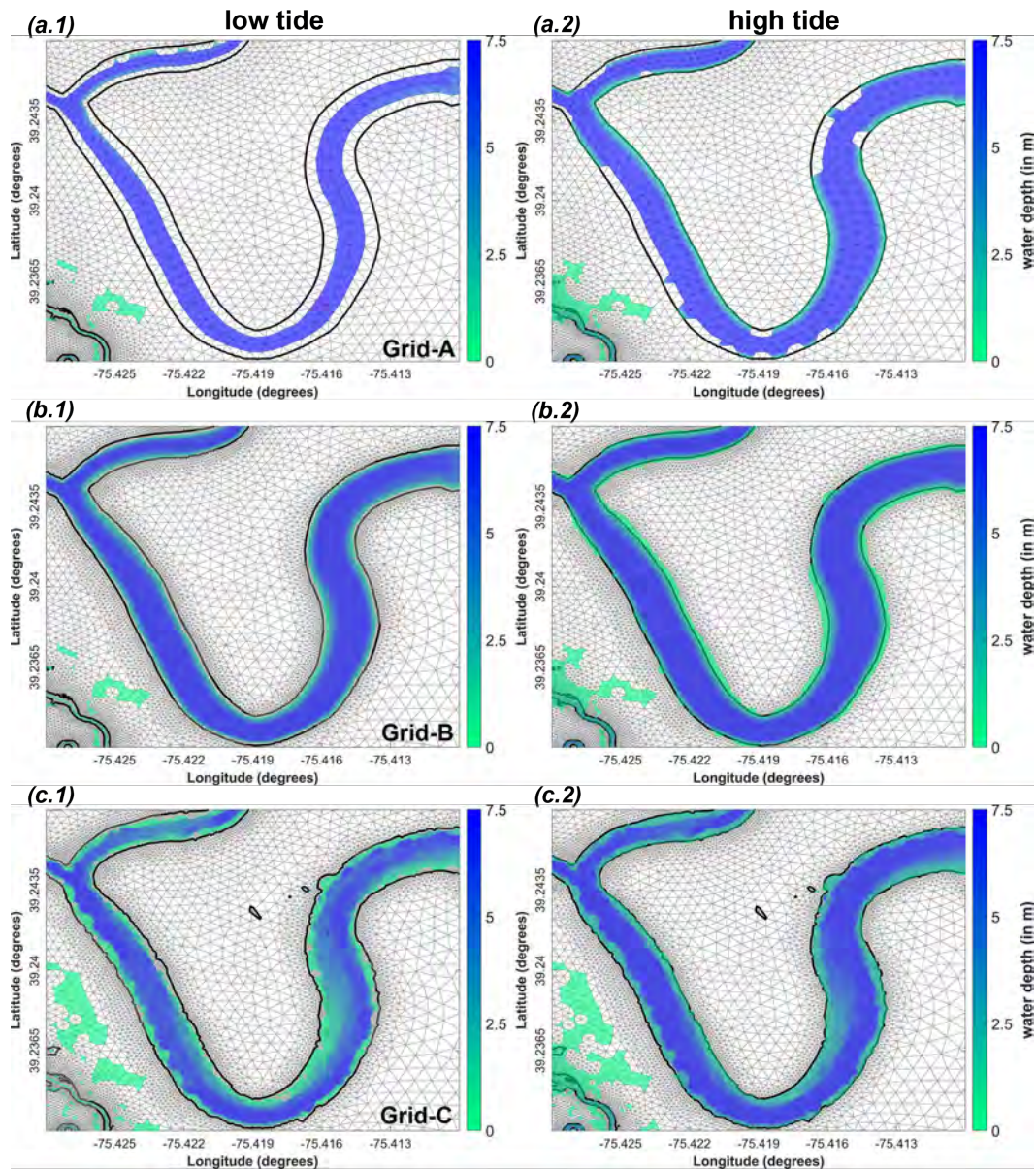
Figure 3.10: Channel total water depth (surface + bottom elevation, in meters) and width variation during low and high tide, separated into three rows for different grids: (a) lower channel resolution and insufficient channel survey (b) higher channel and berm resolution and bathymetry interpolated from the previous grid (c) higher channel and berm resolution and new dense channel survey data set.
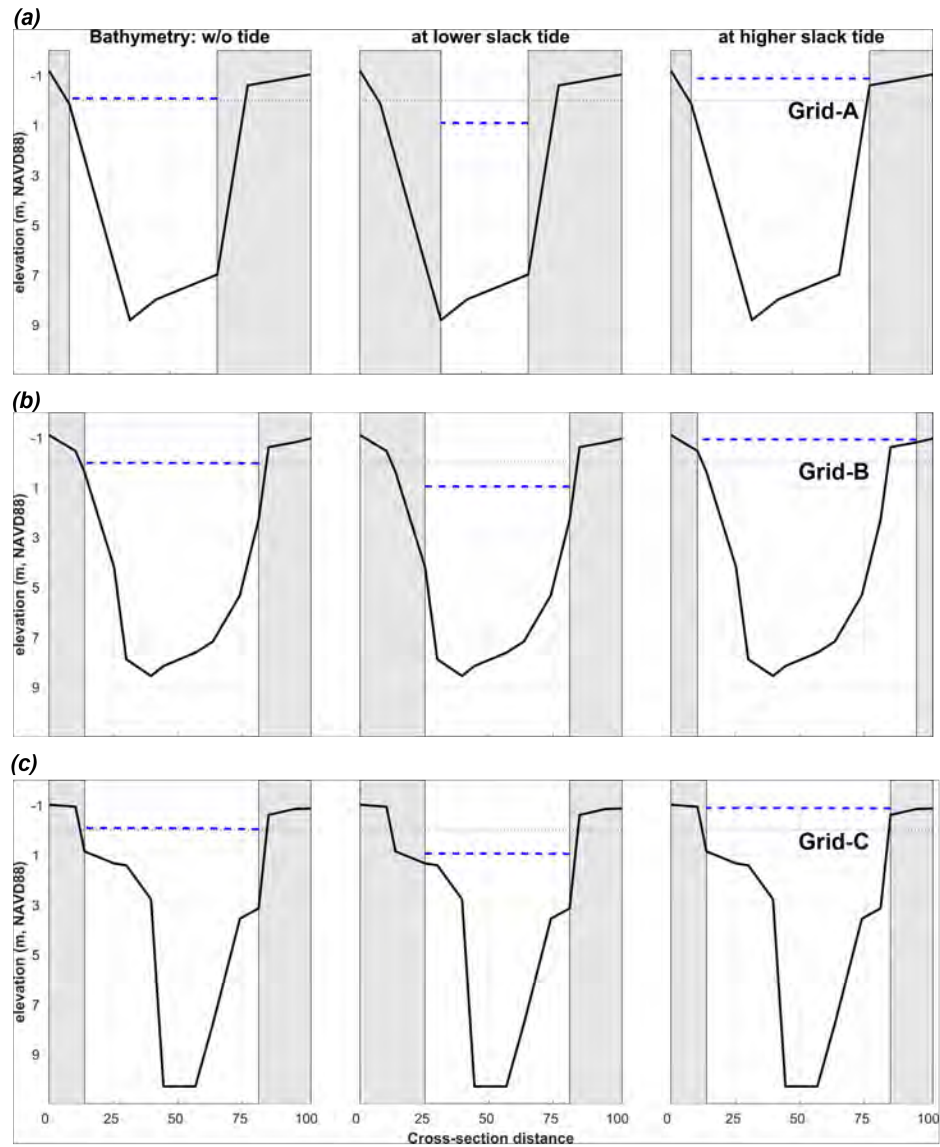
Figure 3.11: A channel cross-section showing Leipsic River hypsometry for different grid conditions (taken 3 km inward from the inlet mouth). Total water depth and width variation for still water, and during low and high tide are separated into three rows for different grids like Figure 3.10. Here, gray patch represent dry land seen by model grids during different tidal conditions and the corresponding loss in channel volume. Blue dashed line is the surface elevation and dotted black line is the NAVD88 vertical reference level (in meters).

.

74
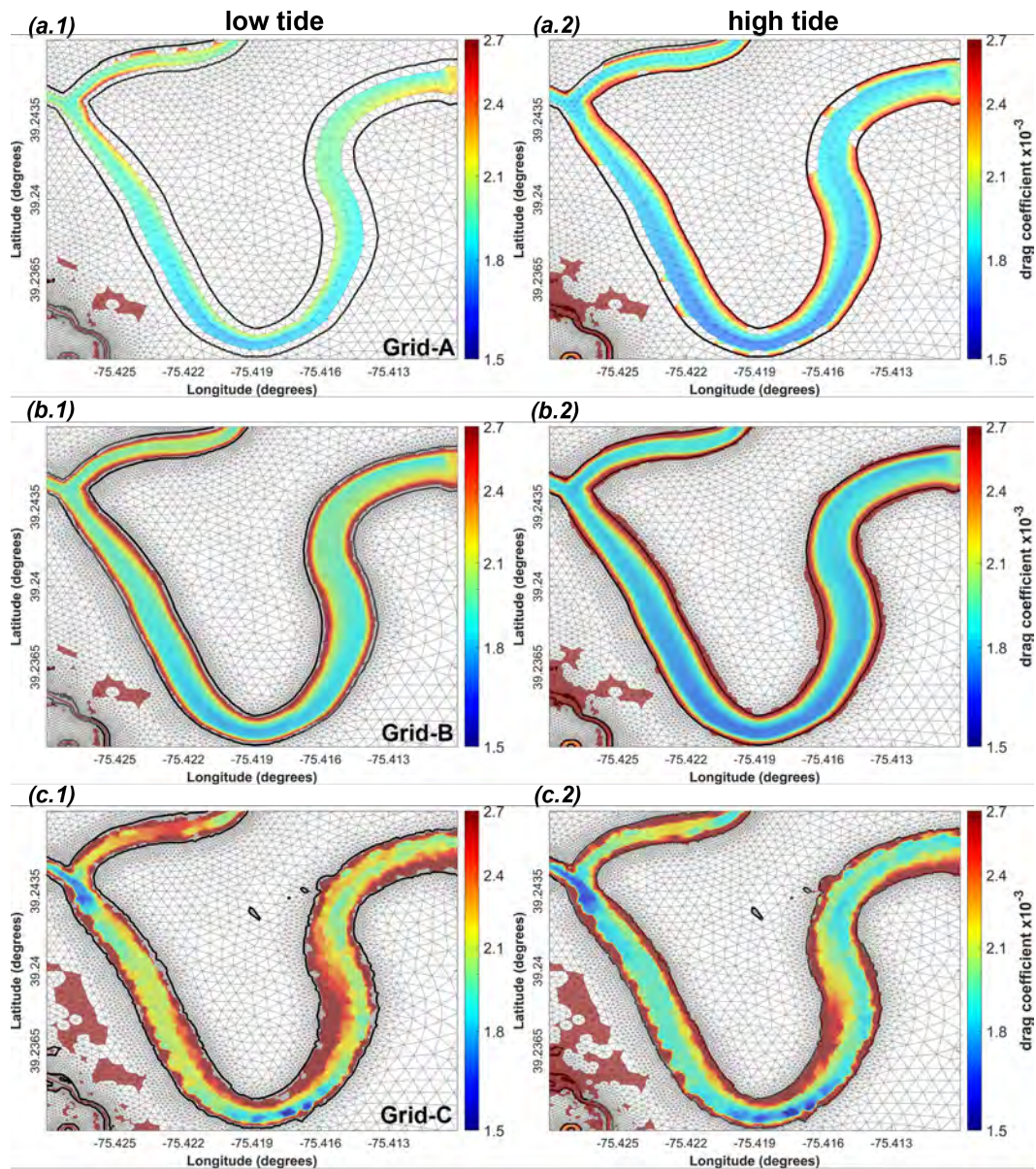
Figure 3.12: Drag coefficient, C_D during low and high tide estimated using the Manning formula and friction coefficient $n = 0.02$, separated into three rows for different grids: descriptions are similar to Figure 3.10.

The along-channel surface phase lag for different hypsometry conditions can be also explained in a mechanistic way by using the Saint Venant equations widely used for one-dimensional discharge routing in open channels. According to Brunner and Bonner (2010), for a gradually varying unsteady flow with irregular cross sections, the equations can be written as:

$$\frac{\partial A}{\partial t} + \frac{\partial Q}{\partial x} = 0 \qquad (3.4.1)$$

$$\frac{\partial Q}{\partial t} + \frac{\partial QU}{\partial x} + gA\left(\frac{\partial z}{\partial x} + S_f\right) = 0 \qquad (3.4.2)$$

where A is flow area of cross section (bH), Q is discharge (AU), U is x-direction velocity, and $z = z_0 + H$; z_0 is channel elevation and H is the total depth. The friction slope S_f using the Manning equation is

$$S_f = \frac{Q|Q|n^2}{2.208R^{4/3}A^2} \qquad (3.4.3)$$

where n is Manning's roughness coefficient and R is hydraulic radius, or cross-sectional area A divided by the wetted perimeter.

We developed a 1D unsteady model for the entire Leipsic River (Figure 3.13) using the Hydrologic Engineering Center's River Analysis System (version 5.0.7) – known as HEC-RAS, that solves equations 3.4.1-3.4.2. The bathymetric data set HEC-RAS includes 56 cross-sections taken from triangulated irregular network (TIN) data developed from different FVCOM grids, and a stage and flow boundary condition is assigned at the inlet cross-section using FVCOM model surface elevation and volume flux. The along-channel bathymetry representation in HEC-RAS is shown in the Figure 3.13.

For a channel with irregular bathymetry and rapid width contraction and expansion, the along and across-channel properties in equation 3.4.1-3.4.3 can be separated

using still water and tidally varying representations as

$$A(x,t) = A_0(x) \pm A'(x,t) \tag{3.4.4}$$

$$b(x,t) = b_0(x) \pm b'(x,t) \tag{3.4.5}$$

$$H(x,t) = h_0(x) + \eta(x,t) \tag{3.4.6}$$

Here, A_0, b_0 and h_0 represent the channel area, width and depth in a still water condition, and A', b' and η are the tidally varying components.

Among our model grids, Grid-A presents a unique situation where the inaccurate mesh design and the resulting rapid changes in channel width in a short period of time (due to wetting and drying), both in longitudinal and lateral direction (Figure 3.10a and 3.14a.1), controls the phase delay. During low tide, the spatial rate of change in channel width $\frac{\partial(b_0 - b')}{\partial x}$ is higher than the change in depth $\frac{\partial h_0}{\partial x}$, and dominates the changes in the flow area $\frac{\partial(A_0 - A')}{\partial x}$. Also, this along-channel rate of change is higher than the time rate of change of the wetted cross-sectional area, that ultimately reduces the channel conveyance and increase the surface phase lag. When tide rises to the level of marsh surface elevation, the along-channel artificial width convergence goes away and model recovers the full flow area. At this point, the time rate of change of the channel width, depth and wetted cross-sectional all become important again along with the spatial change, and contribute to the overall transport. This rapid change in channel cross-section from low model resolution is not trivial to explain using a 1D case and needs subgrid representation of the partially wet elements in 2D calculations. In Grid-B, with higher marsh-channel shoreline resolution shown in Figure 3.10b and 3.14a.2, the spatial and time rate of change in channel width $\frac{\partial b}{\partial x}$ and $\frac{\partial b}{\partial t}$ reduces, and also, as we have kept the same bathymetry, the spatial change in channel depth $\frac{\partial h_0}{\partial x}$ and bottom friction (Equation 3.4.3) remain similar to the values from Grid-A. From Figure 3.14c (top subplot), we can see that the surface phase lag has reduced as tide travels upstream and show a standing wave type condition, similar to the result shown earlier in Figure 3.9b using FVCOM. In Grid-C, the surveyed bathymetry data has altered

the along and across-channel bottom roughness and flow area significantly compared to Grid-B. While, in this case, the rate of change in channel width is similar to Grid-B, the spatial change in channel depth $\frac{\partial h_0}{\partial x}$ (Figure 3.14b.2), change in area $\frac{\partial A}{\partial x}$ and friction have become the dominant terms, ultimately reestablishing the phase lag between both gauges again (Figure 3.14c, bottom subplot).
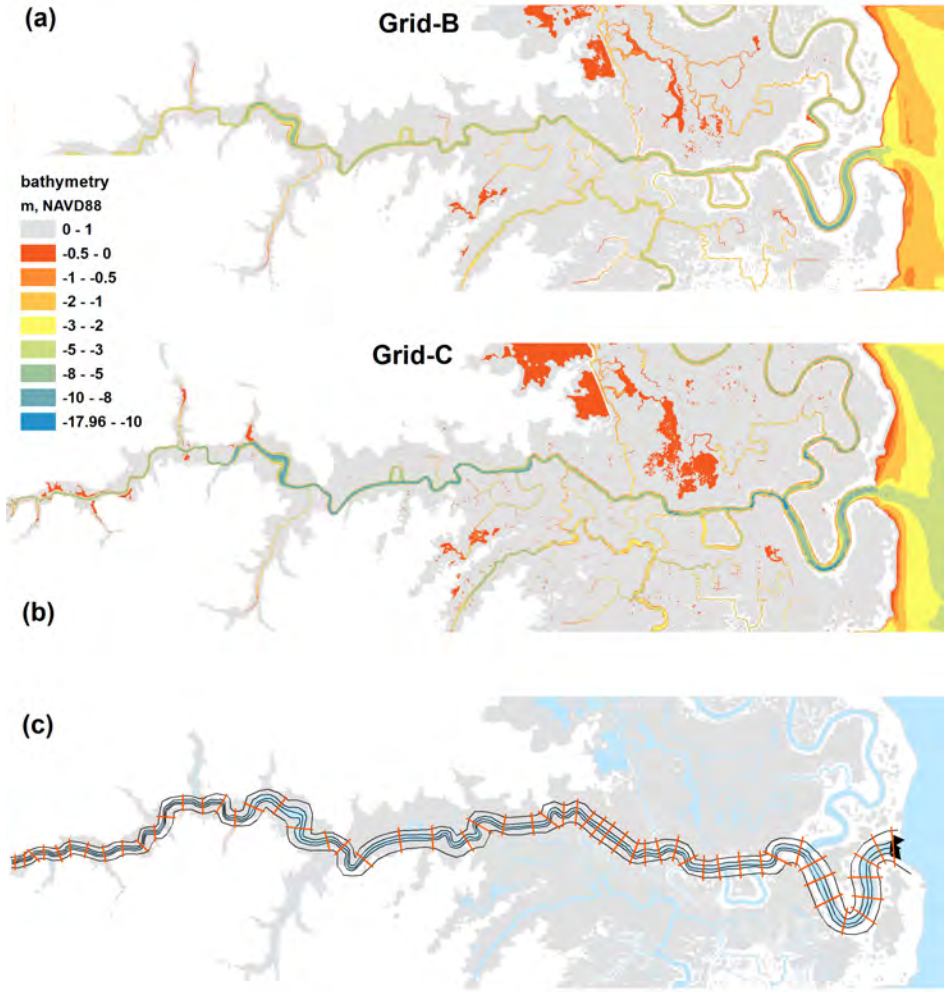
Figure 3.13: (a)-(b) Triangulated irregular network (TIN) data for Leipsic River HEC-RAS 1D simulations developed from the unstructured grid Grid-B and Grid-C bathymetry (in meters, from NAVD88 vertical reference level); (c) Channel cross-sections used for HEC-RAS 1D unsteady simulations.
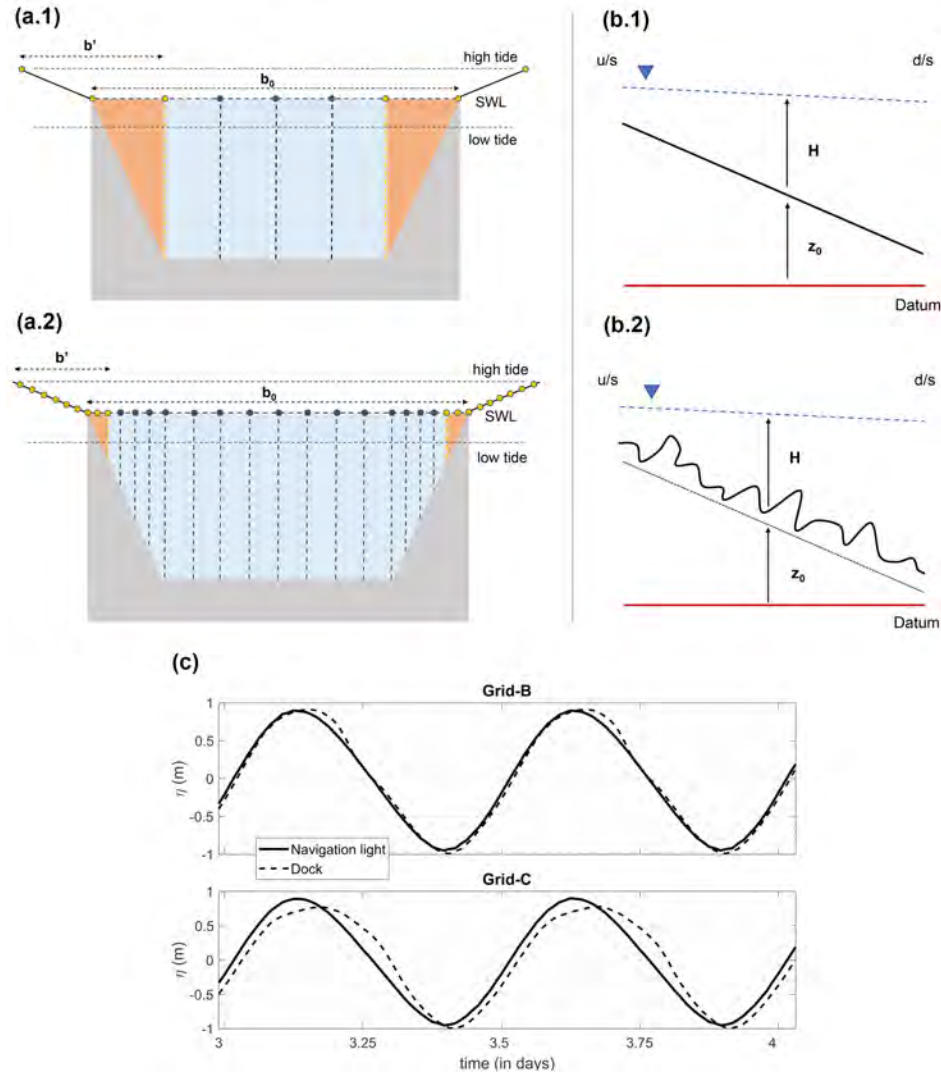
Figure 3.14: (a) Cross-section view of channel wetting and drying, and the respective width change in the model for different grids ; (a.1) channel representation in a low resolution grid (Grid-A), where the cells and nodes shown in orange color represent model active wet/dry domain; (a.2) similar representation in higher resolution grids (Grid-B and C); (b) Along-channel depth variation for different density in the survey data; (b.1) lower number of measured cross-sections (Grid-A and B); (b.2) higher density channel survey using zig-zag pattern (Grid-C). (c) Water surface elevation comparison between two gauge locations from Leipsic River inlet opening and model boundary: Navigation light and Dock using 1D Saint-Venant equations (in meters, from NAVD88 vertical reference level). Subplots from the top to bottom shows a sequence of result for different grid conditions, B-C.

3.4.3 Channel hypsometry and tidal wave regime

In Figure 3.15 and 3.16, with surface elevation we also have included current & flux information to compare the phase lag between them, which can provide more details on changes to the wave regimes. In our cases, we observed that the velocity/flux proceeds surface elevation by varying degrees based on the tidal stage at both inlet and channel boundary. We have estimated flux to take care of the channel geometry and across the channel velocity variation, and identified changes in relative phase $\phi_{\eta u}$ and $\phi_{\eta Q}$) to see the variation in tidal wave types.

For Grid-A, we can see that during flood tide, phase difference both $\phi_{\eta u}$ & $\phi_{\eta Q}$ increases slowly from 60° to almost 90° as the wave travels from inlet mouth to farther upstream (Figure 3.15 a,b). During flood, the increase in phase difference of $\phi_{\eta u}$ & $\phi_{\eta Q}$ is completely from the artificial channel width variation due to model wetting and drying. It is much more complicated for ebb tide as there is a reflection from the boundary and it displays characteristics of a standing wave at Dock (u/s location), where $\phi_{\eta u}$ & $\phi_{\eta Q}$ are even slightly higher than 90°. This case has a higher channel depth, corresponding lower bottom friction (Figure 3.12a), weak convergence, and the phase difference shown at locations close to inlet mouth and boundary are completely from significant width variation during rising and falling tide (Figure 3.10-3.12 (top row)). Throughout the channel, velocity and flux magnitude has dramatically decreased due to the cross-sectional area contraction, topographic dispersion and flow diversion toward a few smaller channels, while the surface elevation magnitude remains almost similar (Figure 3.15-3.16 a,b). We have observed good model performance using this Grid-A during both Hurricane Sandy and Joaquin when compared the surface elevation only. Interestingly, it can easily mislead into believing other subsequent model interpretation of velocity and flux estimation, as the velocity magnitude is completely out of order compared to the Grid-C, which is validated extensively with field measurements shown in Deb et al. (2018a). With the higher resolution in channels and berm location in Grid-B, the phase difference remains almost unchanged close to 80° during flood shown in Figure 3.15 and3.16 c-d, with a reduced magnitude in velocity and volume flux. At

the beginning of ebb tide, the phase difference between surface and velocity/flux, $\phi_{\eta u}$ and $\phi_{\eta Q}$ shows a complete reflection even at the inlet mouth, and they stay close to 90° which displays characteristics of a standing wave. In this case, channel caused a very little damping of the incident and reflected wave due to weak convergence, higher depth and low roughness even during the low tide (Figure 3.10-3.12 (middle row)). From Figure 3.15 c-d, we can see that the velocity magnitude is similar to the previous case at the inlet mouth, and almost doubled at the boundary during ebb. Grid-B with improved resolution completely misrepresents the tidal phase speed and surface-velocity/flux phase difference due to incorrect channel bathymetry data, ultimately reflected in our comparisons for Hurricane Sandy and Joaquin (Figure 3.5-3.6). Finally, in Grid-C with surveyed bathymetry , both $\phi_{\eta u}$ and $\phi_{\eta Q}$ show a different behavior than Grid-A and Grid-B, and the surface-velocity/flux phase lag seems to decrease with rising tide and wave regime represents a progressive type (Figure 3.15-3.16 e-f). During ebb, the cross-section averaged depth decreases, bottom friction becomes dominant and slows the incident wave propagation further. Figure 3.15 and 3.16 (f) shows the increase in phase lag between surface and velocity/flux at the boundary due to reflection and it reaches close to 90°, but then dampens due to frictional forces from well defined channel shoals. This case illustrates the time-dependent relationship between tidal phase speed and changes in channel width and depth, and how it changes between progressive and standing wave during high and low tide. Grid-C provided the most reliable performance considering both surface elevation and velocity comparisons, and the velocity comparisons are shown in Deb et al. (2020b), where Grid-C is used extensively.
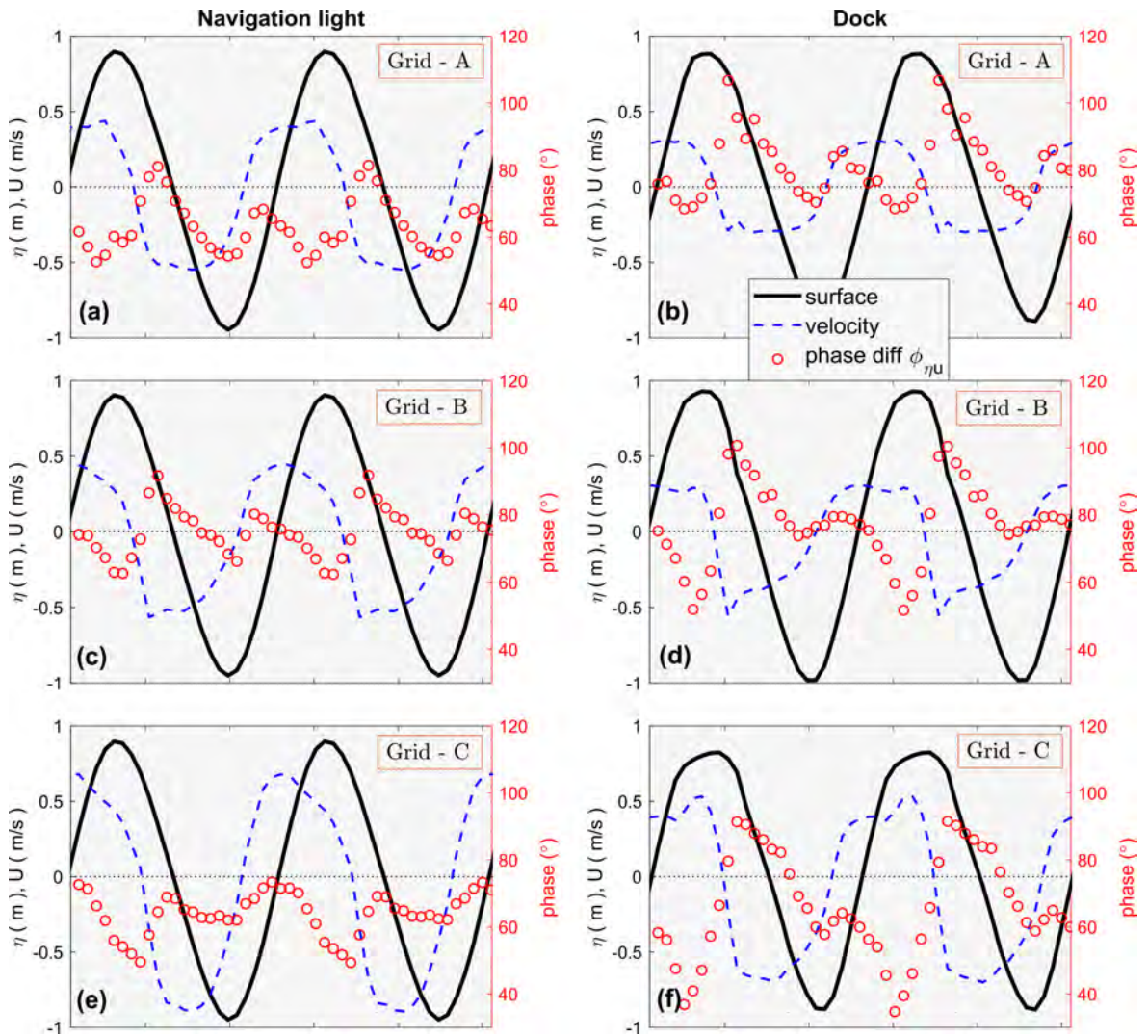
Figure 3.15: Phase difference (in degrees) between model water surface (in meters) and mid-channel velocity (in m/s) from two gauge locations at inlet channel opening and boundary: Navigation light and Dock respectively (separated into 2 columns). Subplots from the top to bottom (a,c,e & b,d,f) shows a sequence of result for different grid conditions, A-C.
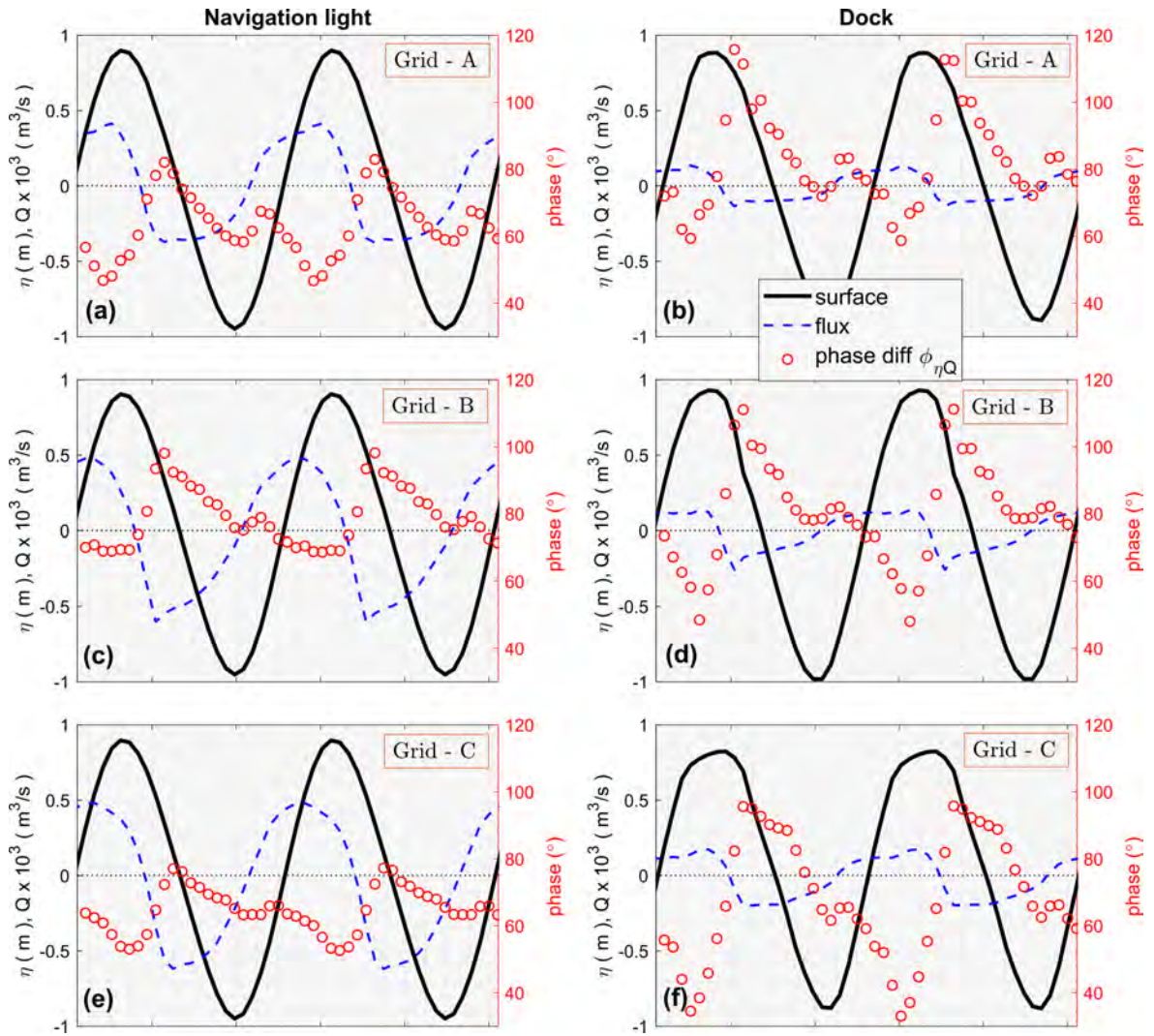
Figure 3.16: Phase difference (in degrees) between model water surface (in meters) and channel volume flux (in m³/s) from two gauge locations at inlet channel opening and boundary: Navigation light and Dock respectively (separated into 2 columns). Subplots from the top to bottom (a,c,e & b,d,f) shows a sequence of result for different grid conditions, A-C.

3.5   Concluding remarks and future works

We have presented an overview on how the accurate representation of wetland channel hypsometry can significantly improve the overall hydrodynamic modeling skill and reliability. Mainly, two important variables, model grid resolution around the marsh-channel shoreline and channel bathymetry are observed to define the model calculations for major physical processes. Inaccurate channel geometry from lower density survey and model resolution can provide good agreement with in-situ surface elevation data; however, completely misses the tidal velocity and phase. This better surface elevation and phase prediction are observed to result from the artificial channel convergence due to model low resolution around marsh edges. An increase in the grid resolution helped to identify the wet/dry boundary better, but has shown a dramatic decrease in the model skill because of the existing low density channel survey data that misrepresents the channel hypsometry and bottom friction. Finally, with a higher density channel survey inside the wetland, the model calculation of surface elevation has improved, along with the velocity magnitude and phase. Having an accurate estimate of the tidal velocity, and relative phase difference between current and surface are essential for determining asymmetry, wave regime and the residual flow. Ultimately, it contributes toward having a reliable hydrodynamic model, and further sediment transport calculations and net budget of the entire wetland system.

This study has shown the role of channel hypsometry only, and kept the influence of marsh topography separate for a different study. The marsh topography is an important variable in controlling the platform wetting and drying, and the estuary width variation. However, due to the modeling limitation: artificial ponding in isolated marsh depressions, we have shown the importance of wetland channels here in controlling the tidal hydrodynamics. More details on the artificial ponding and the necessary fixes are given in Deb et al. (2018a).

Chapter 4

A SURFACE POROSITY APPROACH FOR ELIMINATING ARTIFICIAL PONDING IN COASTAL SALT MARSH SIMULATIONS

4.1 Introduction

Coastal salt marshes around the globe are dynamic landscapes that go through continuous erosion-accretion phenomenon. They provide an important buffer against storm surge, wind waves and even tsunamis, and can act as a natural protection system. However, massive degradation of several salt marsh environments has been observed over the last few decades. These changes are possibly due to various anthropogenic and natural processes such as sea level rise, man-made morphology changes, over grazing by native and migratory species, and severe meteorological events. Salt marsh stability depends on tidal range, elevation of the marsh platform, weather variability and vegetation biomass (Mariotti and Fagherazzi, 2010). Also, the competition between SLR and sediment accumulation can control the marsh elevation, thus the stability (Mudd et al., 2013). The overall system represents a complex dynamic that depends on the nonlinear interaction between biological and physical processes. The vegetation biomass growth rate depends particularly on tidal amplitude, period and local elevation, resulting in different vegetation species that dominates different zones (Morris, 2006). Hydrodynamic forces like tidal current and wind waves suspend sediment from the channel and mudflat, and then spread the suspended sediment over the marsh platform through overtopping channel berms and the narrow creeks. Marsh vegetation interacts with sediment dynamics and raises the elevation by trapping inorganic sediment, and incorporating direct organic decomposition.

In recent decades, the field and numerical studies of salt marsh systems is an active matter of research because of continuous marsh loss. These studies have varied in terms of spatial scales, and solved long-term dynamics of the marsh boundary progradation or regression and platform evolution with time (e.g. D'Alpaos et al., 2007; Fagherazzi et al., 2012; Kirwan et al., 2016). Traditionally, in one-dimensional marsh transect, two-dimensional marsh platform, and large scale landscape models, the feedback between tidal elevation, vegetation dynamics, sediment transport and other climate variables (e.g., relative mean sea level (RMSL)) are taken into consideration to simulate wetland morphological processes (Fagherazzi et al., 2012).

All the vegetative and sedimentary processes over the marsh platform are primarily modeled based on the local tidal range, the flow exchange between channel and marsh flats (i.e., wetting and drying), and the depth, duration and frequency of inundation. At present, the modeling of hydrodynamic processes in a salt marsh system is a challenging task, because of the complex topographic features such as rills and cuts through channel berms, small creeks on marsh platform and the variation in the scale of such elements. They are often missing in the model grid due to both incomplete resolution in data sources such as LiDAR, as well as the loss of resolution in the development of DEM's and model grids (Figure 4.1d, 4.3a,b). Many of these small scale topographic features may be hidden under dense vegetation canopies and are thus not easily recognized using even higher resolution techniques such as Structure from Motion (SfM). Inadequate representation of these features leads to the artificial hydraulic isolation of depressions in the marsh surface, leading to artificial ponding and resulting inaccuracies in predictions of the depth and duration of inundation (Deb et al., 2018a). Subsequently, this error can lead to the incorrect selection process of vegetation species, and of the volume and speed of flooding and draining processes, which ultimately contributes to the estimation of sedimentation rates and marsh platform geomorphological evolution. Besides the landscape evolution, this artificial storage of water can initiate other significant defects for the wetland modeling community. The flood/ebb dominance in a multi-inlet wetland system depends mainly on channel configuration and

the inter-tidal volume storage. If the estuary width is much higher during high tide compared to low tide, the tidal wave propagates over the marsh surface slowly, and the system shows an ebb dominance overall. Model wetting/drying with significant ponding over marsh surface can alter the channel tidal asymmetry as the flood tide over marsh surface would propagate faster due to the reduced friction, changing the estuary width dramatically. Ultimately, it will provide an erroneous assessment of volume exchange, circulation, and net residual transport from the entire interconnected system. Moreover, this problem raises an issue also for the salt-marsh groundwater modeling community as the ponding can significantly increase surface-groundwater flow exchange, providing an artificial volume of water which in nature drains through the narrow channels on the marsh surface.

Resolving microtopography (i.e., cuts through channel berms and depressions) in numerical simulation of flooding and draining processes is challenging in terms of both computational time and memory storage, even using the two-dimensional shallow water models. Inadequate representation of the ground irregularities can change the dynamic wetting and drying processes, causing discrepancies in the numerical model mass and momentum conservation. Although numerous techniques and strategies have been implemented over the years to improve tidal inundation over marsh surface in large-scale coastal models (e.g. Defina et al., 1994; Bates and Hervouet, 1999), the adequate treatment of the hydraulic isolation of depressions over marsh surface is still a matter of concern. Defina (2000) proposed a marsh porosity concept using modified shallow water equations, where 3-D equations are phase (area) averaged over an element and depth-integrated to provide a stochastic representation of the ground unevenness and microscopic flow. The subgrid model has improved the wetting and drying phenomena on a complex topographic environment with much less computational effort. Subsequently, D'Alpaos and Defina (2007) coupled a 1D channel model with the subgrid model to improve the flow through marshes in the Venice lagoon. The 1D linear elements representing narrow channels are placed on the 2D domain, and only the intermediate scale channels were solved, which are more prominent in

length and size compared to the narrow cuts in BHNWR. While they have observed an improvement in subgrid model performance, there was no further analysis done on the marsh platform flooding and draining. Panday and Huyakorn (2004) and Jan et al. (2018) have proposed modified diffusion wave equations by incorporating the effects of microtopographic features (depression and obstructions) for areal overland flow simulations in integrated surface/subsurface inland watershed models. Both studies have considered a volumetric height in the governing equations to represent reduced storage volumes in isolated depressions, and a no-flow condition until the disconnected low points are filled with water. This strategy can be useful for hillslope overland flow simulations, whereas we need a different surface flow condition for the salt marshes where the depressions go through dynamic tidal flooding and draining due to the rills and cuts on the channel berms.

King (2000) implemented a thin slot algorithm in the two-dimensional hydrodynamic finite element model RMA2, where flow is allowed to occur through a low porosity zone when water surface elevation goes below the marsh ground elevation. Although Nielsen and Apelt (2003) have tested the sensitivity of different marsh parameters and wet/dry conditions in RMA2, and Proudfoot et al. (2018) calibrated the model in a complex floodplain environment, the model capability in predicting marsh platform inundation is still not very well known. Also, the equivalent water depth term in the governing equations is assigned in a non-conservative form, which could lead to an inaccurate mass and momentum conservation over the marsh surface.

In this study, we introduce a slot algorithm in the mass and momentum conservation equation to improve the representation of wetting and drying in artificially isolated depressions, using the Finite-Volume Coastal Ocean Model (FVCOM; Chen et al. (2013)) as a framework. We have followed the narrow slot or permeable-seabed technique used by Chen et al. (2000) and Kennedy et al. (2000) where the hydraulic depressions are considered as active fluid domain until the water surface elevation is below the lowest point of the depression/pond. Using narrow slots to represent flooding and draining through marsh depressions is justifiable, as, in reality, we can observe

the rills and cuts distributed along channel berms all over the marsh platforms, shown in Figure 4.3. While our modeling strategy is conceptually similar to Chen et al. (2000) and Kennedy et al. (2000) where the time-varying slot cross-section area is taken into account using a conservative form, but differs in porosity calculations based on marsh slot height and tidal elevation, and a modified momentum equation. We made the modifications primarily to eliminate artificial ponding effects observed in hydrodynamic model simulations in any coastal salt marsh systems. We have verified our proposed model correction strategy against an extensive set of pressure measurements obtained from a real marsh depression during different periods and marsh submergence conditions in Bombay Hook National Wildlife Refuge, DE.
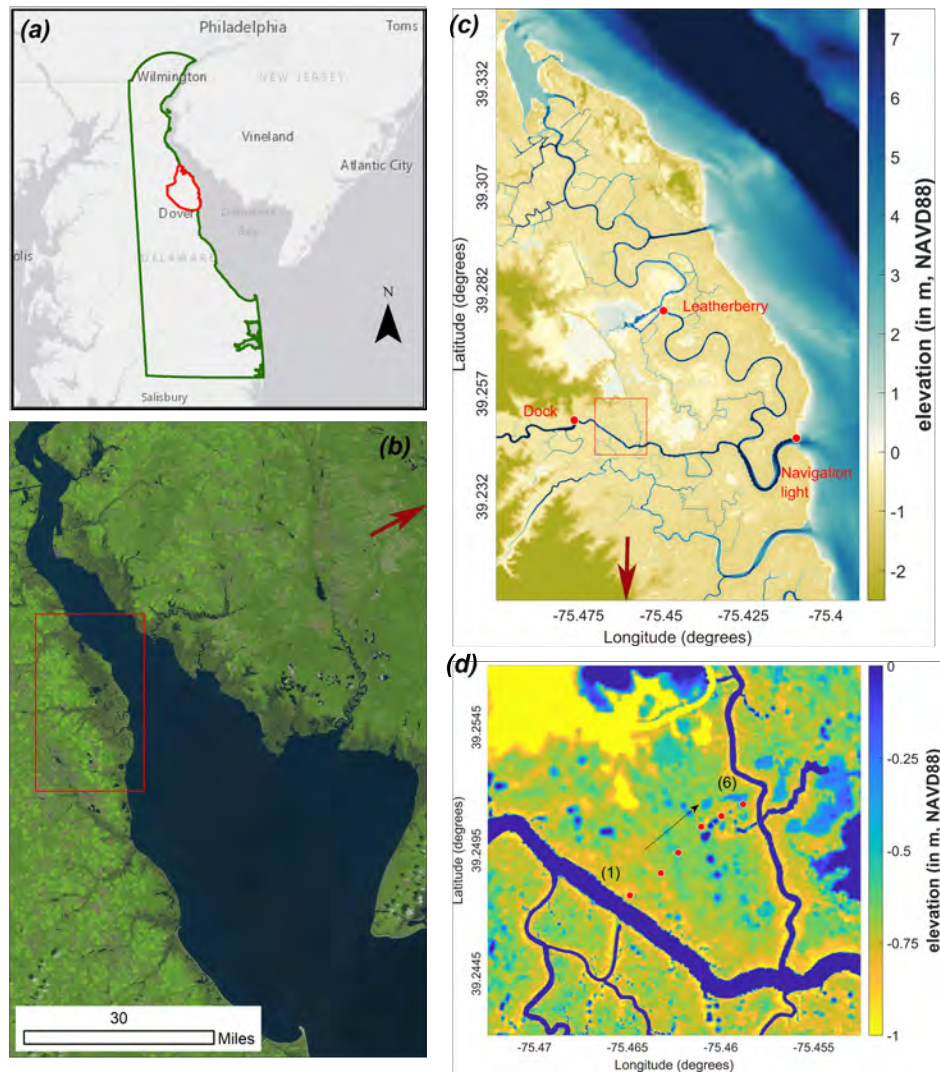
Figure 4.1: (a) The State of Delaware, USA. The red polygons show the study area, Bombay Hook National Wildlife Refuge, DE; (b) USGS Landsat imagery for the Delaware Bay (https://glovis.usgs.gov/); (c) NOAA 2011 LiDAR data set of marsh surface (Hund (2013); in meters, vertical datum: NAVD88). Red circles represent channel tide gauge locations used for model validation, and the rectangular box displays HOBO pressure gauge locations over a marsh depression; (d) Zoomed in view of the HOBO pressure gauge location on top of model elevation (in meters, vertical datum: NAVD88).

4.2   Artificial ponding over marsh platform

We use FVCOM to develop a high resolution, tidal creek resolving 2D hydrodynamic model for the BHNWR in Deb et al. (2020b). This model has been previously used in several estuarine and coastal studies featuring complex topo-bathymetry, intertidal wetting and drying, and irregular coastlines (Chen et al., 2008). We provide more details on the model governing equations and wetting/drying scheme in the following section.

The unstructured grid channel bathymetry data is collected during an extensive bathymetric survey, and the marsh topography is interpolated from the vegetation bias-corrected LiDAR DEM of the area. The model is driven by a large scale three-dimensional model (Kukulka et al., 2017) based on the Coupled-Ocean-Atmospheric-Wave-Sediment Transport (COAWST) modeling framework (Warner et al., 2010) that provided current and surface elevations to the FVCOM model. We evaluated the model performance in Deb et al. (2020b) at point locations, for a time frame from April to October 2015 and during two extreme events Hurricane Sandy in 2012 and Hurricane Joaquin in 2015, in term of water surface elevation and current in open water, marsh interior channels and on marsh flats shown in Figure 4.1. Both extreme meteorological events used for model validation: Hurricane Sandy (2012) and Hurricane Joaquin (2015) had threatened the Delaware Bay with storm surge and large-scale coastal flooding. Comparison of surface elevation and current data sets at the gauge locations in the BHNWR and Delaware Bay described in Deb et al. (2020b) showed good agreement between the model and in-situ data in the Bay and interior channels. However, the model results over the marsh platform showed a static water surface elevation during ebb, exhibiting artificial ponding at HOBO pressure gauge locations 3-6, shown in Figure 4.2. This elevated depth represents a continuous storage of water on the marsh platform due to artificially isolated low spots or depressions in the model DEM formed by channel berms, mentioned in the previous section. It is mostly observed after a spring tide or surge event, when the water level overtops the channel berms and inundates most of the low-marsh area. Although grid resolution refinement can help to

resolve the cuts and rills on channel berms, a substantial computational resource and higher resolution LiDAR data with negligible vegetation bias are required. In other words, it is almost impossible to resolve the fine-scale features present on the marsh surface using remotely sensed data and current technology.

Figure 4.3 a-c and 4.4a show an example of the ponding and drainage problem over the BHNWR marsh platforms during low tide, where the entire wetland is first flooded by providing a maximum tidal elevation of 2 m and then allowed to drain gradually for a couple of hours. Figure 4.3a shows the LiDAR DEM representation (~ 1 m) of the deployed HOBO pressure gauge area, where the meter-scale rills and creeks over the marsh platform are visible that floods and drains this depression following the tide cycle. Although the LiDAR survey identified the cuts, it misrepresented the actual depth of these structures because of the dense vegetation and some level of submergence during the survey. Subsequently, when we interpolated this elevation into the model unstructured grid of lower resolution ($\sim 3 - 5$ m), a systematic error associated with the horizontal interpolation and smoothing added further inaccuracy in interpreting the marsh surface, shown in Figure 4.3b. We can see that the artificial storage of water resulted immediately at the isolated depressions on the marsh platform (Figure 4.3c) that originally drains using the marsh cuts shown in Figure 4.3 d-e. The drainage problem was more evident after evaluating the total volume of water going in and out of the system, mainly when severe surges are under consideration. The results for Hurricane Sandy and Hurricane Joaquin are shown in Figure 4.4 c,d. First, volume exchange between marsh and bay is shown in the upper panel (b) separated by the black line at zero depth (NAVD88), and the model grid elements are divided into dry (gold) and wet (blue) using static bathymetry data to estimate instant volume at the channels and marshes separately. Figure 4.4 c,d middle panel shows the volume stored in the channel areas, and indicates that the tidal/surge fluxes are fluctuating in channels as expected. From the bottom panel of Figure 4.4 c,d, we can see that the model suffers from poor channel connectivity, and the marsh area retains a static volume of water following the complete platform inundation. For both events, the

estimates of the stored amount are almost similar after the main surge period, and they are comparable to the maximum channel volume exchange per cycle, approximately 1.0×10^7 m^3. Additional set of videos are given as supplementary material to illustrate the model artificial ponding during Hurricane Sandy (2012), and the real-time marsh surface draining via narrow slots.
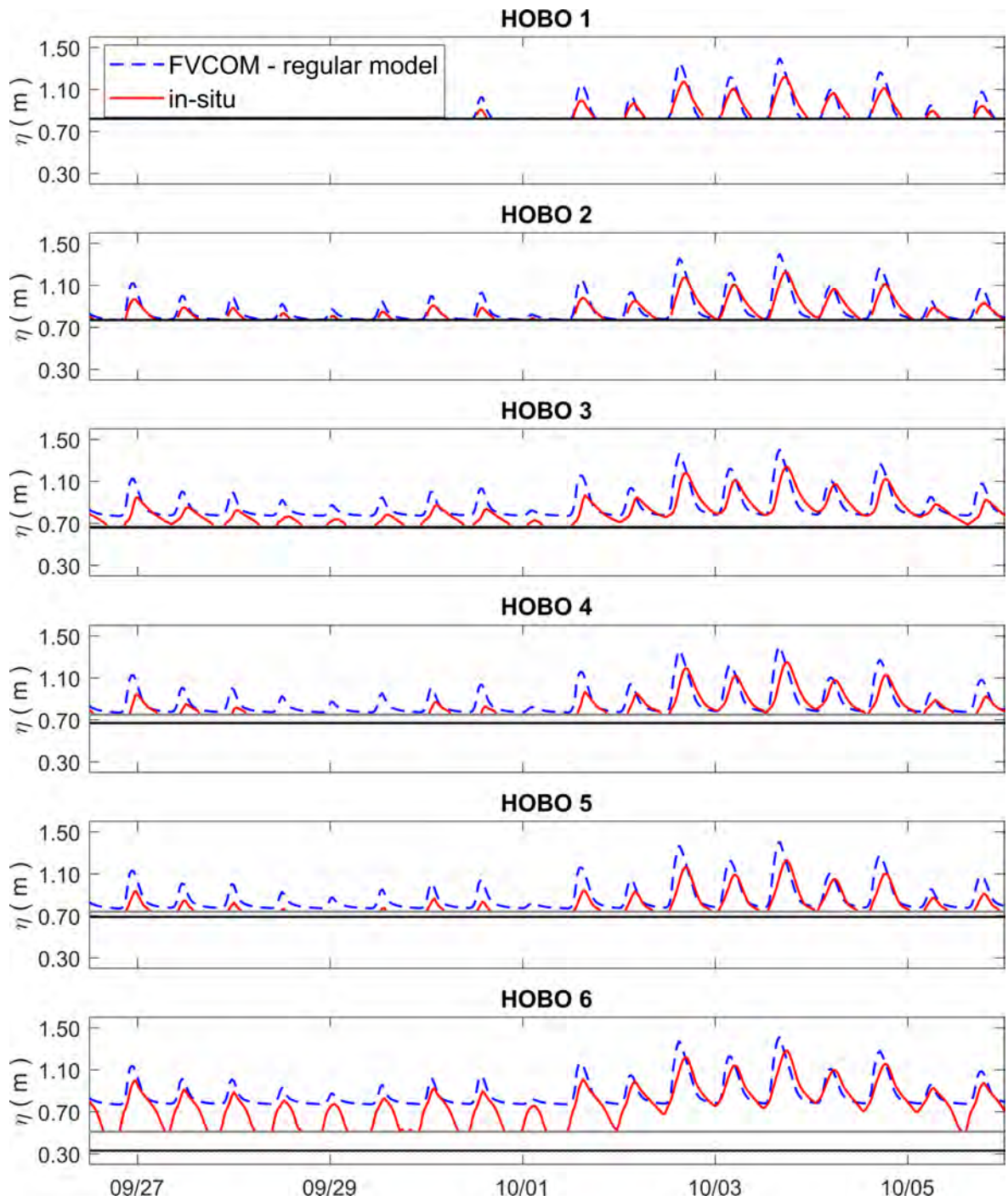
Figure 4.2: A comparison between FVCOM model (in blue) and in-situ (in red) water surface elevation during Hurricane Joaquin, 2015 at different HOBO gauge locations (in meters, from NAVD88 vertical reference level). The black and gray straight lines represent FVCOM model grid and surveyed bottom elevation.
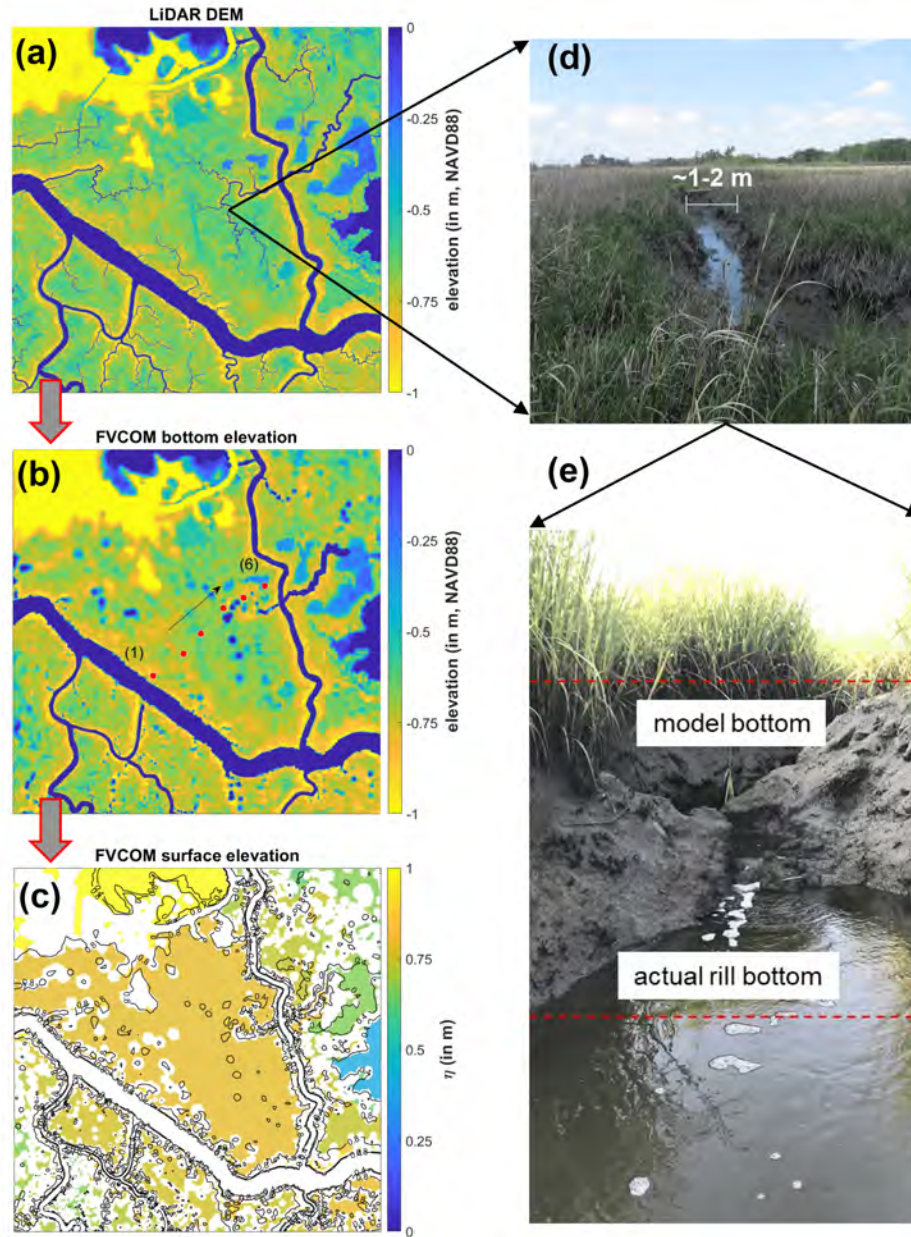
Figure 4.3: Ponding and drainage problem over the BHNWR marsh platform HOBO gauge locations during a low tide. (a) NOAA 2011 LiDAR DEM elevation (in meters); (b) Unstructured grid bottom elevation (in meters); (c) A snapshot of model surface elevation during a low tide and artificial ponding on the HOBO location (in meters); (d-e) Meter-scale features: cuts and rills over marsh platform that drains a depression. Red dashed lines show the difference between actual rill bottom and the elevation seen by the model.
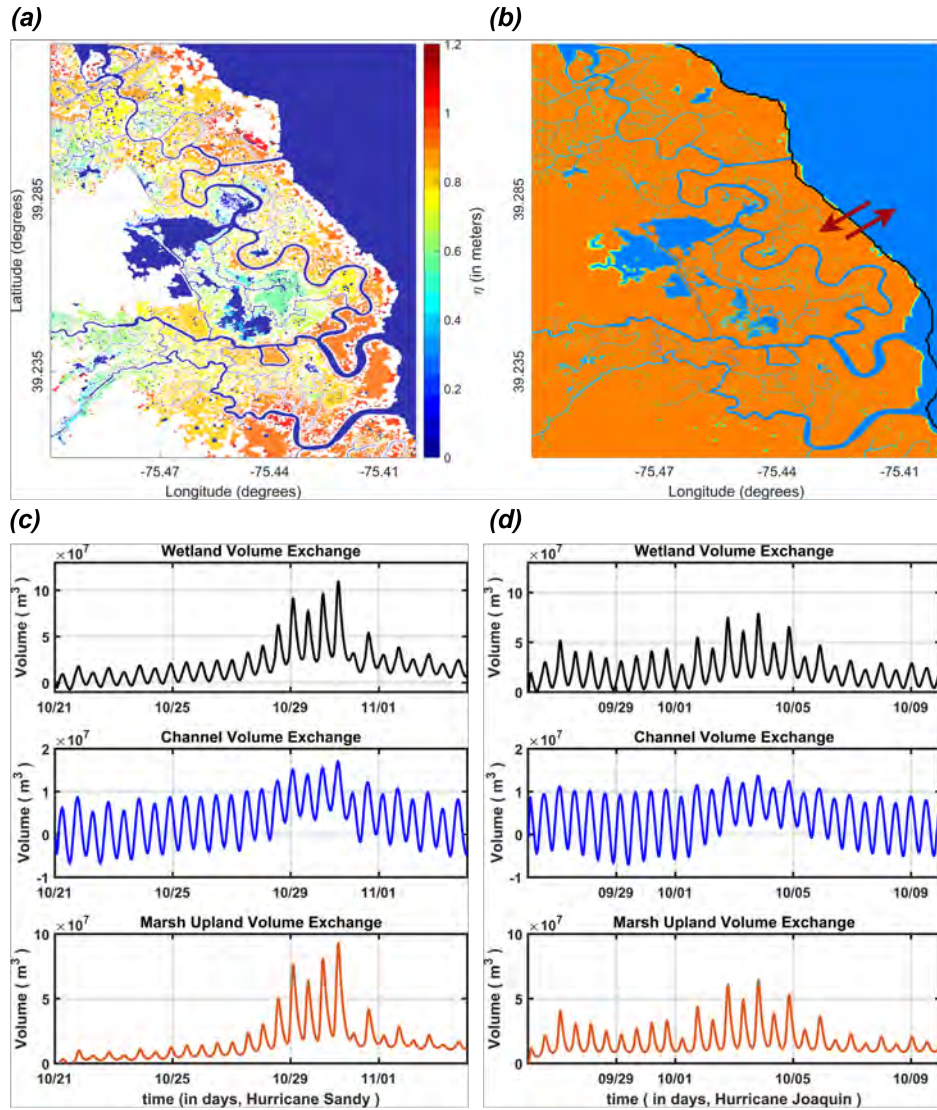
Figure 4.4: (a) A snapshot of model surface elevation during a low tide and artificial ponding on the entire marsh platform. The colorbar on the right side represents water surface elevation (in meters, from NAVD88 vertical reference level); (b) Wet (blue) and dry (golden) cells at calm (t = 0); panel (c) Time series of water volume, inundated wetland cells (top) and drained to the wetland interior channels (middle) and residual trapped water on marsh cells (bottom) indicating the artificial ponding problem during Hurricane Sandy, 2012; (d) Similar estimations like (c) during Hurricane Joaquin, 2015.

4.3 Description of the numerical model and modifications

4.3.1 FVCOM

FVCOM is a three-dimensional model originally developed by Chen et al. (2008). It uses an unstructured triangular grid in the horizontal to better represent the coastal geometry. FVCOM has been previously successfully applied in several estuarine and coastal studies featuring wetting and drying in complex topo-bathymetry and macrotidal salt marshes Chen et al. (2008); Huang et al. (2008). In this study, we modify the 2D vertically integrated equations and the wetting and drying criteria to improve marsh platform flooding and draining in artificially isolated depressions.

4.3.1.1 Governing equations

The original FVCOM 2D vertically integrated, barotropic mode, continuity and momentum equations are

$$\frac{\partial \eta}{\partial t} + \frac{\partial (\bar{u} H)}{\partial x} + \frac{\partial (\bar{v} H)}{\partial y} = 0 \tag{4.3.1}$$

$$\frac{\partial \bar{u} H}{\partial t} + \frac{\partial \bar{u}^2 H}{\partial x} + \frac{\partial \bar{u} \bar{v} H}{\partial y} - f\bar{v}H = -gH\frac{\partial \eta}{\partial x} - \tau_{bx} + H\tilde{F}_x + G_x \tag{4.3.2}$$

$$\frac{\partial \bar{v} H}{\partial t} + \frac{\partial \bar{u} \bar{v} H}{\partial x} + \frac{\partial \bar{v}^2 H}{\partial y} + f\bar{u}H = -gH\frac{\partial \eta}{\partial y} - \tau_{by} + H\tilde{F}_y + G_y \tag{4.3.3}$$

where x and y are the east and north axes of the Cartesian coordinate; $\bar{u}$ and $\bar{v}$ are the depth-averaged x, y velocity components; η is surface elevation, $H = h + \eta$ is total water depth, and τ_{bx} and τ_{by} are the x and y components of bottom stress, respectively. The difference between nonlinear terms based on vertically-averaged 2-D variables and terms resulting from vertical integration of 3-D variables are given by G_x and G_y,

defined by (Chen et al., 2013)

$$G_x = \frac{\partial \bar{u}^2 H}{\partial x} + \frac{\partial \bar{u}\bar{v}H}{\partial y} - H\tilde{F}_x - \left[\frac{\partial \overline{u^2}H}{\partial x} + \frac{\partial \overline{uv}H}{\partial y} - H\overline{F}_x\right] \qquad (4.3.4)$$

$$G_y = \frac{\partial \bar{u}\bar{v}H}{\partial x} + \frac{\partial \bar{u}^2 H}{\partial y} - H\tilde{F}_y - \left[\frac{\partial \overline{uv}H}{\partial x} + \frac{\partial \overline{v^2}H}{\partial y} - H\overline{F}_y\right] \qquad (4.3.5)$$

where

$$H\tilde{F}_x \approx \frac{\partial}{\partial x}\left[2\bar{A}_m H \frac{\partial \bar{u}}{\partial x}\right] + \frac{\partial}{\partial y}\left[\bar{A}_m H\left(\frac{\partial \bar{u}}{\partial y} + \frac{\partial \bar{v}}{\partial x}\right)\right] \qquad (4.3.6)$$

$$H\overline{F}_x \approx \frac{\partial}{\partial x}\overline{2A_m H \frac{\partial u}{\partial x}} + \frac{\partial}{\partial y}\overline{A_m H\left(\frac{\partial u}{\partial y} + \frac{\partial v}{\partial x}\right)} \qquad (4.3.7)$$

$$H\tilde{F}_y \approx \frac{\partial}{\partial x}\left[\bar{A}_m H\left(\frac{\partial \bar{u}}{\partial y} + \frac{\partial \bar{v}}{\partial x}\right)\right] + \frac{\partial}{\partial y}\left[2\bar{A}_m H \frac{\partial \bar{v}}{\partial y}\right] \qquad (4.3.8)$$

$$H\overline{F}_y \approx \frac{\partial}{\partial x}\overline{A_m H\left(\frac{\partial u}{\partial y} + \frac{\partial v}{\partial x}\right)} + \frac{\partial}{\partial y}\overline{2A_m H \frac{\partial v}{\partial y}} \qquad (4.3.9)$$

Here, A_m is the horizontal eddy diffusion coefficient and the overline $\overline{(\cdot)}$ denotes the depth-averaged value. The bottom friction in 2D FVCOM is calculated using a drag coefficient formulation

$$(\tau_{bx}, \tau_{by}) = C_D\sqrt{\bar{u}^2 + \bar{v}^2}(\bar{u}, \bar{v}) \qquad (4.3.10)$$

where the drag coefficient C_D is calculated using the total depth and Manning's n values as

$$C_D = \frac{gn^2}{H^{1/3}} \qquad (4.3.11)$$

These equations are solved in a horizontal computational domain which is subdivided into a set of nonoverlapping unstructured triangular cells. An unstructured triangle consists of three nodes, a centroid, and three sides, and the surface elevation η and depth H are placed at the nodes and velocity $\bar{u}$ and $\bar{v}$ are at the cell centroids, shown in Figure A1. The surface elevation η is calculated by integrating the flux going in and out of a control volume, and the variables at the cell centroid are calculated based on the flux through the sides. For more detail about the 2D external mode

discretization, the reader is referred to Appendix A and Chen et al. (2013).

4.3.1.2 Treatment of wetting/drying in the standard FVCOM model

To simulate the flooding/draining process over intertidal land surfaces, a wetting/drying scheme has been incorporated into FVCOM using the concept of a minimum water depth D_{min}. When local water depth is less than D_{min}, the cell is assigned as a dry cell and its velocity is set to zero. When the surface elevation rises back during the flood tide and thickness exceeds D_{min}, the cells are considered as wet and its velocity and elevation are computed by solving the governing equations.

According to the model present setup, the water depth $H = \eta - h_m + D_{min}$, where h_m is the model bottom elevation, and the wet/dry criterion for node points is given by

$$\begin{cases} \text{wet,} & \text{if } H = \eta - h_m + D_{min} > D_{min} \\ \text{dry} & \text{if } H = \eta - h_m + D_{min} \leq D_{min} \end{cases} \quad (4.3.12)$$

and for triangular cells is given by

$$\begin{cases} \text{wet,} & \text{if } H = \max\left(\eta_{\hat{i}}, \eta_{\hat{j}}, \eta_{\hat{k}}\right) - \min\left(h_{m,\hat{i}}, h_{m,\hat{j}}, h_{m,\hat{k}}\right) + D_{min} > D_{min} \\ \text{dry,} & \text{if } H = \max\left(\eta_{\hat{i}}, \eta_{\hat{j}}, \eta_{\hat{k}}\right) - \min\left(h_{m,\hat{i}}, h_{m,\hat{j}}, h_{m,\hat{k}}\right) + D_{min} \leq D_{min} \end{cases} \quad (4.3.13)$$

where $\hat{i}$, $\hat{j}$ and $\hat{k}$ are the integer numbers to identify the three node points of a triangular cell.
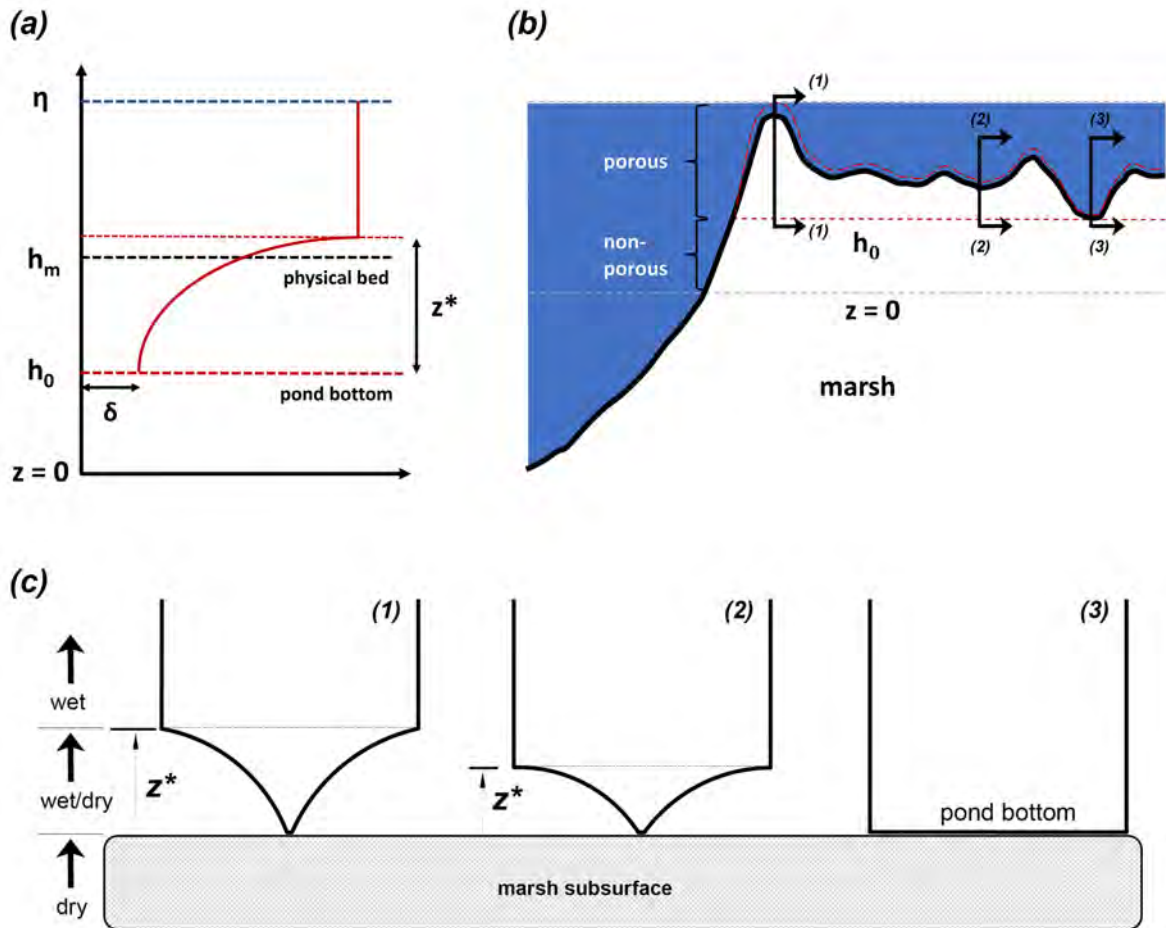
Figure 4.5: (a) Idealized representation of slot height z^* and flow section with respect to a marsh elevation; (b) Example of model artificial ponding over a marsh platform after channel berm overtopping during high tide; (c) Sketch of the proposed model wet/dry conditions, and spatial changes in slot cross-section from channel berm to the marsh depression.

4.3.2 Description of marsh porosity using slot algorithm

4.3.2.1 Specification of the slot geometry

In this section, we derive the narrow slot or permeable-seabed properties that changes the mass and momentum conservation equations in FVCOM. Figure 4.5 shows a schematic of the slot distribution over marsh depression where Figure 4.5c (bottom subplot) represents the vertical variation of slot width and cross-section area. The horizontal slot area with respect the unit area of the element can be defined as

$$\beta(z) = \begin{cases} \delta + (1-\delta)e^{\lambda[z-(h_0+z^*)]}; & h_0 < z \le h_0 + z^* \\ 1; & z > h_0 + z^* \end{cases} \tag{4.3.14}$$

where δ is the slot area relative to a unit area of the element; λ is the shape parameter that controls the smooth transition of the horizontal area from an unit area to a narrow slot; h_0 is a reference bottom elevation of the marsh pond/depression; and z^* denotes the elevation of the marsh from h_0 where $\beta = 1$. Using water surface elevation η and time-varying slot area β, we derive the volume per unit horizontal area as

$$\Lambda(\eta) = \int_{h_0}^{\eta} \beta(z)dz \tag{4.3.15}$$

$$\Lambda(\eta) = \begin{cases} \int_{h_0}^{z^*} \beta(z)dz + (\eta - [h_0 + z^*]); & \eta > h_0 + z^* \\ \int_{h_0}^{\eta} \beta(z)dz; & \eta \le h_0 + z^* \end{cases} \tag{4.3.16}$$

Integrating Equation 4.3.16 for both surface elevation conditions, we get

$$\Lambda = \begin{cases} \delta(\eta - h_0) + \frac{(1-\delta)}{\lambda}\left[e^{\lambda[\eta-(h_0+z^*)]} - e^{-\lambda z^*}\right]; & h_0 < \eta \le h_0 + z^* \\ [\eta - (h_0 + z^*)] + \delta z^* + \frac{(1-\delta)}{\lambda}\left[1 - e^{-\lambda z^*}\right]; & \eta > h_0 + z^* \end{cases} \tag{4.3.17}$$

Small mass loss can occur based on the choice of z^* when the water level is below the top of the slot, as the water must first fill the slots before wetting the dry

surface. We defined z^* in a similar way it is done in Kennedy et al. (2000) where once the surface elevation is above the top of the slot, the overall volume is kept identical to that if there was no slot existed. Equating the volume per unit horizontal area with and without a slot leads to

$$[\eta - (h_0 + z^*)] + \delta z^* + \frac{(1-\delta)}{\lambda}\left[1 - e^{-\lambda z^*}\right] = \eta - h_m \tag{4.3.18}$$

For a $\delta \ll 1$ and $\lambda \gg 1$, the slot height z^*, will be near $h_m - h_0$. Using a Taylor series expansion of the term $\frac{e^{-\lambda z^*}}{\lambda}$ from $h_m - h_0$, we get

$$\begin{aligned} z^* &= \frac{h_m - h_0}{(1-\delta)\left[1 - e^{-\lambda(h_m-h_0)}\right]} + \frac{1}{\lambda\left[1 - e^{-\lambda(h_m-h_0)}\right]} \\ &\quad - \frac{e^{-\lambda(h_m-h_0)}}{\left[1 - e^{-\lambda(h_m-h_0)}\right]}\left[\frac{1}{\lambda} + (h_m - h_0)\right] \end{aligned} \tag{4.3.19}$$

Since $\lambda \gg 1$, Equation 4.3.19 can be simplified as

$$z^* = \frac{h_m - h_0}{1 - \delta} + \frac{1}{\lambda} \tag{4.3.20}$$

From Equation 4.3.20, we see that for $\delta \ll 1$ and $\lambda \gg 1$, $h_0 + z^*$ becomes the original model bottom elevation h_m (Figure 4.5a).

4.3.2.2   Modified mass and momentum conservation equations

Defina (2000) derived a set of 2D shallow water equations for partially wet elements by implementing a phase-averaging process to the Reynolds-averaged Navier Stokes equations and then integrating over depth. The phase-averaging $\langle \, \rangle$ represents averaging of a generic variable of the flow field $f(\mathbf{x}, t)$ over an element area A, with the average written as

$$\langle \phi f \rangle \equiv \frac{1}{A}\int_A \phi f \, dA \tag{4.3.21}$$

The phase function ϕ indicates whether a point lies above the local, high-resolution

bed and is given by

$$\phi(\mathbf{x}) = \begin{cases} 1; & z = h_m(\mathbf{x}) \\ 0; & z < h_m(\mathbf{x}) \end{cases} \tag{4.3.22}$$

where h_m denotes the local bottom elevation and $\mathbf{x}$ is the vector of spatial coordinate (x, y, z). The phase-average satisfies the following rules

$$\frac{\partial}{\partial t}\langle\phi(\mathbf{x})f(\mathbf{x},t)\rangle = \frac{1}{A}\int_A \phi(\mathbf{x})\frac{\partial f(\mathbf{x},t)}{\partial t}dA = \langle\phi(\mathbf{x})\frac{\partial f(\mathbf{x},t)}{\partial t}\rangle \tag{4.3.23}$$

$$\nabla\langle\phi(\mathbf{x})f(\mathbf{x},t)\rangle = \langle\nabla\phi(\mathbf{x})f(\mathbf{x},t)\rangle \tag{4.3.24}$$

Assuming a gradually varied flow condition where η changes smoothly over the entire domain, it can be shown that

$$\langle\varphi(\mathbf{x})f(\mathbf{x},t)\nabla\eta\rangle = \langle\varphi(\mathbf{x})f(\mathbf{x},t)\rangle\nabla\eta \tag{4.3.25}$$

The portion of a horizontal element cross-sectional area above the bottom is given by

$$\langle\phi\rangle = \frac{1}{A}\int_A \phi dA = \beta(z) \tag{4.3.26}$$

In our case, the $\langle\phi\rangle$ calculation is different as described by Equation 4.3.14, where $\beta(z)$ is given for the present slot geometry, and

$$\langle\phi\rangle(z=\eta) = \langle\phi\rangle|_\eta = \beta|\eta \tag{4.3.27}$$

is the wetted surface area, with values of $\beta_\eta = 1$ if η lies above the highest value of $z = h_0 + z^*$ within the cell, has a value greater than zero as long as η is above the rill elevation h_0 in a cell.

The continuity equation for homogeneous, incompressible fluid is given by

$$\nabla \cdot \mathbf{u} = 0 \quad h_0(\mathbf{x}) \leq z \leq \eta(\mathbf{x}, t) \tag{4.3.28}$$

Kinematic surface and bottom boundary conditions are given by

$$\frac{\partial \eta}{\partial t} + u\frac{\partial \eta}{\partial x} + v\frac{\partial \eta}{\partial y} - w = 0; \quad z = \eta \tag{4.3.29}$$

$$u\frac{\partial h_0}{\partial x} + v\frac{\partial h_0}{\partial y} - w = 0; \quad z = h_0 \tag{4.3.30}$$

Applying phase-averaging to Equation 4.3.28 gives

$$\langle \phi \nabla \cdot \mathbf{u} \rangle = 0 \tag{4.3.31}$$

which may be manipulated to obtain

$$\langle \nabla \cdot (\phi \mathbf{u}) \rangle + \langle \mathbf{u} \cdot \nabla \phi \rangle = 0 \tag{4.3.32}$$

$\nabla \phi = 0$ except the bottom where it is normal to the flow. Equation 4.3.32 reduces to

$$\nabla \cdot \langle \phi \mathbf{u} \rangle = 0 \tag{4.3.33}$$

Let

$$\mathbf{U} = \langle \phi \mathbf{u} \rangle \tag{4.3.34}$$

The phase-averaged continuity equation becomes

$$\nabla \cdot \mathbf{U} = 0 \tag{4.3.35}$$

Integrating the phase-averaged continuity equation from h_0 to η gives

$$\int_{h_0}^{\eta} \nabla \cdot \mathbf{U} dz = 0 \tag{4.3.36}$$

Applying Leibnitz' rule, we obtain

$$\frac{\partial}{\partial x}\int_{h_0}^{\eta} U dz - U|_{\eta}\frac{\partial \eta}{\partial x} + \frac{\partial}{\partial y}\int_{h_0}^{\eta} V dz - V|_{\eta}\frac{\partial \eta}{\partial y} + W|_{n} - W|_{h_0} = 0 \qquad (4.3.37)$$

The phase-averaged surface boundary condition is

$$\langle \phi \frac{\partial \eta}{\partial t}\rangle + \langle \phi u \frac{\partial \eta}{\partial x}\rangle + \langle \phi v \frac{\partial \eta}{\partial y}\rangle - \langle \phi w \rangle = 0 \qquad (4.3.38)$$

Using Equation 4.3.25, we can write Equation 4.3.38 as

$$\langle \phi \rangle\frac{\partial \eta}{\partial t} + \langle \phi u \rangle\frac{\partial \eta}{\partial x} + \langle \phi v \rangle\frac{\partial \eta}{\partial y} - \langle \phi w \rangle = 0 \qquad (4.3.39)$$

Here, $\langle \phi \rangle|_{\eta} = \beta|_{\eta}$, $\langle \phi u \rangle|_{\eta} = U|_{\eta}$, $\langle \phi v \rangle|_{\eta} = V|_{\eta}$ and $\langle \phi w \rangle|_{\eta} = W|_{\eta}$. Equation 4.3.37 becomes

$$\beta|_{\eta}\frac{\partial \eta}{\partial t} + \frac{\partial Q_x}{\partial x} + \frac{\partial Q_y}{\partial y} = 0 \qquad (4.3.40)$$

where

$$(Q_x, Q_y) \equiv \int_{h_0}^{\eta}(U, V) dz \qquad (4.3.41)$$

We know from Equation 4.3.15 that

$$\Lambda = \int_{h_0}^{\eta}\beta(z) dz \qquad (4.3.42)$$

We introduce a wetted-area-average velocity $(\bar{u}, \bar{v})$ as

$$(\bar{u}, \bar{v}) = \frac{(Q_x, Q_y)}{\Lambda} = \frac{\int_{h_0}^{\eta}(U, V) dz}{\Lambda} = \frac{\int_{h_0}^{\eta}\langle \phi u, \phi v \rangle dz}{\int_{h_0}^{\eta}\langle \phi \rangle dz} \qquad (4.3.43)$$

and write Equation 4.3.40 as

$$\beta|_{\eta}\frac{\partial \eta}{\partial t} + \frac{\partial(\bar{u}\Lambda)}{\partial x} + \frac{\partial(\bar{v}\Lambda)}{\partial y} = 0 \qquad (4.3.44)$$

Taking the derivative w/r time of Λ in Equation 4.3.17 gives

$$\frac{\partial \Lambda}{\partial t} = \begin{cases} \delta \frac{\partial \eta}{\partial t} + \frac{(1-\delta)}{\lambda} \lambda \left[e^{\lambda[\eta - (h_0 + z^*)]} \right] \frac{\partial \eta}{\partial t} = \beta|_\eta \frac{\partial \eta}{\partial t}; & h_0 < \eta \leq h_0 + z^* \\ \frac{\partial \eta}{\partial t}; & \eta > h_0 + z^* \end{cases} \tag{4.3.45}$$

Using the relation between derivatives of η and Λ w/r time in Equation 4.3.45, we can finally write Equation 4.3.28 in conservative form as

$$\frac{\partial \Lambda}{\partial t} + \frac{\partial(\bar{u}\Lambda)}{\partial x} + \frac{\partial(\bar{v}\Lambda)}{\partial y} = 0 \tag{4.3.46}$$

For shallow water flows, the vertical momentum equation can be simplified by neglecting acceleration and stresses such that the hydrostatic pressure distribution is recovered. The three-dimensional momentum equations read as follows:

$$\rho \frac{\partial u}{\partial t} + \rho \nabla \cdot u\mathbf{u} = \nabla \cdot \mathbf{t_x} - \frac{\partial p}{\partial x} \tag{4.3.47}$$

$$\rho \frac{\partial v}{\partial t} + \rho \nabla \cdot v\mathbf{u} = \nabla \cdot \mathbf{t_y} - \frac{\partial p}{\partial y} \tag{4.3.48}$$

$$0 = \rho g z + \frac{\partial p}{\partial z} \tag{4.3.49}$$

where u and v are the x, y velocity components, p is pressure, ρ is fluid density, and $\mathbf{t_x}$ and $\mathbf{t_y}$ are x and y components of both viscous and turbulent stresses.

Considering the x-momentum equation and using the phase-averaging, we obtain

$$\rho \frac{\partial}{\partial t} \langle \phi u \rangle + \rho \nabla \cdot \langle \phi u\mathbf{u} \rangle - \rho \langle \nabla \phi \cdot u\mathbf{u} \rangle - \nabla \cdot \langle \phi \mathbf{t_x} \rangle + \langle \nabla \phi \cdot \mathbf{t_x} \rangle + \rho g \left\langle \phi \frac{\partial \eta}{\partial x} \right\rangle = 0 \tag{4.3.50}$$

$\nabla \phi = 0$ except the bottom where it is normal to the flow, eliminating the third term. Decomposing the velocity in the second term in 4.3.50 into an intrinsic phase-averaged velocity $\mathbf{U}/\beta$ and a fluctuation velocity $\tilde{\mathbf{u}}$ defined according to $\langle \phi \tilde{u} \rangle = 0$, we can rewrite

it as

$$\rho\frac{\partial U}{\partial t} + \rho\nabla\cdot(U\mathbf{U}/\beta) + \rho g\beta\frac{\partial\eta}{\partial x} + \rho\nabla\cdot\langle\phi\tilde{u}\tilde{\mathbf{u}}\rangle - \nabla\cdot\langle\phi\mathbf{t_x}\rangle + \langle\nabla\phi\cdot\mathbf{t_x}\rangle = 0 \quad (4.3.51)$$

The last term in Equation 4.3.51 represents the bottom stress τ_{bx}. $\langle\phi\tilde{u}\tilde{\mathbf{u}}\rangle$ represents the momentum exchange due to vertical variation of the velocity field and can be lumped into $\mathbf{t_x}$ (Defina, 2000). Equation 4.3.51 becomes

$$\rho\frac{\partial U}{\partial t} + \rho\nabla\cdot(U\frac{\mathbf{U}}{\beta}) + \rho g\beta\frac{\partial\eta}{\partial x} + \beta\tau_{bx} - \nabla\cdot\mathbf{T_x} = 0 \quad (4.3.52)$$

Here, $\mathbf{T_x}$ is the phase-averaged stress tensor. Depth integrating Equation 4.3.51 from h_0 to η, we get

$$\rho\int_{h_0}^{\eta}\frac{\partial U}{\partial t}dz + \rho\int_{h_0}^{\eta}\nabla\cdot U\frac{\mathbf{U}}{\beta}dz + \rho g\int_{h_0}^{\eta}\beta\frac{\partial\eta}{\partial x}dz + \int_{h_0}^{\eta}\beta\tau_{bx}dz - \int_{h_0}^{\eta}\nabla\cdot\mathbf{T_x}dz = 0 \quad (4.3.53)$$

Looking into the first two terms of Equation 4.3.53 and applying Leibnitz' rule, we obtain

$$\int_{h_0}^{\eta}\frac{\partial U}{\partial t}dz + \int_{h_0}^{\eta}\nabla\cdot U\frac{\mathbf{U}}{\beta}dz = \frac{\partial}{\partial t}\int_{h_0}^{\eta}Udz - U|\eta\frac{\partial\eta}{\partial t} + \frac{\partial}{\partial x}\int_{h_0}^{\eta}\frac{U^2}{\beta}dz - \frac{U^2}{\beta}|\eta\frac{\partial\eta}{\partial x} +$$
$$\frac{\partial}{\partial y}\int_{h_0}^{\eta}\frac{UV}{\beta}dz - \frac{UV}{\beta}|\eta\frac{\partial\eta}{\partial y} + \frac{1}{\beta}U|\eta W|\eta$$
$$(4.3.54)$$

Using the surface boundary condition in Equation 4.3.54 gives

$$\int_{h_0}^{\eta}\frac{\partial U}{\partial t}dz + \int_{h_0}^{\eta}\nabla\cdot U\frac{\mathbf{U}}{\beta}dz = \frac{\partial}{\partial t}\int_{h_0}^{\eta}Udz + \frac{\partial}{\partial x}\int_{h_0}^{\eta}\frac{U^2}{\beta}dz + \frac{\partial}{\partial y}\int_{h_0}^{\eta}\frac{UV}{\beta}dz \quad (4.3.55)$$

Putting Equation 4.3.55 back into Equation 4.3.53, we get

$$\rho\frac{\partial}{\partial t}\int_{h_0}^{\eta}Udz + \rho\frac{\partial}{\partial x}\int_{h_0}^{\eta}\frac{U^2}{\beta}dz + \rho\frac{\partial}{\partial y}\int_{h_0}^{\eta}\frac{UV}{\beta}dz + \rho g\Lambda\frac{\partial\eta}{\partial x} + \Lambda\tau_{bx} - \int_{h_0}^{\eta}\nabla\cdot\mathbf{T_x}dz = 0$$
$$(4.3.56)$$

Using Equation 4.3.41 in 4.3.56 yields

$$\rho \frac{\partial Q_x}{\partial t} + \rho \frac{\partial}{\partial x}\left(\frac{Q_x^2}{\Lambda}\right) + \rho \frac{\partial}{\partial y}\left(\frac{Q_x Q_y}{\Lambda}\right) + \rho g \Lambda \frac{\partial \eta}{\partial x} + \Lambda \tau_{bx} - \int_{h_0}^{\eta} \nabla \cdot \mathbf{T_x} dz = 0 \quad (4.3.57)$$

Using the relationship shown in Equation 4.3.43, Equation 4.3.57 can be written as

$$\frac{\partial \bar{u}\Lambda}{\partial t} + \frac{\partial \bar{u}^2 \Lambda}{\partial x} + \frac{\partial \bar{u}\bar{v}\Lambda}{\partial y} = -g\Lambda \frac{\partial \eta}{\partial x} - \Lambda \tau_{bx} + H\tilde{F}_x + G_x \quad (4.3.58)$$

Similarly, the y-momentum equation is

$$\frac{\partial \bar{v}\Lambda}{\partial t} + \frac{\partial \bar{u}\bar{v}\Lambda}{\partial x} + \frac{\partial \bar{v}^2 \Lambda}{\partial y} = -g\Lambda \frac{\partial \eta}{\partial y} - \Lambda \tau_{by} + H\tilde{F}_y + G_y \quad (4.3.59)$$

While the Equation 4.3.58 and 4.3.59 are in a similar form as given in Defina (2000), we have a different porosity distribution using the narrow slots. Here,

$$G_x = \frac{\partial \bar{u}^2 \Lambda}{\partial x} + \frac{\partial \bar{u}\bar{v}\Lambda}{\partial y} - H\tilde{F}_x - \left[\frac{\partial \overline{u^2}\Lambda}{\partial x} + \frac{\partial \overline{uv}\Lambda}{\partial y} - H\overline{F}_x\right] \quad (4.3.60)$$

$$G_y = \frac{\partial \bar{u}\bar{v}\Lambda}{\partial x} + \frac{\partial \bar{v}^2 \Lambda}{\partial y} - H\tilde{F}_y - \left[\frac{\partial \overline{uv}\Lambda}{\partial x} + \frac{\partial \overline{v^2}\Lambda}{\partial y} - H\overline{F}_y\right] \quad (4.3.61)$$

$$H\tilde{F}_x = \frac{\partial}{\partial x}\left[2\bar{A}_m \Lambda \frac{\partial \bar{u}}{\partial x}\right] + \frac{\partial}{\partial y}\left[\bar{A}_m \Lambda \left(\frac{\partial \bar{u}}{\partial y} + \frac{\partial \bar{v}}{\partial x}\right)\right] \quad (4.3.62)$$

$$H\tilde{F}_y = \frac{\partial}{\partial x}\left[\bar{A}_m \Lambda \left(\frac{\partial \bar{u}}{\partial y} + \frac{\partial \bar{v}}{\partial x}\right)\right] + \frac{\partial}{\partial y}\left[2\bar{A}_m \Lambda \frac{\partial \bar{v}}{\partial y}\right] \quad (4.3.63)$$

$$H\overline{F}_x = \frac{\partial}{\partial x}\overline{2A_m \Lambda \frac{\partial u}{\partial x}} + \frac{\partial}{\partial y}\overline{A_m \Lambda \left(\frac{\partial u}{\partial y} + \frac{\partial v}{\partial x}\right)} \quad (4.3.64)$$

$$H\overline{F}_y = \frac{\partial}{\partial x}\overline{A_m \Lambda \left(\frac{\partial u}{\partial y} + \frac{\partial v}{\partial x}\right)} + \frac{\partial}{\partial y}\overline{2A_m \Lambda \frac{\partial v}{\partial y}} \quad (4.3.65)$$

$$\tau_{bx}, \tau_{by} = \frac{gn^2\sqrt{\bar{u}^2 + \bar{v}^2}(\bar{u}, \bar{v})}{H_s^{1/3}} \qquad (4.3.66)$$

We have provided a higher Manning's n for narrower slots as a simple approximation of the reduced channel hydraulic radius and the increased wall roughness. Proudfoot et al. (2018) have shown the RMA2 model calibration in a similar way, where a higher Manning's n is assigned over marsh slots. Also, we have assigned a modified depth $H_s = \eta - h_0$ for τ_b when $\eta < h_0 + z^*$, and it changes to the regular depth $H = \eta - h_m$ when $\eta > h_0 + z^*$.

4.3.2.3 Revised wetting/drying criterion

In addition to the proposed equations, we have redefined the marsh surface as active wet domain until the water surface elevation is below h_0. During low tide when water surface elevation is below $h_0 + D_{min}$, the cell is assigned as a dry cell and its velocity is set to zero. When the surface elevation rises above $h_0 + D_{min}$, the cells are considered as wet and their velocities and elevations are solved for. The wetting/drying criterion for a node point is given as

$$\begin{cases} \text{wet}, & \text{if } H = \eta - h_0 + D_{min} > D_{min} \\ \text{dry} & \text{if } H = \eta - h_0 + D_{min} \leq D_{min} \end{cases} \qquad (4.3.67)$$

and, for a triangular cell (Figure A), is given as

$$\begin{cases} \text{wet}, & \text{if } H = \max\left(\eta_{\hat{i}}, \eta_{\hat{j}}, \eta_{\hat{k}}\right) - \min\left(h_{0,\hat{i}}, h_{0,\hat{j}}, h_{0,\hat{k}}\right) + D_{min} > D_{min} \\ \text{dry}, & \text{if } H = \max\left(\eta_{\hat{i}}, \eta_{\hat{j}}, \eta_{\hat{k}}\right) - \min\left(h_{0,\hat{i}}, h_{0,\hat{j}}, h_{0,\hat{k}}\right) + D_{min} \leq D_{min} \end{cases} \qquad (4.3.68)$$

4.4 Model evaluation using idealized cases

The model surface elevation map for the entire BHNWR, Figure 4.4, shows that the marsh platform has a widely varying scale for isolated hydraulic depressions in terms of area and depth. Most of the small depressions (length $\sim$ 10 - 100 m) resulted from model grid connectivity issues and not real depressions. Then, there are

real marsh depressions also identified from model surface elevation and stored volume, like the HOBO pressure gauge location shown in the Figure 4.3 a-c. In this model evaluation part, our goal is to determine whether the modified equations and the new wet/dry scheme can improve the overall hydrodynamics in well-formed idealized marsh depressions similar to a scale of the HOBO pressure gauge location.

4.4.1 Model setup and boundary forcing

We developed two idealized cases: A) A Bay-Marsh system, where a well defined marsh berm at the shoreline separates the land and water body, making an isolated depression over land during low tide (Figure 4.6 a-b), and B) A Bay-Marsh-Channel system, where a tidal channel separates the marsh platform into two similar isolated depressions (Figure 4.6 c-d). We assigned a similar berm property for both cases, where berm width $= 50m$, berm height $= 0.8m$ and $h_0 = 0.6m$. We expect that, in reality, these idealized depressions would flood and drain through the narrow rills of similar scale observed in the HOBO pressure gauge location. Unstructured grids for idealized cases are developed using the Surface-water Modeling System (SMS) v13.0 (https://www.aquaveo.com/). We have designed the mesh in a way that it provides maximum resolution around the marsh-channel shoreline and berms where the slots are assigned. Then, gradually the element size increases toward the Bay and the open boundary. For both cases, we have used an open boundary condition at the Bay boundary and provided a surface elevation forcing that has a slowly increasing amplitude and a period of 12.42 hours, keeping it similar to the BHNWR forcings. For different model runs, all the physical parameters such as the model minimum depth D_{min}, mixing coefficient A_m, and others are kept the same as cases mentioned in Chapter 2. Details about the spatial distribution of the model drag coefficient using Manning's n is given in the following section.

4.4.2 Results

4.4.2.1 Case-A: Bay-Marsh system

We used four tide gauges at different locations to represent the changes in flooding and draining across the Bay-Marsh system shown in Figure 4.6a. These point locations are chosen based on the uniqueness w/r to bathymetry and the distance from the berm, where Gauge 1 is in the open water and Gauge 2-4 are on land that goes through continuous wetting and drying. The variation of the slot width and cross-sectional area based on surface elevation is shown in 4.7. We can see that the model recovers regular element area and depth, as $\beta = 1$ and $\Lambda = H$ when the water surface surpass the slot top z^* (red dashed line).

Figure 4.8 shows the surface elevation comparison for three tide cycles after the berm overtopping, going from Bay to the marsh depression. Subsequently, the Figure 4.8b illustrates the changes in flow velocity inside the depression and flux through the berm. From Figure 4.8a, we can see that the surface elevation at Gauge 1 from both models show a similar response. Gauge 2 and 3 are located on both sides of the berm to explain the differences in wetting and drying, where Bay side goes through proper flooding and draining while the marsh portion stores water. It is evident from Figure 4.8a that at Gauge 3, the regular model stores water during low tide, and the minimum water surface elevation stays equal to the maximum berm elevation. After implementing slots on the berm, where we have varied the combination of δ and Manning's n, the surface comparison shows an improved flooding and draining over the marsh. The amplitude and speed varies based on the slot width and cross-sectional area shown in Figure 4.7. A decrease in the unit slot width δ reduces the model control volume porosity, which increased surface amplitude phase lag inside the marsh, more prominently during the low tide. The flow velocity inside the depression gradually became more flood dominant and the draining speed decreased as the slots got narrower (Figure 4.8b, left subplot). Figure 4.8b, right subplot shows the volume flux estimated through the berm. We have multiplied the depth-averaged velocity with time-varying slot depth and width to estimate volume flux through each cell face at the

transect, and finally took an integral over the entire transect for the total volume flux estimate. From the comparison between different slot sizes, we can see that the total volume flux reduces following the shrinkage in slot width. The difference in volume flux will be higher if the slot height z^* is higher based on the bottom elevation of the marsh depression. We have also estimated the tide-averaged volume flux and noticed that the residual value is less than 1% of the maximum flux magnitude for all cases, and the model conserves mass. Finally, to evaluate the dominant processes at the slot, we have estimated the momentum terms separately for a tide cycle shown in Figure 4.9. We chose $\delta = 0.001$, $\lambda = 100$, and a limited tide range to avoid marsh drying that generates numerical oscillation when the water surface is close to the bottom. The momentum balance shows that during both rising and falling tide, the pressure gradient at the marsh-Bay boundary is primarily balanced by bottom friction and all other terms are smaller when the surface stays in the slot range. It should be noted that, the balance can change when the tidal elevation is much higher than the slot height, and inertia can dominate instead of the bottom friction.

4.4.2.2   Case-B: Bay-Channel-Marsh system

After evaluating model mass conservation, we developed another scenario that includes a tidal channel separating the marsh, similar to the HOBO pressure gauge location (Figure 4.6 c-d). The aim of this test case to check the "leaking" process described by Nielsen and Apelt (2003) and Proudfoot et al. (2018) through the low porosity zone of the marsh elements when the water level fell inside the slot region. Both of these previous studies showed that a poor selection of marsh parameters in RMA2 model can result in a leakage of additional volume of water through elements that should be ideally impermeable. To take care of this problem, we have chosen a restricted range of elevation over the marsh surface that resolves the flooding and draining up to a lowest depression elevation h_0, and not the entire rill depth observed in a marsh. In Figure 4.10a, first, we have provided the surface comparison again. The two gauges 1 and 2 located on the Bay and channel show an identical behavior for the

different slot distributions. From the combination of marsh slots, and dynamic wetting and drying (i.e., element elimination), we can see that the channel surface elevation during low tide doesn't show any marsh leakage effect. The two other gauges 3 and 4 over the marsh platform illustrate the main effects of the slot properties. Gauge 4 is the farthest one from channel berm and shows a higher phase lag with a decrease in slot width and surface porosity compared to Gauge 3. We have used a smaller Manning's n value of 0.02 over marsh surface where no slots are implemented, and the phase delay is primarily from the area and drag changes in the slot. From this comparison, it is also evident that a narrow slot, in our case ranging from 0.1 to 0.001, slowly increases the hydro-period. Figure 4.10b illustrates the changes in flow velocity between Gauge 3 (close to the berm top) and Gauge 4 (depression bottom). As shown in the previous case, the maximum velocity magnitude during both flood and ebb remains same at the berm, and the ebb duration increases for a reduced slot width and lower porosity. When compared to the regular model (shown in red color) representing the physical channel berm, we can see that the peak magnitude during flood is almost similar for both models (Gauge 3) and can provide a reasonable estimate of the transport when surface overtop the berm. The difference between both models becomes prominent during the draining phase when the higher berm in the regular model disconnects the marsh interior from the channel and causes ponding.
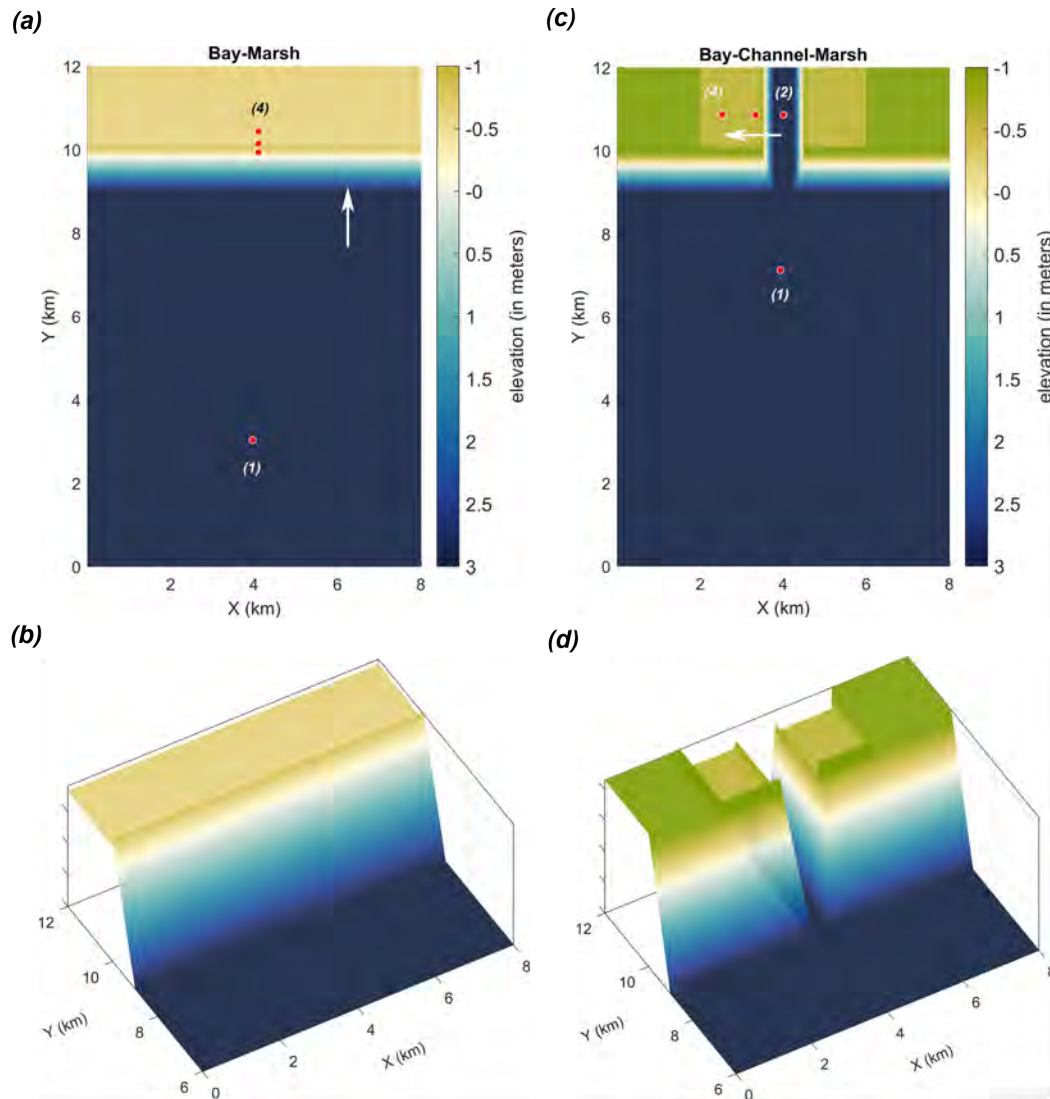
Figure 4.6: (a)-(b) A Bay-Marsh system, where a well defined marsh berm at the shoreline separates the land and water body, making an isolated depression over land during low tide. Red circles represent tide gauge locations used for model sensitivity evaluation; (c)-(d) A Bay-Marsh-Channel system, where a tidal channel separates the marsh platform into two similar isolated depressions. Red circles represent tide gauge locations used for model sensitivity evaluation.
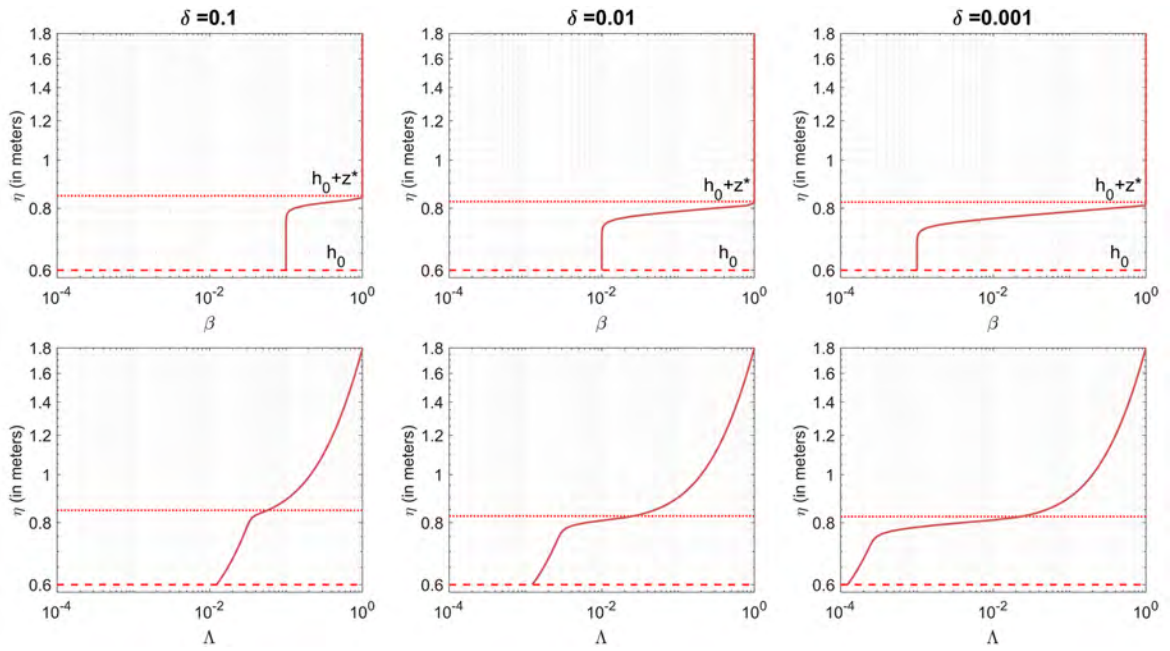
Figure 4.7: Variation of slot width and cross-sectional area based on different δ, η and $\lambda = 100$ for Case-A along Y = 10 KM, between gauge 2 and 3 (Figure 4.6a).
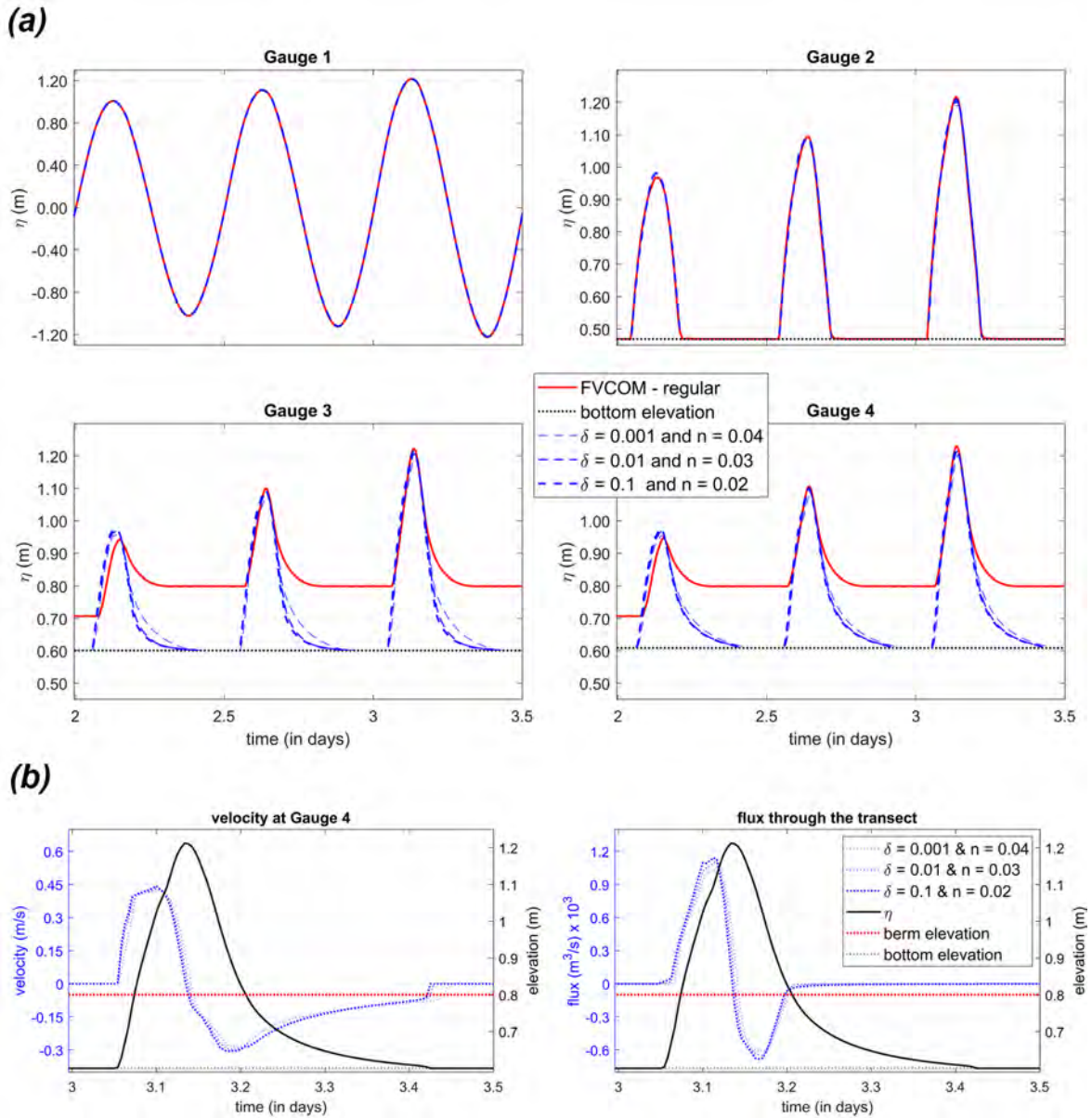
Figure 4.8: (a) Case-A surface elevation comparison for different slot/porosity distributions at tide gauge locations 1-4, directed from Bay toward the marsh depression (in meters). Red solid line represents regular FVCOM model, and the blue color shows result from the modified model; (b) left-subplot: A similar comparison like (a) for velocity changes at Gauge 4, inside the marsh depression (in m/s); right-subplot: Total volume flux going in and out of the marsh (in m³/s), estimated using a transect positioned at cross-shore position X = 0-8 km, Y = 10 KM in Figure 4.6a. Here, positive flux represents going in to the wetland, negative represents going out.
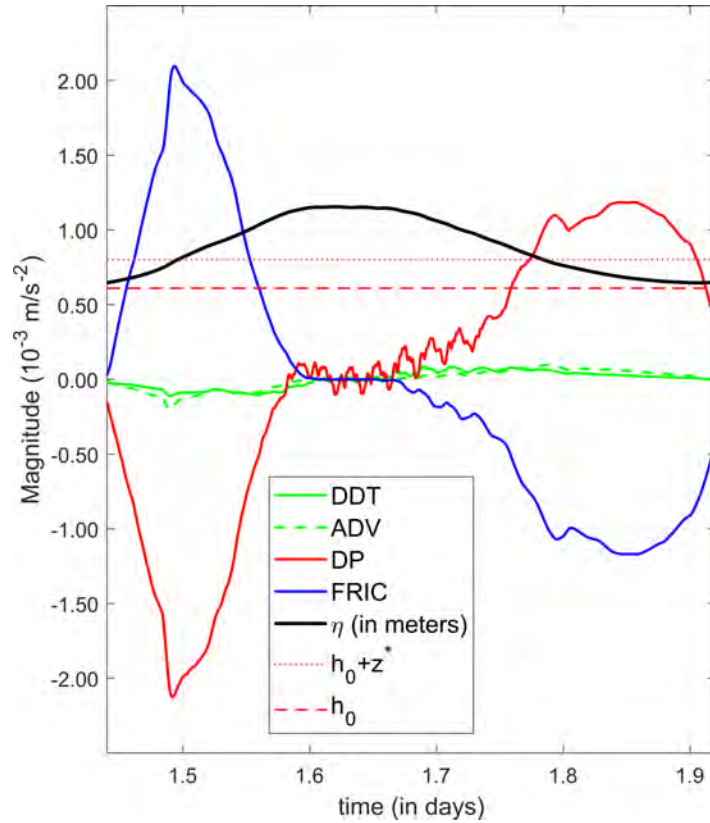
Figure 4.9: A tide cycle showing the vertically averaged terms of the y-momentum equation (Equation 4.3.13) for Case-A in slots along Y = 10 KM, between gauge 2 and 3. Here, DDT represents the local inertia, ADV the advective inertia, DP the barotropic pressure gradient and FRIC is the bottom friction. The 2D-3D momentum correction, horizonatal viscosity and coriolis term are observed to be smaller and not shown.

(a)

(b)
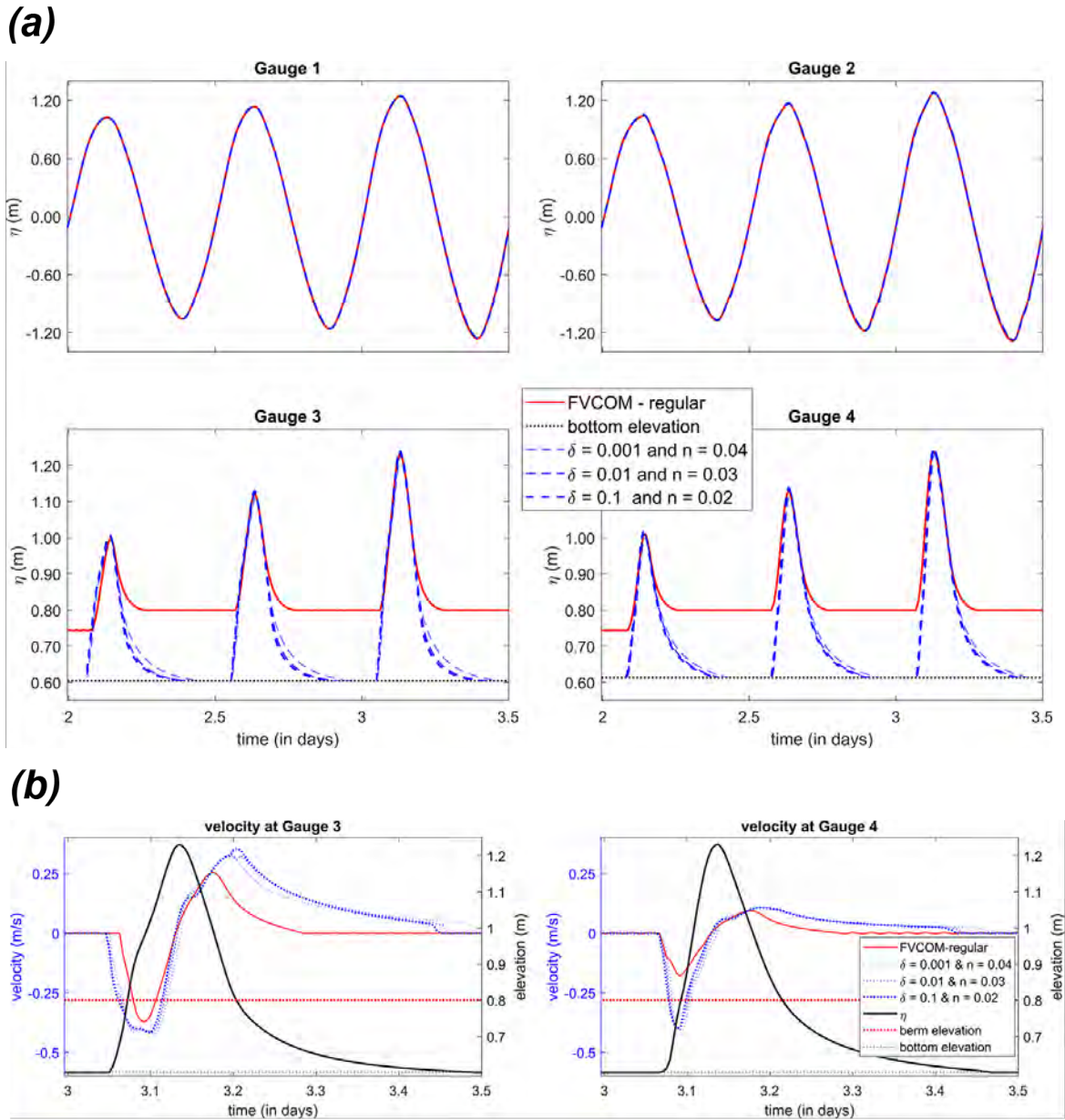
Figure 4.10: (a) Case-B surface elevation comparison for different slot/porosity distributions at tide gauge locations 1-4, directed from Bay toward the marsh depression (in meters) shown in Figure 4.6c (b) A similar comparison like (a) for velocity changes at Gauge 3 & 4, inside the marsh depression (in m/s). Here, negative velocity represents flood condition and flow going in to the wetland, and positive represents ebb and going out. Black solid line shows model surface elevation (in meters) at Gauge 3 & 4 for $\delta = 0.001$ and $n = 0.04$.

Beside slot geometry, the bottom and wall roughness can also play an essential role in controlling flow propagation and affecting surface elevation and phase variation. Where slots are assigned, the sensitivity of pond filling and draining to bottom friction also needed to be taken into account. In FVCOM 2D equations, the friction force is defined by the depth-dependent drag coefficient C_D, calculated using Manning's equation (Equation 4.3.11). In all our previous results, we have assumed a Manning's n in the range of 0.02 to 0.04 following the slot width contraction that represents higher roughness as the channel gets narrower. To examine the sensitivity of flow to both slot width/surface porosity and friction, we ran cases varying the Manning's n for the different slot sizes shown in Figure 4.11. We have gradually increased the Manning's n from 0.02 to 0.05, 0.03 to 0.06 and 0.04 to 0.07 for $\delta = 0.1$, 0.01 and 0.001 respectively to represent the drag from various types of marsh vegetation available in coastal areas Loder et al. (2009). Manning's n outside the slot distribution site is kept to 0.02. For a higher slot width $\delta = 0.1$, water drains faster from inside the depression for smaller n. While there is no considerable difference in surface phase during the flood, the increase in n and a smaller δ increases surface elevation phase lag, and retain more water inside the depression.
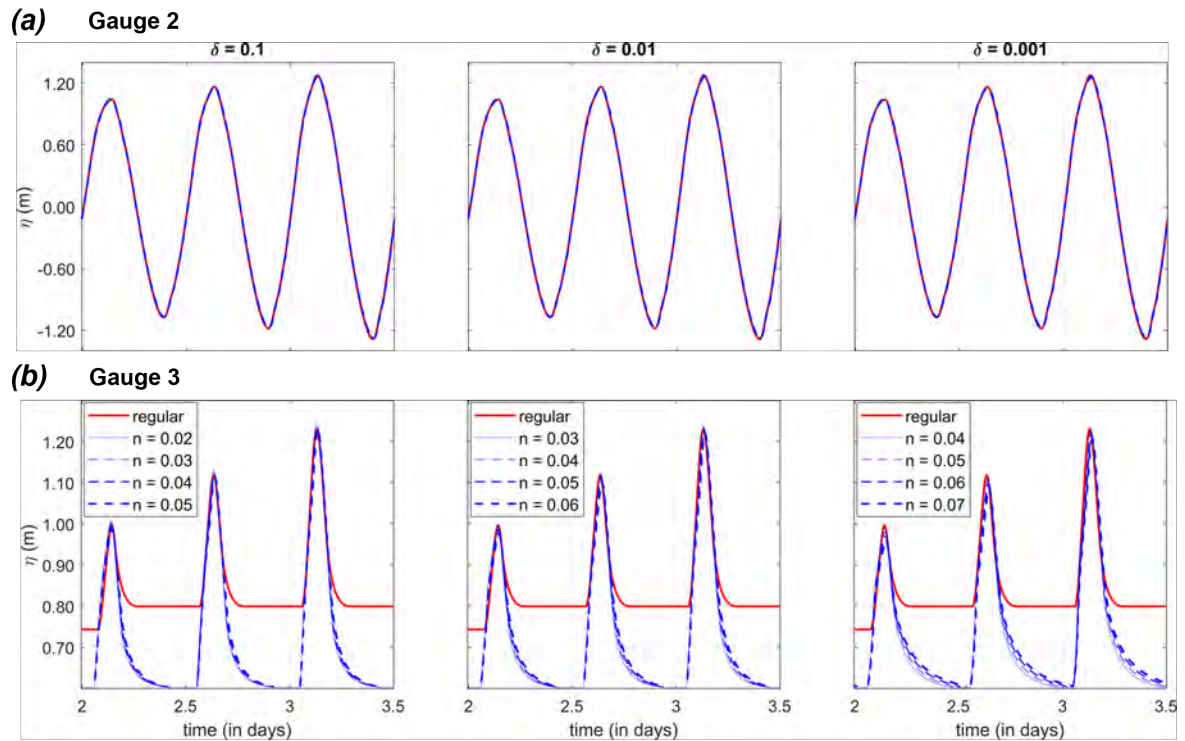
Figure 4.11: Case-B model sensitivity to changes in slot/porosity distributions and Manning's n; (a) surface elevation comparison at Gauge 2 (in meters); (b) surface elevation comparison at Gauge 3 (in meters). The darker colors represent results for increasing Manning's n.

4.5 Field verification of model

4.5.1 Model setup and boundary forcing

In this test, we used the water level and depth averaged velocity fields from the large scale three-dimensional model directly nested at the unstructured grid boundary for a stormy condition, described earlier in section 4.2. Results are compared with the field data collected from the BHNWR at HOBO pressure gauge location. The large scale ROMS simulations for the entire Bay included necessary forcings such as atmospheric forcing, tidal constituents and river discharge data from multiple sources, and they were validated against NOAA tide gauges located in the Bay (Deb et al., 2018a). The unstructured grid used in this case is developed for the previous studies, chapter 2 and 3, and extensively validated using tide gauge and current profiler data sets collected from the wetland channels. For more details about the digital elevation model (DEM) development, tidal and subtidal boundary condition, in-situ data collection and post-processing, and the regular FVCOM model validation, the reader is referred to both chapter 2 and 3. Again, all the physical parameters such as the model minimum depth D_{min}, mixing coefficient A_m, and others are kept the same as cases mentioned in chapter 2.

4.5.2 Results

In this section, we evaluate the effectiveness of the slot porosity approach in the isolated BHNWR marsh depression where HOBO pressure gauges were deployed along a transect from the channel berm into the marsh. The time series of water elevation at these gauges show the wetting and drying pattern and highlight the artificial ponding and phase lags in the regular FVCOM model simulations explained earlier in section 4.2. We have used the same storm condition (Hurricane Joaquin, 2015) described in Deb et al. (2020a), and ran the modified model for a similar period of 14 days matching the regular model simulations. In addition to the pressure gauges over the marsh surface, we also picked channel tide gauge locations inside the wetland (Figure 4.1, right subplot) for model validation. The channel tide gauges are regularly maintained by

the Delaware Department of Natural Resources and Environmental Control (DNREC) and more details about the data collection period and quality control are given in Deb et al. (2018b).

It is essential to adjust the surface porosity based on local flooding and draining data collected from the marsh depression. From the HOBO pressure gauge DEM elevation, a depression elevation h_0 of $0.55m$ (NAVD88) is chosen to assign slots over that particular location (Figure 4.3 a-c). We performed multiple large scale model simulations by varying all the slot variables shown earlier in the idealized cases. From the combinations, we have observed that a $\delta = 0.0001$ and Manning's n of 0.05 over the marsh slot shows a considerable improvement in model skill when compared to $\delta = 0.1$ and Manning's n of 0.02, shown in Figure 4.12. Compared to the regular model (Figure 4.2), we now observe a better draining at HOBO 3 to 6 during low tide. Water surface amplitude and phase in all of the gauges show a good agreement with the in-situ data, representing an improved flooding and draining on the entire depression. Among all the gauges, only at HOBO 6, it still shows the storage of water during both regular and storm period. This gauge is located on a real isolated pond inside the depression and the model elevation is below the selected h_0 value for the marsh surface. Our model has inaccurate elevation at that location from the DEM, and also the grid resolution is not high enough to resolve the small rill that drains it during the low tide. The scatter comparison for both regular and modified model at HOBO locations is shown in Figure 4.13. Also, the error statistics is given in Table 4.1, where the comparisons have been assessed in terms of model skill Willmott (1981), average bias index (Equation 2.3.1-2.3.2) and R^2. A model skill of 1.0 shows perfect agreement, and a positive/negative bias represents model over/under-prediction.

At HOBO 3-6, we can observe a noticeable improvement compared to HOBO 1 and 2, positioned close to the channel berm and drain properly, even in the regular model grid (Figure 4.3 and 4.2). Model skill increased at HOBO 3-5 located in the center of the depression. The regression coefficients and R^2 values also show a higher correlation between model with slots and in-situ compared to the traditional approach.

The average bias index shows an essential contrast between the outcomes from the two model setups. The regular FVCOM model overestimates surface elevation during flood and completely misses phase, where the modified model slightly underestimates. Again, we can improve this underestimation further by properly tuning the model slot properties and drag coefficient. Both modeling approaches show similar statistics at Navigation light and Leatherberry tide gauges, located on the channels (Figure 4.14a). However, at Dock (the farthest upstream tide gauge), there is a notable discrepancy seen during Hurricane Joaquin for the regular model. This gauge is located on the main Leipsic channel and close to the HOBO pressure gauge location subjected to artificial ponding in model results. During 2015, both calm conditions and at the time of Hurricane Joaquin, the model predicts a faster falling tide and a slightly higher peak than the in-situ data. After implementing slots in the marsh depression, we noticed an immediate improvement in surface phase prediction at Dock, shown in Figure 4.14b. The amplitude now slightly decreases as some of the channel volume goes toward filling the slots during high tide.
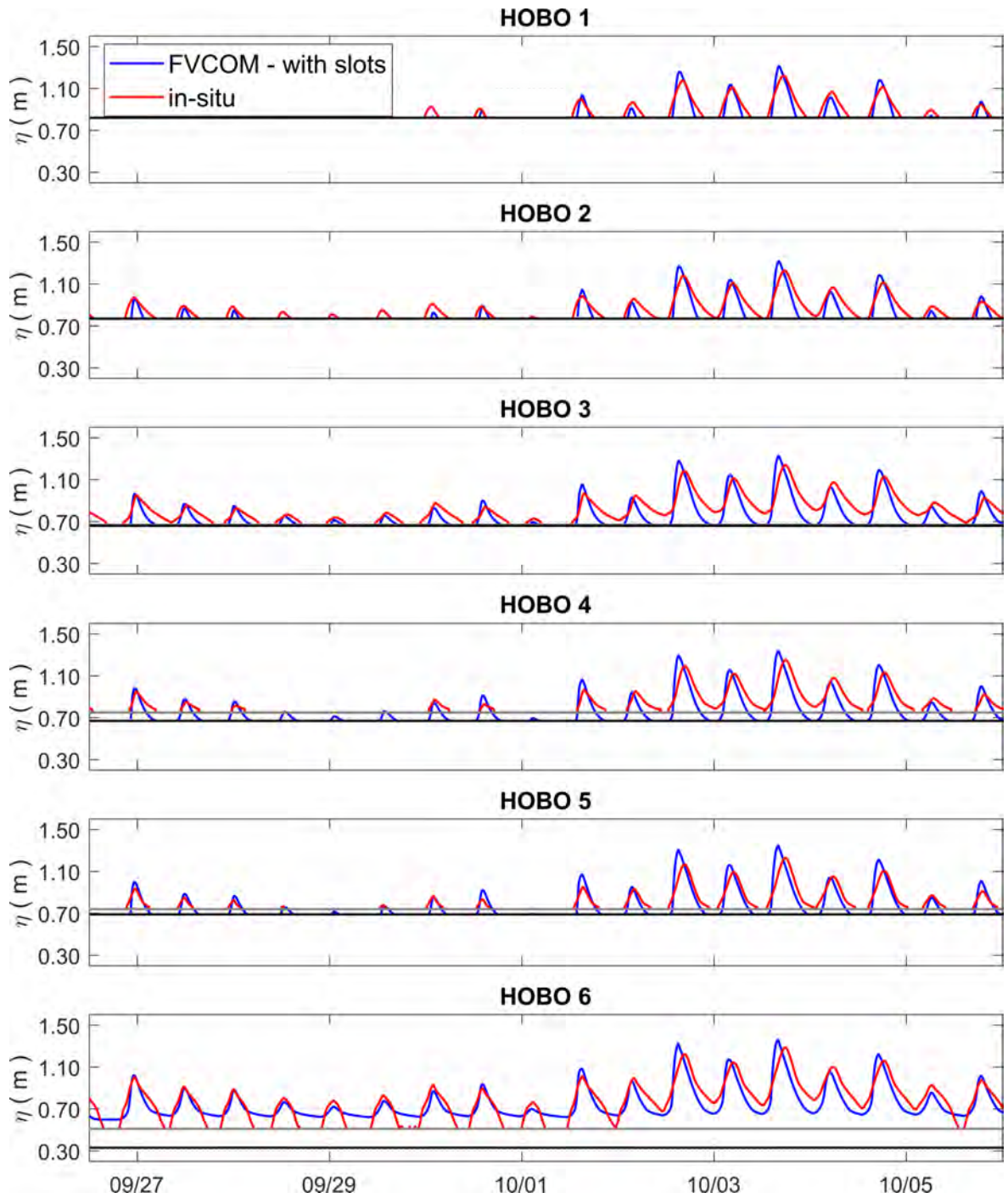
Figure 4.12: A comparison between modified FVCOM model with $\delta = 0.0001$ & $n = 0.05$ (in blue) and in-situ (in red) water surface elevation during Hurricane Joaquin, 2015 at different HOBO gauge locations (in meters, from NAVD88 vertical reference level). The black and gray straight lines represent FVCOM model grid and surveyed bottom elevation.

124
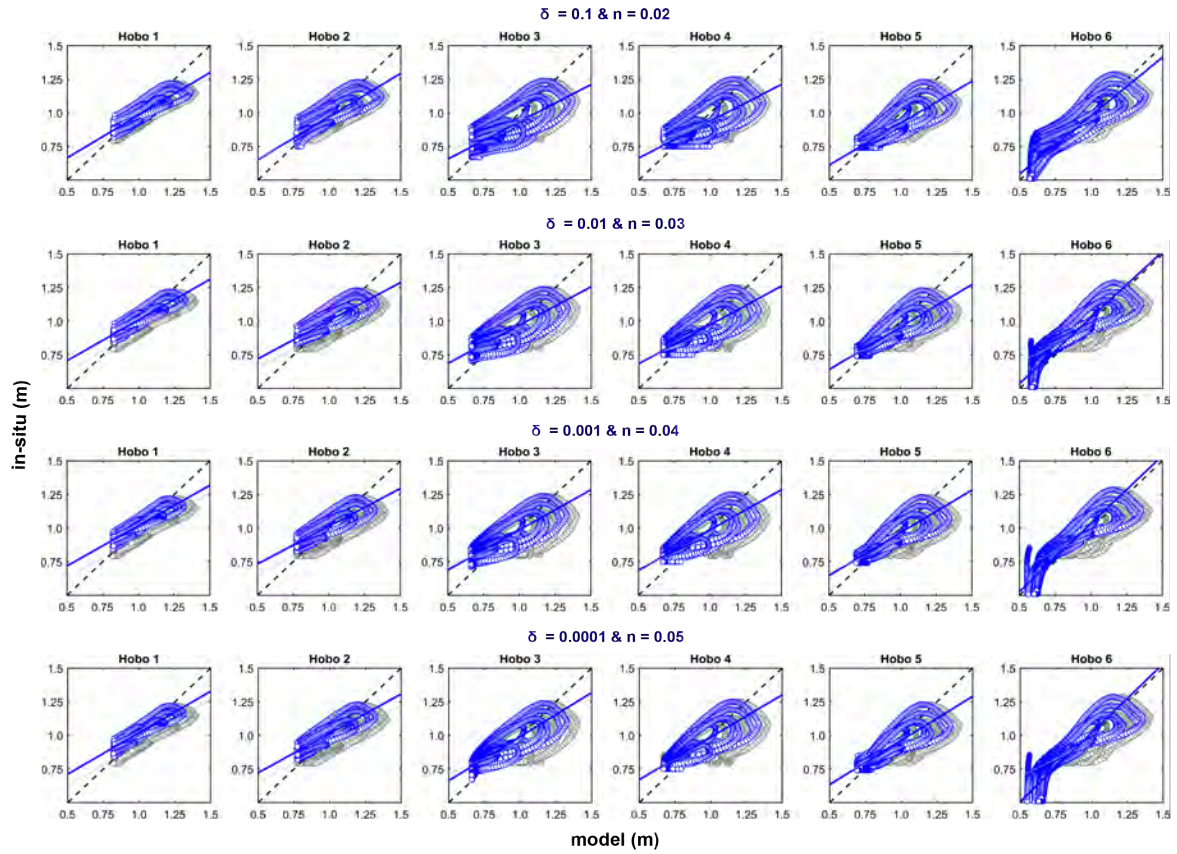
Figure 4.13: Scatter comparison between FVCOM model and in-situ water surface elevation at the HOBO pressure gauge locations. Gray color shows the comparison for regular model and blue color represents modified model. Model vs in-situ statistics is given in Table 4.1.

125
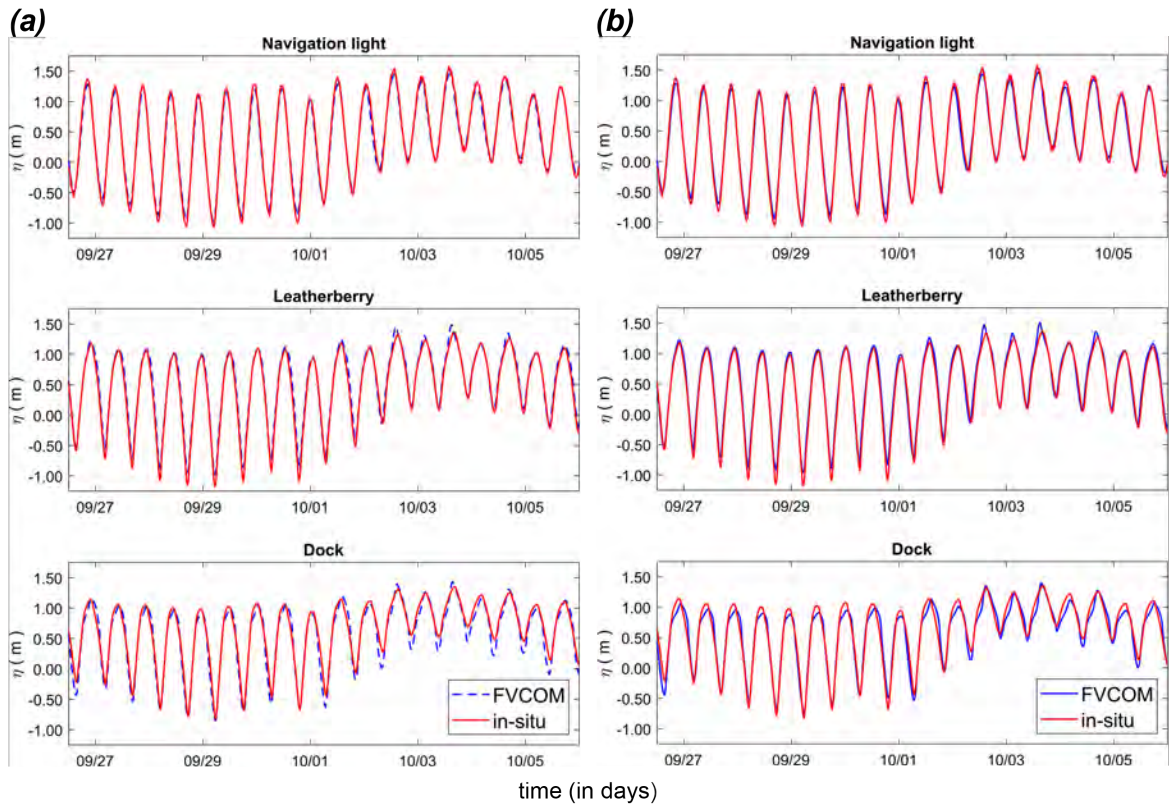
Figure 4.14: (a) Comparison between regular FVCOM model (in blue) and in-situ (in red) water surface elevation during Hurricane Joaquin, 2015 at different channel tide gauges (in meters, from NAVD88 vertical reference level); (b) Similar comparison between modified model ($\delta = 0.0001$ & $n = 0.05$) and in-situ.

126

Statistics from the model comparison with in-situ data				
Gauge	FVCOM	Bias	Skill	R^2
HOBO 1	Regular	0.05	0.89	0.89
	$\delta = 0.1$, n = 0.02	0.01	0.91	0.88
	$\delta = 0.01$, n = 0.03	-0.01	0.89	0.87
	$\delta = 0.001$, n = 0.04	-0.02	0.89	0.88
	$\delta = 0.0001$, n = 0.05	-0.03	0.90	0.90
HOBO 2	Regular	0.04	0.84	0.80
	$\delta = 0.1$, n = 0.02	0.007	0.89	0.82
	$\delta = 0.01$, n = 0.03	-0.03	0.86	0.82
	$\delta = 0.001$, n = 0.04	-0.04	0.85	0.83
	$\delta = 0.0001$, n = 0.05	-0.04	0.86	0.85
HOBO 3	Regular	0.03	0.74	0.64
	$\delta = 0.1$, n = 0.02	0.003	0.79	0.67
	$\delta = 0.01$, n = 0.03	-0.05	0.81	0.73
	$\delta = 0.001$, n = 0.04	-0.07	0.82	0.79
	$\delta = 0.0001$, n = 0.05	-0.07	0.84	0.83
HOBO 4	Regular	0.04	0.74	0.65
	$\delta = 0.1$, n = 0.02	0.004	0.80	0.69
	$\delta = 0.01$, n = 0.03	-0.04	0.82	0.75
	$\delta = 0.001$, n = 0.04	-0.06	0.83	0.79
	$\delta = 0.0001$, n = 0.05	-0.06	0.85	0.82
HOBO 5	Regular	0.10	0.66	0.64
	$\delta = 0.1$, n = 0.02	0.04	0.86	0.80
	$\delta = 0.01$, n = 0.03	-0.006	0.89	0.84
	$\delta = 0.001$, n = 0.04	-0.01	0.90	0.85
	$\delta = 0.0001$, n = 0.05	-0.01	0.91	0.86
HOBO 6	Regular	0.03	0.79	0.71
	$\delta = 0.1$, n = 0.02	-0.02	0.92	0.86
	$\delta = 0.01$, n = 0.03	-0.04	0.91	0.86
	$\delta = 0.001$, n = 0.04	-0.04	0.91	0.86
	$\delta = 0.0001$, n = 0.05	-0.04	0.91	0.86

Table 4.1: Comparison between model and in-situ at HOBO locations

4.6   Summary and discussion

In inter-tidal areas, traditional large-scale coastal models may suffer from artificial ponding due to the presence of artificially isolated depressions which store water over marsh platforms. It is a universal modeling problem that results from the missing model representation of rills and cuts through channel berms, due to insufficient horizontal grid resolution and underlying inaccuracies in the regional DEM. This error in model hydrodynamics can directly affect the prediction of the hydro-period, dynamic vegetation growth, the volume and speed of flooding and draining processes over the marsh surface. The deposition of fine sediments over the marsh surface varies based on the tidal properties, vegetation types and the available suspended sediment concentration (Kirwan and Murray, 2007). The higher sediment concentration near the channel bank is observed to decay exponentially depending on the water depth, horizontal flow velocity, and particle settling velocity as the distance increases (Christiansen et al., 2000). In recent studies, Fagherazzi et al. (2012) and Zhang et al. (2019) have demonstrated the critical role of averaged velocity and water depth over the marsh platform in changing the sediment transport length scale during flooding. The artificial water storage in isolated depressions would misrepresent the transport length scale, and cause a different trend in sedimentation and elevation changes on the marsh surface.

In this study, we have first demonstrated the limitation of traditional modeling over the marsh surface using a 2D unstructured grid model FVCOM. The surface elevation comparison with the pressure gauge data collected from the marsh depression and flood map have shown that, after a surge event, overland flooding and draining inside the wetland is severely affected by artificial ponding. To treat this problem, We have implemented an artificial surface porosity in the model calculations to improve the overall marsh inundation process. Following the previous work of Defina (2000), we have modified the mass conservation and momentum equation using a narrow slot or permeable-seabed technique around the artificially isolated depressions. The model performance is evaluated using two different idealized marsh depression conditions and the realistic BHNWR marsh HOBO pressure gauge location. Both idealized cases have

shown the effectiveness of narrow slots in flooding and draining the isolated depressions. The channel berm porosity decreases following the slot contraction, and increases the surface phase lag inside the marsh. Slot height and width are defined in a way that it is narrower at the berm and then gradually reaches the unit width and area as the distance from berm increases. Subsequently, we have also looked into the changes in depth-averaged velocity that show an incremental increase in ebb duration from the slot width contraction and lower porosity at the berm. At the channel berm, the similarity in peak velocity magnitude during flood shows that the new equations can provide a reliable prediction of the velocity, which can give a better estimate of fine sediment transport if used with the corrected water depth. Changes to the slot bottom friction is incorporated by providing a higher Manning's n at the channel berms. We have observed that a narrow slot in combination with higher Manning's n, can affect the draining phase more compared to the flood. The slot roughness has been defined using a simple approximation of the Manning's n and the depth changes in the slot region, and would require further studies in the future to properly address the changes in slot hydraulic radius. After evaluating the model performance and sensitivity using idealized cases, we have used the same set of parameters in the realistic artificial ponding case in BHNWR. We assigned surface porosity on the channel berms that surrounded HOBO pressure gauges over the marsh platform. The new modeling strategy over the isolated depressions is observed to improve the marsh flooding and draining accuracy to a great extent compared to the traditional approach. However, to eliminate artificial ponding from the entire wetland, it is necessary to have a large network of pressure gauge deployed over all the profoundly affected areas, which will help to calibrate the marsh porosity.

Chapter 5

SUMMARY AND FUTURE WORK

5.1 Summary of presented work

This study consists of three chapters which described (1) sensitivity of tidal hydrodynamics to wetland morphology changes, (2) importance of channel shoreline and bathymetry resolution in improving the numerical model accuracy, and (3) removal of model artificial water storage over marsh platform by implementing a stochastic porosity distribution in the governing equations.

The second chapter describes field data collection and a high-resolution unstructured grid 2D model setup and validation for simulating hydrodynamic processes in Bombay Hook National Wildlife Refuge, Delaware. An excellent model performance is observed compared to the in-situ point source observations in terms of water surface elevation and current velocity. The modeling framework is then used to assess the role of historical anthropogenic and natural morphological disturbances in changing the overall tidal dynamics. We have observed that an abrupt channel construction or inlet opening in a connected multi-inlet wetland system can significantly affect the system's natural balance. It can increase the natural frequency, decrease frictional dissipation, and ultimately lead to an ebb dominant condition that increases channel erosion. The numerical model results are also explained using simple scaling analysis and the first-order balance of the governing hydrodynamic forces.

In the third chapter we have demonstrated that poor grid resolution around marsh-channel berms creates artificial channel convergence and inaccurate tidal wave characteristics. The inaccurate channel bathymety and inadequate resolution might provide an acceptable model of surface elevation when compared to in-situ data but,

at the same time, completely misrepresent the velocity field. This model inaccuracy can lead to faulty estimates of other important processes such as net circulation and sediment transport. The study has shown that a high-resolution marsh-channel boundary in combination with a dense bathymetry survey can dramatically improve the configuration of tidally varying channel hypsometry and increase numerical model reliability. We recommend to always compare both the model surface elevation and velocity field when developing a modeling framework for complex salt-marsh environments.

Furthermore, in chapter four we have observed that the models predictions of overland flow and sediment transport onto tidal marsh platforms can be affected by the effect of artificial ponding, or the retention of ponded water in low areas of the platform. These areas would drain in the real world, providing a greater potential volume for water transport onto the platform during flooding, but small topographic features that make drainage possible are represented poorly or not at all in a coarse model grids, data sets used to build DEM's for model grids, or both. We have treated this problem by adding an effective porosity to the marsh surface over a restricted range of elevations, and tested the modified governing equations in an application to the wetland system within the Bombay Hook National Wildlife Refuge, Delaware.

5.2 Future work

The results of the study have emphasized the need for further work before the model could be used to assess long-term sedimentation problems and geomorphology evolution.

- With the present explicit scheme and wetting/drying algorithm, the model is observed to produce unrealistic velocities near steep marsh-channel boundaries due to the rapid drawdown between control volumes during the ebb tide. This artificially generated volume is not significant compared to the total tidal volume flux transported in and out of the wetland; however, it can affect the net circulation estimates from the entire system based on the total inundated area, model computational time step, and the minimum depth. A better treatment of

the pressure gradient term at the steep wet/dry boundary might further improve the model accuracy.

- We have observed the 3D model instability when assigned more than three sigma vertical layers for the entire model domain because of the extreme shallow conditions over the marsh surface. An improved 2D-3D coupled modeling framework is needed in the future, where the model will resolve the higher resolution vertical layers in the channel, and only the depth-averaged quantities on the marsh surface.

- A large network of pressure gauges is required over the properly identified hydrualic depressions to calibrate spatially varying slot parameters, and eliminate artificial ponding from the entire wetland.

- The sensitivity of the porosity distribution and marsh platform flooding/draining to different unstructured grid resolution also need to be tested for prescribing the optimum model resolution.

BIBLIOGRAPHY

Abdolali, A., Kirby, J.T., Shi, F., Guiteras, S., Deb, M., 2016. Field and modeling studies of salt marshes in Bombay Hook National Wildlife Refuge in Delaware, in: RAETCS16) Restore America's Estuaries 8th National Summit on Coastal and Estuarine Restoration and 25th Biennial Meeting of The Coastal Society, New Orleans, LA.

Aretxabaleta, A.L., Ganju, N.K., Butman, B., Signell, R.P., 2017. Observations and a linear model of water level in an interconnected inlet-bay system. Journal of Geophysical Research: Oceans 122, 2760–2780. doi:10.1002/2016JC012318.

Aubrey, D.G., Speer, P.E., 1985. A Study of Non-linear Tidal Propagation in shallow inlet / estuarine systems Part I : Observations. Estuarine, Coastal and Shelf Science 21, 185–205. doi:doi:10.1016/0272-7714(85)90096-4.

Bates, P.D., Hervouet, J.M., 1999. A new method for moving–boundary hydrodynamic problems in shallow water. Proceedings of the Royal Society of London. Series A: Mathematical, Physical and Engineering Sciences 455, 3107–3128.

Berg, R., 2016. National Hurricane Center Tropical Cyclone Report Hurricane Joaquin. Technical Report. Rep. AL112015, National Hurricane Center.

Bomers, A., Schielen, R.M.J., Hulscher, S.J., 2019. The influence of grid shape and grid size on hydraulic river modelling performance. Environmental fluid mechanics 19, 1273–1294.

Boon, J.D., Byrne, R.J., 1981. On basin hyposmetry and the morphodynamic response of coastal inlet systems. Marine Geology 40, 27–48. doi:10.1016/0025-3227(81)90041-4.

Brunner, G., Bonner, V., 2010. HEC River Analysis System (HEC-RAS) Version 4.1 January 2010 , 411URL: http://oai.dtic.mil/oai/oai?verb=getRecord{&}metadataPrefix=html{&}identifier=ADA289522.

Chen, C., Beardsley, R.C., Cowles, G., Qi, J., Lai, Z., Gao, G., Stuebe, D., Liu, H., Xu, Q., Xue, P., Ge, J., Hu, S., Ji, R., Tian, R., Huang, H., Wu, L., Lin, H., Sun, Y., Zhao, L., 2013. An unstructured grid, finite-volume community ocean model FVCOM user manual (3rd edition). Technical Report MITSG 12-25. Sea Grant College Program, Massachusetts Institute of Technology.

Chen, C., Qi, J., Li, C., Beardsley, R.C., Lin, H., Walker, R., Gates, K., 2008. Complexity of the flooding/drying process in an estuarine tidal-creek salt-marsh system: An application of FVCOM. Journal of Geophysical Research: Oceans 113. doi:10.1029/2007JC004328.

Chen, J.L., Ralston, D.K., Geyer, W.R., Sommerfield, C.K., Chant, R.J., 2018. Wave Generation, Dissipation, and Disequilibrium in an Embayment With Complex Bathymetry. Journal of Geophysical Research: Oceans 123, 7856–7876. doi:10.1029/2018JC014381.

Chen, J.L., Shi, F., Hsu, T.J., Kirby, J.T., 2014. NearCOM TVD A quasi-3D nearshore circulation and sediment transport model. Coastal Engineering 91, 200–212.

Chen, Q., Kirby, J.T., Dalrymple, R.A., Kennedy, A.B., 2000. Boussinesq modeling of wave transformation, breaking, and runup. II: 2D. Journal of Waterway, Port, Coastal, and Ocean Engineering 126, 48–56.

Christiansen, T., Wiberg, P.L., Milligan, T.G., 2000. Flow and sediment transport on a tidal salt marsh surface. Estuarine, Coastal and Shelf Science 50, 315–331. doi:10.1006/ecss.2000.0548.

Chuang, W.S., Swenson, E.M., 1981. Subtidal water level variations in Lake Pontchartrain, Louisiana. Journal of Geophysical Research: Oceans 86, 4198–4204.

D'Alpaos, A., Lanzoni, S., Marani, M., Rinaldo, A., 2007. Landscape evolution in tidal embayments: Modeling the interplay of erosion, sedimentation, and vegetation dynamics. Geophysical Research Letters 112, 1–17. doi:10.1029/2006JF000537.

D'Alpaos, L., Defina, A., 2007. Mathematical modeling of tidal hydrodynamics in shallow lagoons: A review of open issues and applications to the Venice lagoon. Computers and Geosciences 33, 476–496. doi:10.1016/j.cageo.2006.07.009.

Deb, M., Abdolali, A., Kirby, J.T., Shi, F., 2018a. Hydrodynamics, sediment transport and wind waves in an eroding salt marsh environment. Bombay Hook National Wildlife Refuge, Delaware. Research Report CACR-18-04. Center for Applied Coastal Research, Department of Civil and Environmental Engineering, University of Delaware. Newark, DE.

Deb, M., Abdolali, A., Kirby, J.T., Shi, F., 2020a. Hydrodynamic modeling in an eroding salt marsh: Importance of channel shoreline resolution and bathymetry survey. Coastal Engineering submitted.

Deb, M., Abdolali, A., Kirby, J.T., Shi, F., Guiteras, S., 2020b. Sensitivity of tidal hydrodynamics to morphology changes in a multi-inlet rapidly eroding salt marsh system: A numerical study. Hydrological Processes submitted.

Deb, M., Abdolali, A., McDowell, C., Kirby, J.T., Sommerfield, C.K., Shi, F., 2018b. Hydrodynamic, survey and sediment data collection. Bombay Hook National Wildlife Refuge, Delaware. Research Report CACR-18-03. Center for Applied Coastal Research, Department of Civil and Environmental Engineering, University of Delaware. Newark, DE.

Defina, A., 2000. Two-dimensional shallow flow equations for partially dry areas. Water Resources Research 36, 3251. doi:10.1029/2000WR900167.

Defina, A., D'Alpaos, L., Matticchio, B., 1994. New set of equations for very shallow water and partially dry areas suitable to 2D numerical models. Proceedings of the Specialty Conference on Modelling of Flood Propagation Over Initially Dry Areas , 72–81.

Dierssen, H.M., Theberge, A.E., 2014. Bathymetry: Assessing Methods. Encyclopedia of Ocean Sciences .

Dietrich, J.C., Tanaka, S., Westerink, J.J., Dawson, C., Luettich, R., Zijlema, M., Holthuijsen, L.H., Smith, J., Westerink, L., Westerink, H., 2012. Performance of the unstructured-mesh, SWAN+ ADCIRC model in computing hurricane waves and surge. Journal of Scientific Computing 52, 468–497.

Dohner, S., Trembanis, A., Miller, D., 2016. A tale of three storms: Morphologic response of Broadkill Beach, Delaware, following Superstorm Sandy, Hurricane Joaquin, and Winter Storm Jonas. Shore & Beach 84, 3.

Dozier, H.L., 1947. Salinity as a factor in Atlantic Coast tidewater muskrat production, in: North American Wildlife Conference Transactions, pp. 398–420.

Dronkers, J., 1986. Tidal asymmetry and estuarine morphology. Netherlands Journal of Sea Research 20, 117–131.

EPA, 2010. Coastal Wetlands Initiative: Mid-Atlantic Review. Technical Report.

Fagherazzi, S., Kirwan, M.L., Mudd, S.M., Guntenspergen, G.R., Temmerman, S., Rybczyk, J.M., Reyes, E., Craft, C., Clough, J., 2012. Numerical models of salt marsh evolution: Ecological, geormorphic, and climatic factors. Review of Geophysics 50, 1–28. doi:10.1029/2011RG000359.

Familkhalili, R., Talke, S.A., 2016. The effect of channel deepening on tides and storm surge: A case study of Wilmington, NC. Geophysical Research Letters 43, 9138–9147. doi:10.1002/2016GL069494.

Friedrichs, C.T., 2010. Barotropic tides in channelized estuaries. Contemporary Issues in Estuarine Physics , 27–61.doi:10.1017/CBO9780511676567.004.

Friedrichs, C.T., Aubrey, D.G., 1988. Nonlinear tidal distortion in shallow well-mixed estuaries. Estuarine, Coastal and Shelf Science 27, 521–545. doi:10.1016/0272-7714(90)90054-U.

Friedrichs, C.T., Madsen, O.S., 1992. Nonlinear diffusion of the tidal signal in frictionally dominated embayments. Journal of Geophysical Research 97, 5637. doi:10.1029/92JC00354.

Horritt, M., Bates, P., 2001. Predicting floodplain inundation: raster-based modelling versus the finite-element approach. Hydrological processes 15, 825–842.

Horritt, M., Bates, P., Mattinson, M., 2006. Effects of mesh resolution and topographic representation in 2D finite volume models of shallow water fluvial flow. Journal of Hydrology 329, 306–314.

Hsu, T.J., Chen, S.N., Ogston, A.S., 2013. The landward and seaward mechanisms of fine-sediment transport across intertidal flats in the shallow-water region-A numerical investigation. Continental Shelf Research 60, S85–S98. URL: http://dx.doi.org/10.1016/j.csr.2012.02.003, doi:10.1016/j.csr.2012.02.003.

Huang, H., Chen, C., Blanton, J.O., Andrade, F.A., 2008. A numerical study of tidal asymmetry in Okatee Creek, South Carolina. Estuarine, Coastal and Shelf Science 78, 190–202. doi:10.1016/j.ecss.2007.11.027.

Hund, E., 2013. NOAA orthorectified Digital Elevation Model (DEM) image tiles, Bombay Hook, Delaware, 2011. Technical Report NODC Accession 0112173. Coastal Services Center, National Oceanographic Data Center.

Hunt, J.N., 1964. Tidal Oscillations in Estuaries. Geophysical Journal International 8, 440–455.

Ippen, A., 1966. Estuary and Coastline Hydrodynamics. Engineering societies monographs, Mac Graw-Hill Book Company. URL: https://books.google.com/books?id=XNaiwgEACAAJ.

Jan, A., Coon, E.T., Graham, J.D., Painter, S.L., 2018. A subgrid approach for modeling microtopography effects on overland flow. Water Resources Research 54, 6153–6167. doi:10.1029/2017WR021898.

Jay, D.A., 1991. Green's law revisited: Tidal long-wave propagation in channels with strong topography. Journal of Geophysical Research 96, 20585. doi:10.1029/91JC01633.

Kauffman, G.J., Homsey, A., Chatterson, S., McVey, E., Mack, S., 2011. Economic value of the Delaware estuary watershed. Technical Report. Institute for Public Administration's Water Resources Agency, University of Delaware.

Kennedy, A.B., Chen, Q., Kirby, J.T., Dalrymple, R.A., 2000. Boussinesq modeling of wave transformation, breaking, and runup. I: 1D. Journal of Waterway, Port, Coastal, and Ocean Engineering 126, 39–47. doi:`10.1061/(ASCE)0733-950X(2000)126:1(39)`.

King, I., 2000. RMA2 Version 6.6 User Manual.

Kirwan, M.L., Murray, A.B., 2007. A coupled geomorphic and ecological model of tidal marsh evolution. Proceedings of the National Academy of Sciences of the United States of America 104, 6118–6122. doi:`10.1073/pnas.0700958104`.

Kirwan, M.L., Walters, D.C., Reay, W., Carr, J.A., 2016. Sea level driven marsh expansion in a coupled model of marsh erosion and migration. Geophysical Research Letters 43, 4366–4373. doi:`10.1002/2016GL068507`.

Kukulka, T., Jenkins III, R.L., Kirby, J.T., Shi, F., Scarborough, R.W., 2017. Surface wave dynamics in Delaware Bay and its adjacent coastal shelf. Journal of Geophysical Research: Oceans 122, 8683–8706. doi:`10.1002/2017JC013370`.

Lesser, G.R., Roelvink, J.v., Van Kester, J., Stelling, G., 2004. Development and validation of a three-dimensional morphological model. Coastal engineering 51, 883–915.

Li, Z., Hodges, B.R., 2020. On modeling subgrid-scale macro-structures in narrow twisted channels. Advances in Water Resources 135, 103465. URL: `https://doi.org/10.1016/j.advwatres.2019.103465`, doi:`10.1016/j.advwatres.2019.103465`.

Loder, N.M., Irish, J.L., Cialone, M.A., Wamsley, T.V., 2009. Sensitivity of hurricane surge to morphological parameters of coastal wetlands. Estuarine, Coastal and Shelf Science 84, 625–636. doi:`10.1016/j.ecss.2009.07.036`.

Luettich Jr, R.A., Westerink, J.J., Scheffner, N.W., 1992. ADCIRC: An Advanced Three-Dimensional Circulation Model for Shelves, Coasts, and Estuaries. Report 1. Theory and Methodology of ADCIRC-2DDI and ADCIRC-3DL. Technical Report. Coastal engineering research center Vicksburg MS.

Mariotti, G., Fagherazzi, S., 2010. A numerical model for the coupled long-term evolution of salt marshes and tidal flats. Journal of Geophysical Research: Earth Surface 115, 1–15. doi:`10.1029/2009JF001326`.

McDowell, C., 2017. Marsh sediment accumulation and accretion on a rapidly retreating estuarine coast. Master of Science in Marine Studies. University of Delaware. College of Earth, Ocean and Environment.

McDowell, C., Sommerfield, C.K., 2016. Geomorphic analysis of Bombay Hook NWR, Delaware Wetlands Conference, Wilmington, DE.

Morris, J.T., 2006. Competition among marsh macrophytes by means of geomorphological displacement in the intertidal zone. Estuarine, Coastal and Shelf Science 69, 395–402. doi:10.1016/j.ecss.2006.05.025.

Mudd, S.M., Fagherazzi, S., Morris, J.T., Furbish, D.J., 2013. Flow, sedimentation, and biomass production on a vegetated salt marsh in South Carolina: Toward a predictive model of marsh morphologic and ecologic evolution. American Geophysical Union (AGU). chapter 9. pp. 165–188. doi:10.1029/CE059p0165.

Nidzieko, N.J., 2010. Tidal asymmetry in estuaries with mixed semidiurnal/diurnal tides. Journal of Geophysical Research: Oceans 115, 1–13. doi:10.1029/2009JC005864.

Nidzieko, N.J., Ralston, D.K., 2012. Tidal asymmetry and velocity skew over tidal flats and shallow channels within a macrotidal river delta. Journal of Geophysical Research: Oceans 117, 1–17. doi:10.1029/2011JC007384.

Nielsen, C., Apelt, C., 2003. Parameters Affecting the Performance of Wetting and Drying in a Two-Dimensional Finite Element Long Wave Hydrodynamic Model. Journal of Hydraulic Engineering 129, 628–636. doi:10.1061/(asce)0733-9429(2003)129:8(628).

Officer, C.B., 1976. Physical Oceanography of Estuaries. Wiley & Sons, New York.

Panday, S., Huyakorn, P.S., 2004. A fully coupled physically-based spatially-distributed model for evaluating surface/subsurface flow. Advances in Water Resources 27, 361–382. doi:10.1016/j.advwatres.2004.02.016.

Parker, B.B., 1984. Friction Effects on the Tidal Dynamics of a Shallow Estuary. John Hopkins University, PhD Thesis , 292.

Pawlowicz, R., Beardsley, B., Lentz, S., 2002. Classical tidal harmonic analysis including error estimates in MATLAB using T_TIDE. Computers & Geosciences 28, 929–937. doi:10.1016/S0098-3004(02)00013-4.

Proudfoot, M., Valentine, E.M., Evans, K.G., King, I., 2018. Calibration of a marsh-porosity finite element model: Case study from a macrotidal creek and floodplain in Northern Australia. Journal of Hydraulic Engineering 144, 05017005. doi:10.1061/(ASCE)HY.1943-7900.0001413.

Ralston, D.K., Geyer, W.R., Traykovski, P.A., Nidzieko, N.J., 2013. Effects of estuarine and fluvial processes on sediment transport over deltaic tidal flats. Continental Shelf Research 60, S40–S57. doi:10.1016/j.csr.2012.02.004.

Ralston, D.K., Geyer, W.R., Warner, J.C., 2012. Bathymetric controls on sediment transport in the Hudson River estuary: Lateral asymmetry and frontal trapping. Journal of Geophysical Research: Oceans 117, 1–21. doi:10.1029/2012JC008124.

Ralston, D.K., Talke, S., Geyer, W.R., Al-Zubaidi, H.A., Sommerfield, C.K., 2019. Bigger Tides, Less Flooding: Effects of Dredging on Barotropic Dynamics in a Highly Modified Estuary. Journal of Geophysical Research: Oceans 124, 196–211. doi:10.1029/2018JC014313.

Ramsey, K., Reilly, M.J., 2002. The Hurricane of October 21-24, 1878. Delaware Geological Survey Special Publication 22, 90.

Rodrigues, A.P.F., 2016. Hydrodynamic modeling of Delaware Bay with applications to storm surges and coastal flooding: Current conditions and future scenarios. Master of Science in Marine Studies. University of Delaware. College of Earth, Ocean and Environment.

Runion, K.D., 2019. Variability of sediment transport at a tidal wetland restoration site: Prime Hook National Wildlife Refuge, Delaware. Master's thesis. University of Delaware.

Schmid, K.A., Hadley, B.C., Wijekoon, N., 2011. Vertical Accuracy and Use of Topographic LIDAR Data in Coastal Marshes. Journal of Coastal Research 27, 116–132. doi:10.2112/JCOASTRES-D-10-00188.1.

Speer, P.E., 1984. Tidal distortion in shallow estuaries. Ph.D. thesis. MIT/WHOI.

Speer, P.E., Aubrey, D.G., Friedrichs, C.T., 1991. Nonlinear hydrodynamics of shallow tidal inlet/bay systems. Tidal hydrodynamics , 321–339.

Stammerman, R., 2013. Hydrodynamics and sediment transport studies in tidal marshes of the Delaware Bay using high resolution numerical models. Ph.D. thesis. Drexel University.

Stedman, S.M., Dahl, T.E., 2008. Status and trends of wetlands in the coastal watersheds of the eastern United States, 1998 to 2004. Technical Report. National Oceanic and Atmospheric Administration, National Marine Fisheries Service and U.S. Department of the Interior, Fish and Wildlife Service.

Sullivan, K., Uccellini, L., 2013. Service assessment: Hurricane/post-tropical cyclone Sandy, October 22–29, 2012. Technical Report. US Department of Commerce NOAA and NWS, Silver Spring, Maryland.

Symonds, A.M., Vijverberg, T., Post, S., van der Spek, B.J., Henrotte, J., Sokolewicz, M., 2017. Comparison between MIKE 21 FM, Delft3D and Delft3D FM flow models of Western Port Bay, Australia. Coastal Engineering Proceedings 1, 11.

Tiner, R.W., 1987. Mid-Atlantic wetlands: a disappearing natural treasure. Technical Report. US Fish and Wildlife Service, Fish and Wildlife Enhancement, National Wetlands Inventory Project.

Van Rijn, L., et al., 2010. Tidal phenomena in the Scheldt Estuary .

Warner, J.C., Armstrong, A., He, R., Zambon, J.B., 2010. Development of a coupled ocean–atmosphere–wave–sediment transport (COAWST) modeling system. Ocean Modelling 35, 230 – 244. doi:https://doi.org/10.1016/j.ocemod.2010.07.010.

Williams, S.J., 1995. Louisiana coastal wetlands: A resource at risk. Technical Report. US Geological Survey.

Willmott, C.J., 1981. ON THE VALIDATION OF MODELS. Physical Geography 2, 184–194. doi:10.1080/02723646.1981.10642213.

Yu, D., Lane, S.N., 2006. Urban fluvial flood modelling using a two-dimensional diffusion-wave treatment, part 1: Mesh resolution effects. Hydrological Processes 20, 1541–1565. doi:10.1002/hyp.5935.

Zhang, X., Leonardi, N., Donatelli, C., Fagherazzi, S., 2019. Fate of cohesive sediments in a marsh-dominated estuary. Advances in Water Resources 125, 32–40. URL: https://doi.org/10.1016/j.advwatres.2019.01.003, doi:10.1016/j.advwatres.2019.01.003.

Appendix A

FVCOM DISCRETIZATION AND CODE MODIFICATION
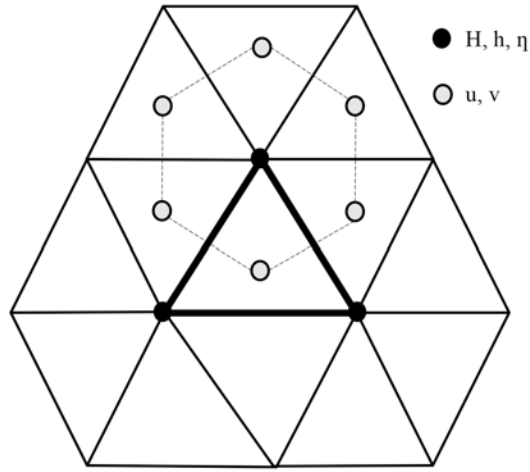
Figure A1: Schematic of the control volume and element in the unstructured grid FVCOM

A.1 The Discrete Procedure - 2D External Mode

Here, we have given a summary of the 2D external mode FVCOM discretization from Chen et al. (2013):

The continuity equation integrated over a horizontal patch is given by

$$\iint \frac{\partial \eta}{\partial t} dxdy = -\iint \left[\frac{\partial(\bar{u}H)}{\partial x} + \frac{\partial(\bar{v}H)}{\partial x} \right] dxdy \qquad (A.1.1)$$

Integrating Equation A.1.1 numerically using the modified fourth-order Runge-Kutta time-stepping scheme gives

$$\eta_j^0 = \eta_j^n, R_\eta^0 = R_\eta^n = \sum_{m=1}^{NT(j)} \left[(\Delta x_{2m-1}\bar{v}_m^n - \Delta y_{2m-1}\bar{u}_m^n) H_{2m-1}^n + (\Delta x_{2m}\bar{v}_m^n - \Delta y_{2m}\bar{u}_m^n) H_{2m}^n \right]$$

(A.1.2)

and

$$\eta_j^k = \eta_j^0 - \alpha^k \frac{\Delta t R_\eta^{k-1}}{2\Omega_j^\eta}; \text{ and } \eta_j^{n+1} = \eta_j^4$$

(A.1.3)

where $k = 1, 2, 3, 4$ and $\alpha^1, \alpha^2, \alpha^3, \alpha^4 = (1/4, 1/3, 1/2, 1)$. Ω_j^η is the area enclosed by the lines through centroids and mid-points of the sides of surrounding triangles connected to the node. $\bar{u}_m^n$ and $\bar{v}_m^n$ are defined as

$$\bar{u}_m^n = \overline{u(NT(m))}^n, \bar{v}_m^n = \overline{v(NT(m))}^n$$

(A.1.4)

Integrating the x-momentum equation over a given triangular area gives:

$$\iint \frac{\partial \bar{u} H}{\partial t} dx dy = -\oint_{s'} \bar{u} H \bar{v}_n ds' + \iint f\bar{v} H dx dy - \iint gH \frac{\partial \eta}{\partial x} dx dy$$
$$- \iint \frac{\tau_{bx}}{\rho_o} dx dy + \iint H\widetilde{F}_x dx dy + \iint G_x dx dy$$

(A.1.5)

Integrating Equation A.1.5 numerically using the modified fourth-order Runge-Kutta time-stepping scheme gives

$$\bar{u}_i^0 = \bar{u}_i^n, \overline{R}_u^0 = \overline{R}_u^n$$

(A.1.6)

$$\bar{u}_i^k = \bar{u}_i^0 - \alpha^k \frac{\Delta t \overline{R}_u^0}{4\Omega_i^u \bar{H}_i}$$

(A.1.7)

$$\bar{u}_i^{n+1} = \bar{u}_i^4$$

(A.1.8)

Ω_i^u is the area where $\bar{u}$ and $\bar{v}$ are located in the cell centroid.

A.1.1 Determining velocity at the cell edge

velocity at the edge mid-point

$$\widehat{u}_{im} = 0.5 \left[\phi_i^u \left(\bar{x}'_m, \bar{y}'_m \right) + \phi_{\text{NBi}(m)}^u \left(\bar{x}'_m, \bar{y}'_m \right) \right] \tag{A.1.9}$$

$$\widehat{v}_{im} = 0.5 \left[\phi_i^v \left(\bar{x}'_m, \bar{y}'_m \right) + \phi_{\text{NBi}(m)}^v \left(\bar{x}'_m, \bar{y}'_m \right) \right] \tag{A.1.10}$$

where,

$$\Phi_i^u \left(x', y' \right) = \bar{u}_{i,0} + a_i^u x' + b_i^u y' \tag{A.1.11}$$

$\bar{u}_{i,0}$ is the velocity at cell center, and a_i^u and b_i^u are determined by a least-square method based on velocity values at the cell center and nearest three cell centered points.

Flux through the side m of a triangle is

$$\bar{V}_{nm} = \widehat{v}_n \left(X_n \left(N_i \left(j_2 \right) - X_m \left(N_i \left(j_1 \right) \right) - \widehat{u}_m \left(Y_n \left(N_i \left(j_2 \right) \right) - Y_n \left(N_i \left(j_1 \right) \right) \right) \tag{A.1.12}$$

The velocity for the cell edge is then chosen as

$$\bar{u}_{im} = \begin{cases} \phi_i^u(0,0) & \bar{V}_{nm} < 0 \\ \phi_{NB_i(m)}^u \left(x_{im}, y_{im} \right), & \bar{V}_{nm} \geq 0 \end{cases} \tag{A.1.13}$$

A.2 Modified FVCOM modules with slot porosity

FVCOM modules modified to include the slot porosity parameters can be downloaded from the following repository:

https://github.com/mithundeb/FVCOM---slot-porosity